Automated image analysis techniques for cardiovascular magnetic resonance imaging
Geest, R.J. van der

Automated Image Analysis Techniques for Cardiovascular Magnetic Resonance Imaging

Robertus Jacobus van der Geest
2011

Automated Image Analysis Techniques for Cardiovascular Magnetic Resonance Imaging

Proefschrift

ter verkrijging van
de graad van Doctor aan de Universiteit Leiden,
op gezag van Rector Magnificus prof. mr. P.F. van der Heijden
volgens besluit van het College van Promoties
ter verdediging op dinsdag 22 maart 2011
klokke 16:15 uur

door

Robertus Jacobus van der Geest

geboren te Leiderdorp
in 1966

PROMOTIECOMMISIE

Promotor:
Prof. dr. ir. J.H.C. Reiber

Overige leden:
Prof. dr. A. de Roos
Prof. dr. E.E. van der Wall
Prof. dr. A.C. van Rossum   VU Medisch Centrum, Amsterdam

Contents

CHAPTER

1

General introduction and outline

1.1 BACKGROUND

Assessment of quantitative parameters describing the status of the cardiac system is of eminent importance for the diagnosis and follow-up of patients with cardiac disease. Cardiac Magnetic Resonance Imaging (CMR) is one of the many imaging modalities used in clinical practice. CMR can be used to study multiple aspects of the cardiac system in a single examination, such as information on the cardiac anatomy, function, perfusion, flow and tissue characteristics. This would otherwise require multiple studies with different imaging modalities, and the subsequent difficulty in combining these data from the different unregistered modalities each with their spatial and temporal scales. As a three-dimensional (3D) technique, highly accurate volumetric measurements can be obtained without relying on the use of geometrical assumptions, making CMR a powerful technique to study complex structures such as the left and right ventricle. Repeat CMR examinations can be obtained without exposing the patient to harmful radiation or contrast agents. This makes CMR an ideal technique to perform repeat examinations on a patient for quantitative evaluation of the effects of medical treatment.

Visual and quantitative interpretation of a typical MR study requires review and processing of a huge number of images. For quantitative analysis image segmentation is required. The process of image segmentation involves the definition of the myocardial boundaries and other structures in the images. For the assessment of left ventricular function, imaging is usually preformed using a cine-MR acquisition in the short-axis view, in which the heart is imaged in eight to ten imaging sections from apex to base at 20 to 30 time points within the cardiac cycle. As a result, quantitative assessment of the ventricular volume over the cardiac cycle requires the definition of the endocardial (inner) contour of the myocardium in 160 to 300 images. For the assessment of left ventricular mass and regional assessment of the ventricular wall thickness over the cardiac cycle an additional set of epicardial (outer) contours is required. Furthermore, for more extensive quantitative analysis, such as the assessment of right ventricular function, myocardial perfusion, flow and myocardial scar tissue, additional image segmentation is needed. Clearly, manual contour tracing for all these CMR acquisitions is too demanding for routine clinical use. Consequently, the availability of automated or semi-automated contour detection techniques is demanded to fully exploit the information provided by a CMR examination.

1.2 SCOPE OF THIS THESIS

The work described in this thesis is inspired by the clinical needs as described above. Quantitative image analysis has advantages over visual image interpretation as it provides objective numbers which can be used to decide upon the appropriate treatment. The use of automated contour detection potentially has several benefits as it may result in a considerable decrease in the image analysis time and produces objective and reproducible results. Moreover, since automated contour detection is much faster, it also enables assessment of additional quantitative parameters which are derived by taking into account all the available image data. An example of such parameter is the regional rate of wall thickening and wall thinning from short-axis Cine MR. This parameter requires endocardial and epicardial contours in all time frames, which is only practical when automated contour detection is available.

The goal of the research described in this thesis is therefore:
- To investigate automated and semi-automated contour detection techniques for the assessment of quantitative indices of cardiac function
- To develop and evaluate techniques for the assessment of cardiac parameters from CMR image data
- To validate the developed algorithms on clinical CMR studies 7by comparing automated results to results obtained by expert observers.
- To investigate the feasibility of applying an automated contour detection algorithm on images acquired on MR scanners from different vendors using different MR pulse sequences.

1.3 THESIS OUTLINE

The remainder of this thesis is structured as follows.

Chapter 2 provides an overview of image processing techniques developed for quantitative analysis of cardiac MR image data. While the other chapters are mainly focusing on assessment of left ventricular function, this chapter also provides a summary of CMR image analysis techniques for other cardiac parameters, such as perfusion and viability.

Chapter 3 describes a method for semi-automated detection of the myocardial boundaries in multi-slice short-axis cine-MR imaging studies. The method described in this chapter uses low-level image processing techniques such as adaptive thresholding and edge-detection combined with usage of *a priori* information in order to optimize the robustness of the algorithm.

Chapter 4 describes an automated contour detection method for assessment of aortic flow throughout the cardiac cycle from velocity-encoded MR imaging studies. By exploiting the temporal coherence of the image data, the described algorithm provides accurate results, also in the presence of image frames with poor image quality.

In **Chapter 5** a new approach for quantitative assessment of myocardial wall thickness is presented. In contrast to pre-existing methods, the new method explores the three-dimensional nature of multi-slice short-axis studies to obtain improved accuracy of the wall thickness measurements.

Chapter 6 describes a contour detection method for short-axis cine MR studies based on Active Appearance Models. In this chapter the concept of Active Appearance Models was used to develop a 2D+time model. Based on a training set of pre-segmented short-axis MR image series, the left ventricular shape and image appearance is modeled, including the temporal variation from the end-diastolic phase to the end-systolic phase. This information is described in a statistical frame work and used as *a priori* information during the segmentation of new image series. The main advantage of this approach is that the complete time-sequence of images is used to obtain a consistent time-continuous segmentation result. This improves the robustness compared to a single-image (2D) Active Appearance Models implementation.

Chapter 7 describes an alternative contour detection approach for the detection of left ventricular endo- and epicardial contours, which exploits the temporal continuity of cardiac contraction and relaxation. The presented algorithm is an extension to the minimum cost contour detection algorithm which is frequently used in various medical image segmentation problems in 2D images. The method requires an accurate segmentation of a single frame and temporally propagates this segmentation based on local similarity properties and enforcing temporal continuity.

As segmentation algorithms get more complex, it becomes nearly impossible to guarantee that the various parameters controlling the behavior of the algorithm are defined optimally. In addition, it can be observed that images acquired with different pulse-sequences or obtained with different MR scanners do have varying image characteristics. The existence of these image characteristics variations were the motivation for developing an automated parameter optimization procedure, which is described in **Chapter 8**.

Finally, general conclusions of the thesis are presented in Chapter 9.

CHAPTER

2

Quantification in cardiac MRI

2.1 INTRODUCTION

Magnetic resonance imaging (MRI) has become an indispensable imaging modality for the evaluation of the cardiac system. MRI stand outs as is provides unique capabilities for studying many aspects of cardiac anatomy, function, perfusion and viability in a single imaging session. Volumetric measurement of the ventricular cavities and myocardium can be performed at high accuracy and precision as have been demonstrated in many experimental and clinical research studies. The 3D-nature of cardiovascular MRI also provides detailed information of the cardiac system at a regional level. Among others, regional end-diastolic wall thickness and systolic wall thickening provide useful information for the assessment of the location, extent and severity of ventricular abnormalities in ischemic heart disease. MRI can also be used to study blood flow and myocardial perfusion. Velocity-encoded cine MRI (VEC-MRI) is often utilized for the quantification of blood flow through the aortic and pulmonary valves and atrio-ventricular valve planes, which has shown to be clinically valuable in the evaluation of patients with complex congenital heart disease.

Typical cardiac MRI examinations generate large data sets of images. To optimally and efficiently extract the relevant clinical information from these data sets dedicated software solutions featuring automated image segmentation and optimal quantification and visualization methods are needed. Quantitative image analysis requires the definition of contours describing the inner and outer boundaries of the ventricles, which is a laborious and tedious task when based on manual contour tracing. Reliable automated or semi-automated image analysis software would be required to overcome these limitations. This paper focuses on the state-of-the-art post-processing techniques for the quantitative assessment of global and regional ventricular function from cardiac MRI.

2.2 QUANTIFICATION OF VENTRICULAR DIMENSIONS AND GLOBAL FUNCTION

2.2.1 Accuracy and reproducibility of volumetric measurements from multi-slice short-axis acquisitions

MRI allows imaging of anatomical objects in multiple parallel sections, enabling volumetric measurements using the Simpson's rule. According to this Simpson's rule the volume of an object can be estimated by summation of the cross-sectional area's in each section multiplied by the section thickness. When there is a gap in between slices this must be corrected for and the formula for volume becomes:

$$V = \sum \{Area_i * (Thickness + Gap)\},$$

where V is the volume of the 3D object and $Area_i$ the area of the cross-section in section number i.
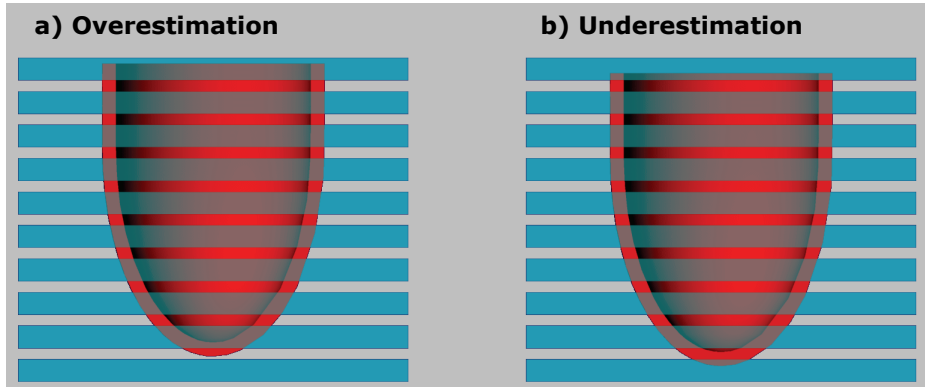
Figure 2-1 Schematic representation of a left ventricular geometry intersected by multiple parallel short-axis sections. Given the same section thickness and intersection gap both over- and underestimation of left ventricular volume may occur dependent on the position of the left ventricle with respect to the imaging slices. In situation a) the most basal slice will be included in the volumetric assessment, while in b), the most basal slice will not be taken into account since it intersect by less than 50% with the left ventricular myocardium.

While MRI is capable of directly acquiring images in any orientation, the short-axis orientation is the most commonly applied image orientation for the assessment of left ventricular chamber size and mass. The short-axis orientation has advantages over other slice orientations since it yields cross-sectional slices almost perpendicular to the myocardium for the largest part of the left ventricle[1]. This results in minimal partial volume effect at the myocardial boundaries and subsequently provides optimal depiction of the myocardial boundaries. However, the curvature of the left ventricle at the apical level leads to significant partial volume averaging. The image voxels in this area simultaneously intersect with blood and myocardium yielding indistinct myocardial boundaries. By minimizing the slice thickness - while keeping sufficient signal to noise - this partial volume effect at the apex can be reduced. Given the relatively small cross-sectional area of the left ventricle in the apical section, the error introduced due to the partial volume effect will be minimal. However, partial volume averaging at the basal level of the heart has a much greater impact since at this level the cross-sectional area of the LV is largest. The base of the LV

exhibits a through-plane motion in the apical direction during systole in the order of 1.3 cm[2,3]. Therefore, the significance of partial volume varies over the cardiac cycle. Additional long-axis views may prove helpful in determining more accurately how a basal short-axis slice intersects with the various anatomical regions.

2.2.2 Impact of slice thickness and slice gap

It is a prerequisite for the accurate assessment of the ventricular volumes that the stack of short-axis slices covers the complete ventricle from base to apex. Typically, a section thickness between 6 and 10 mm is used while the gap between slices varies from no gap (consecutive slices) to 4 mm. Quantification of volumes and mass requires the definition of contours in the images describing the endocardial and epicardial boundaries of the myocardium in several phases of the cardiac cycle. Though an image voxel may contain several tissues – due to the partial volume effect – it is assumed that the traced contours represent the geometry of the ventricle at the center of the imaged section. As shown in Figure 2-1, the partial volume effect may lead to both over- and underestimation in the assessment of ventricular volume.
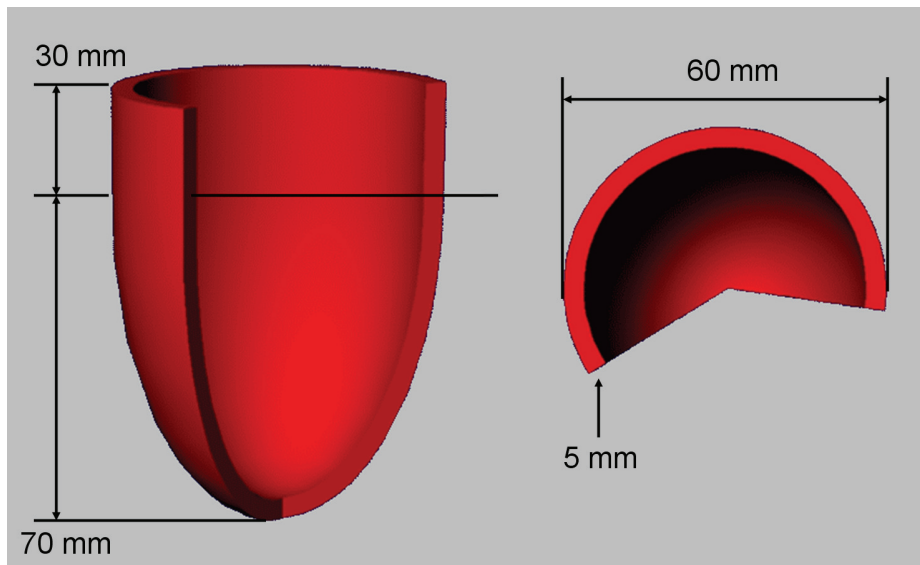
Figure 2-2. Schematic representation of the left ventricular geometry used for the simulation experiments. The phantom consists of a half ellipsoid with a length of 70 mm and an outer diameter at the base of 60 mm; at the base the shape is extended with a cylinder with a diameter of 60 mm and a length of 30 mm. The thickness of the phantom was set to 5 mm. In the experiments the size of the object was varied between the dimensions shown and 80% of this size.

With a simple experiment using synthetically created left ventricular shapes and short-axis cross-sections it can be shown how the partial volume problem may affect measurement accuracy and reproducibility. For this purpose a computer-generated average left ventricular geometry with a fixed size was constructed and short-axis cross-sections were automatically derived, while varying the position of the ventricular geometry along the long-axis direction. The shape used and its dimensions are presented in Figure 2-2. In this experiment it is assumed that the contours in a short-axis slice will only be drawn in case more than 50% of the slice thickness intersects with myocardium. The results of the simulations as depicted in Figure 2-3 demonstrate that the measurement precision (or measurement variability) degrades with increasing distance between the slices. For typical imaging parameters (section thickness 6 mm, gap 4 mm) the measurement variability is between 4 and 5%. The measurement accuracy is not dependent on the slice thickness or slice gap used: a section thickness of 10 mm with no gap results in the same variability as a section thickness of 6 mm with a gap of 4 mm.
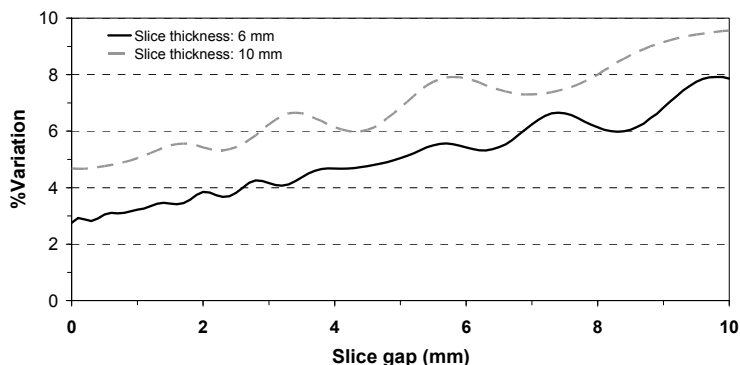
Figure 2-3. Results of volume calculation experiments using synthetically constructed left ventricular geometries. The variability of left ventricular volume estimates increases with increasing slice thickness and slice gap. For a setting of the imaging parameters, such as a thickness of 6 mm and a gap of 4 mm, the measurement variability is ~5%.

The result of this experiment has two important implications. First, variations between successive scans of the same patient may result in volumetric differences of up to 5%, which are inherent to the imaging technique used. Second, since the base of the heart has a significant through-plane motion component, the measurement variability of up to 5% will also be present over the cardiac cycle. Therefore, ejection fraction measurements will also be affected. By reducing the section thickness and the inter-section gap the variability in volumetric measurements can be reduced.
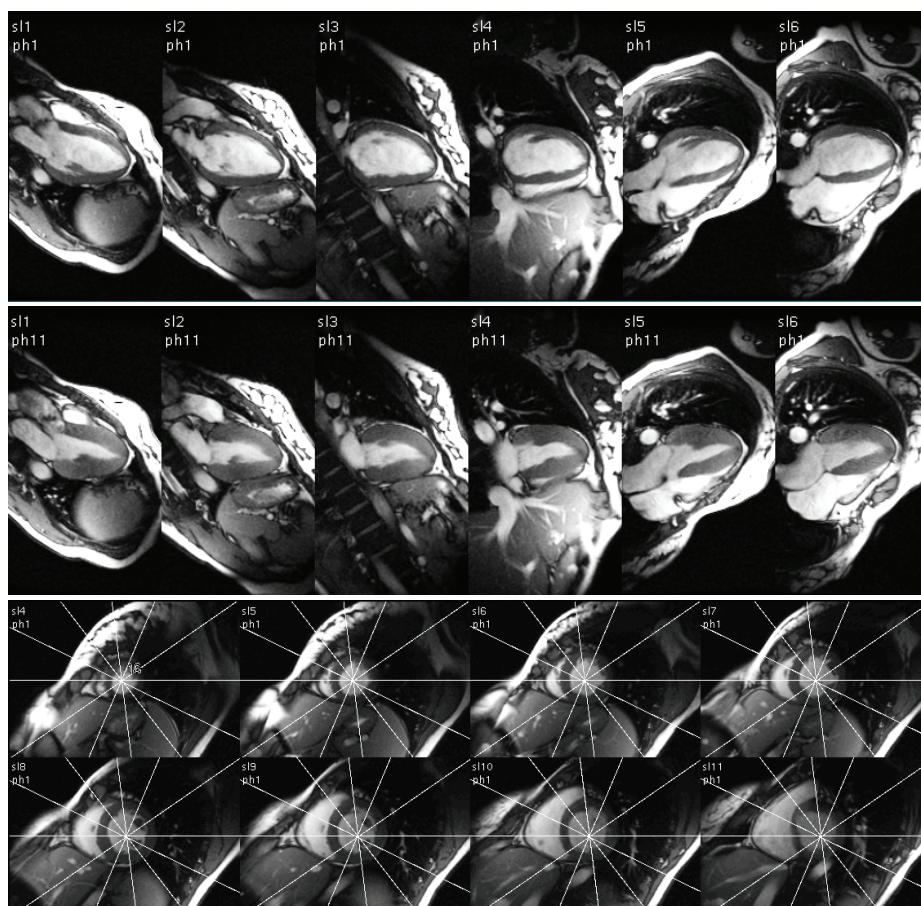
Figure 2-4. ED (top) and ES (middle) MR images acquired in radial long-axis views using SSFP MRI. Note the excellent conspicuity of the LV myocardial wall from base to apex. For reference, the white lines in the short-axis images (bottom) show the orientation of the radial long-axis views. (MR image data courtesy of M. Friedrich)

2.2.3 Global function assessment using radial long-axis views

The accuracy of volumetric measurements from multi-slice short-axis acquisitions is mainly determined by the accurate identification of the most basal slice level and the accurate definition of the endocardial and epicardial contours in this slice level. However due to the relatively large section thickness used, this is often difficult. The origin of the problem is the highly anisotropic nature of a typical short-axis examination in which the resolution in the Z-direction is much worse than the in-plane resolution. In order to overcome this limitation, Bloomer *et al*. investigated the use of multiple radial long-axis views for quantification of left ventricular volumes and mass using an SSFP MRI sequence[3]. With a radial long-axis acquisition

multiple long-axis views are acquired sharing a common axis of rotation (the LV long-axis) at equiangular intervals. This orientation has intrinsic advantages over short axis imaging as it allows clear visualization of the mitral and aortic valve planes. Additionally, long axis views suffer less from partial volume effect near the apex. After definition of the ventricular contours, calculation of LV volume is performed by adding pie-shaped volume elements defined by the location of the axis of rotation, the position of the contour and the angular interval between the image sections. Bloomer *et al*. demonstrated a good agreement between multi-slice short-axis and radial long-axis acquisitions. Importantly, as a result of the improved visualization of the myocardial boundaries and definition of the base, inter-observer agreement was better using the radial long-axis method. Clay at al. presented gender specific normal values for left ventricular volume and function parameters assessed using the radial long-axis approach[5]. Figure 2-4 illustrates examples of MR images acquired using a radial long-axis orientation. It clearly shows that the definition of the base and the contrast between blood and myocardium is excellent. Further research is needed to evaluate whether radial long-axis acquisitions also prove to be valuable for the assessment of regional function.

2.3 MYOCARDIAL MASS

The measurement of heart muscle weight is of clinical importance to properly diagnose and understand a patient's illness and condition, and to estimate the effects of treatment. To detect small changes in mass, it is of paramount importance to utilize an accurate and reproducible measurement technique. Several validation studies have been performed comparing mass estimates as derived from MR with postmortem mass measurements. In a study by Florentine *et al*. a stack of axial slices was used to quantify left ventricular mass using the Simpson rule[6]. In this early study, they found good agreement (r = 0.95, SEE = 13 g). Maddahi *et al*. carried out extensive studies in a dog model comparing several slice orientations and measurement techniques for quantifying left ventricular mass[7]. It was shown that in vivo estimates of left ventricular myocardial mass are most accurate when the images are obtained in the short-axis plane (r=0.98, SEE = 4.9 g).

2.3.1 Left ventricular mass

For the left ventricle it is generally believed and also supported by literature that the short-axis orientation is the most appropriate imaging plane. To obtain optimal accuracy and reproducibility it is important to cover the complete ventricle from apex to base with a sufficient number of slices.

Quantification of mass requires the definition of contours in the images describing the endocardial and epicardial boundaries in the stack of images. The muscle volume is assessed from these contours by applying Simpson's rule. The myocardial mass is derived by multiplying the muscle volume with the specific density of myocardium (1.05 g/cm^3).

Typically, a section thickness between 6 and 10 mm is used with an inter-section gap between 0 and 4 mm. At the apex and basal sections significant partial volume averaging will occur due to the section thickness used and tracing of the myocardial boundaries may not be trivial. Similarly partial volume averaging will cause significant difficulties in interpreting sections with a highly trabeculated myocardial wall and papillary muscles[8]. There is no general consensus on whether to include or exclude papillary muscles and trabeculae in the left ventricular mass[9-13]. While it evident that inclusion of these structures would result in more accurate myocardial mass measurements, for regional wall thickening analysis, it is important to exclude these structures to avoid artifacts in the quantification. Whether to use an end-diastolic or end-systolic time frame for the measurement of the myocardial mass is also a subject of ongoing debate. Most likely, optimal accuracy and reproducibility is obtained by averaging multiple time frames, but this will have practical objections in case contours are derived by manual tracing.

2.3.2 Right ventricular mass

For the right ventricle and also for geometrically abnormal shaped left ventricles multiple sections are required for an accurate volume assessment[14]. MRI experiments with different slice orientations in phantoms and ventricular casts have shown that no significant difference can be observed in accuracy and reproducibility between slice orientations[15]. However, in a clinical situation the choice of slice orientation also depends on the availability of a clear depiction of anatomical features that are needed to define the myocardial boundaries. Volumetric quantification of the right ventricle may be better performed on the basis of axial views[16]. This view shows improved anatomical detail and allows better differentiation between the right ventricular and atrial lumen. Nevertheless, for practical reasons, the right ventricular mass is often measured using a stack of short-axis slices which is also used for measuring the left ventricular dimensions.

2.4 QUANTIFICATION OF VENTRICULAR VOLUMES AND GLOBAL FUNCTION

Assessment of global ventricular function requires volumetric measurement of the ventricular cavities in at least two points in the cardiac cycle, being the end-diastolic (ED) and end-systolic (ES) phases. A vast amount of reports describe the applicability of MRI for accurate and reproducible quantification of left and right ventricular volumes using various MR imaging strategies[4,17]. Sufficient temporal resolution is required to properly capture the end-systolic phase. Generally a temporal resolution, or phase interval, in the order of 40-50 ms is assumed to be sufficient[18].

Chapter

2

For geometrically normal left ventricles one could rely on geometrical models to derive the volumes from one or two long-axis imaging sections. In a group of ten patients with LV hypertrophy and 10 healthy subjects, Dulce *et al*. demonstrated a good agreement between biplane volumetric measurements using either the modified Simpson's rule of an ellipsoid model and true 3D volumetric measurements using a multi-slice MRI approach[19]. In another study by Chuang *et al*. 25 patients with dilated cardiomyopathies were evaluated using both a biplane and a 3D multi-slice approach[20]. They reported a poor correlation between the two measurement methods.

For quantitative volume assessment, using multi-slice short-axis acquisitions is the most commonly applied approach. At the present state, a single section with sufficient temporal resolution can be acquired within a single breath hold, on most available MR systems. The total duration of acquiring the 8 to 12 sections required to image the entire ventricular cavity is in the order of 5 minutes[21,22]. All sections should be acquired at the same end-expiration or end-inspiration phase; otherwise reliable 3D-quantification of volumes from the obtained images is not possible.

Quantitative analysis starts with manual or (semi-) automated segmentation of the myocardium and blood pool in the images. Once contours have been defined in the stack of images describing the endocardial and epicardial boundaries of the myocardium, volumetric measurements including stroke volume and ejection fraction can be obtained by applying the Simpson's rule. Normal values for global ventricular function and mass have been reported by several investigators for different populations and pulse-sequences[23-25]. It is important to note that normal values obtained using the newer Steady State Free Precession (SSFP) type sequences differ significantly from values obtained with previous techniques. The improved contrast between blood and myocardium in SSFP is associated with larger ED and ES cavity volumes, smaller wall thickness values and lower LV mass[25-27]. In direct comparisons

of SSFP with conventional fast GRE techniques within the same individuals, differences in LV mass of up to 16.5% were reported (see Figure 2-5). In contrast, LV measurements have been shown to be relatively independent of the MR field strength used[28].

	Philips/TFE	GE/FastGRE	Siemens/FLASH
■ EDV	8.8%	9.80%	13%
▨ LV mass	-13.80%	-13.90%	-16.50%
☐ EF	3.80%	-5.30%	-10%
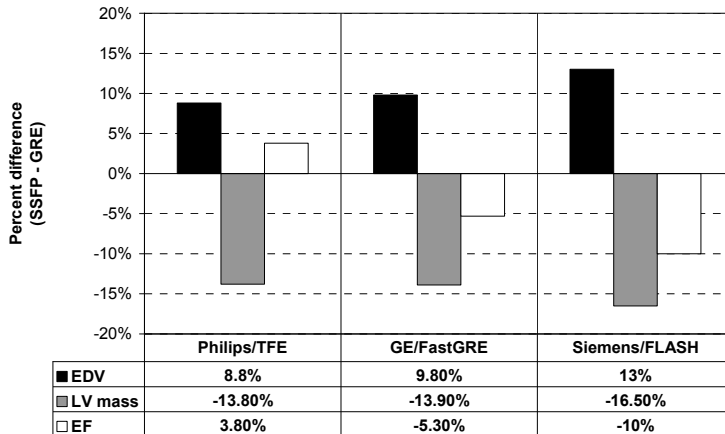
Figure 2-5. Comparison of LV dimensions measured with either a Steady State Free Precession (SSFP) sequence or a segmented GRE technique. Data derived from Alfakih et al[25], Lee et al[26] and Wei et al[27].

At the basal imaging sections, often no clear visual separation between left ventricle and left atrium is present since the imaging section may contain both ventricular and atrial cavity and muscle. It is important to realize that while the imaging sections are fixed in space, the left ventricular annulus exhibits a motion in the apical direction on the order of 1.3 cm in normal hearts[2]. Consequently, myocardium that is readily visible in an end-diastolic time frame may be replaced by left ventricular atrium in the end-systolic time frame. Additional long-axis views may be helpful to more reliably analyze the most basal and apical slice levels of a multi-slice short axis study[3]. Figure 2-6 displays end-diastolic and end-systolic time frames in a long-axis view and three basal short-axis sections obtained during a single MR examination. The white lines, indicating the intersection lines of the imaging planes, provide helpful additional information for interpreting the structures seen in the short-axis images.

Chapter 2
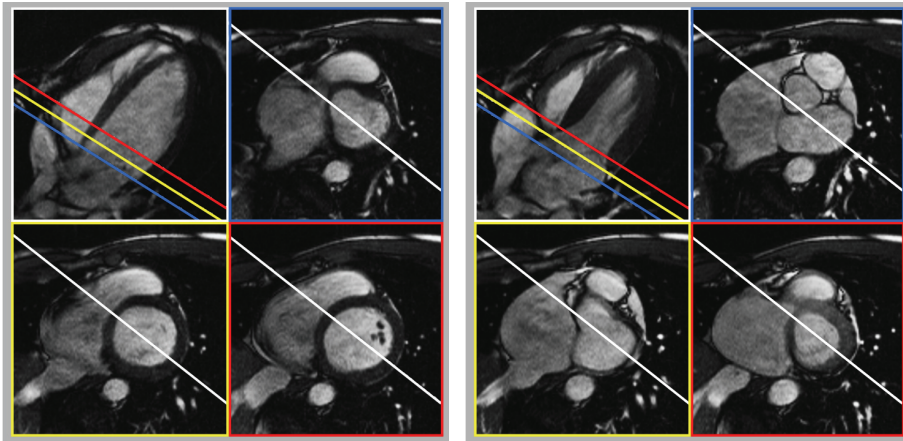
Figure 2-6. Four-chamber long-axis view and three basal level short-axis views acquired within the same examination (left: end-diastole, right: end-systole). The colored lines indicate how the short-axis and long-axis imaging planes intersect with each other. The movement of the base towards the apex in systole can easily be appreciated. The use of displays showing how long-axis and short-axis planes intersect may facilitate the interpretation of basal level short-axis images and may be valuable during tracing of the contours.

2.5 QUANTIFICATION OF REGIONAL WALL MOTION AND WALL THICKENING USING THE CENTERLINE METHOD FROM DYNAMIC SHORT-AXIS IMAGES

The excellent depiction of the endocardial and epicardial boundaries of the left ventricular myocardium forms the basis of quantitative analysis of regional myocardial function. Quantitative analysis methods for endocardial wall motion are hampered by the presence of rigid body motion of the heart. A floating centroid, based on the center of gravity of the endocardial or epicardial contours, can be used to isolate the rigid body motion from the actual endocardial deformation. On the other hand, quantification of wall thickness and thickening does not have this disadvantage. It has been demonstrated that wall thickening analysis is more sensitive in the detection of dysfunctional myocardium than wall motion analysis[29,30]. The optimal slice orientation for wall thickness analysis of the left ventricle is the short-axis plane since in this orientation the major part of the myocardial wall is perpendicular to the imaging section[29-33]. Local wall thickness can be derived in these acquisitions from manually or automatically defined endocardial and epicardial boundaries in each short-axis image. Radial wall thickness quantification methods use an approximate center point in the left ventricle to measure the distance between the endocardial and epicardial contours along radial lines starting from this center point. This approach may result in significant

overestimation of wall thickness in case the ventricular cross-section deviates much from a circular shape. The Centerline method has advantages over the radial methods since it can be applied for a wide variety of shapes. In fact, it was originally developed for wall motion analysis in X-ray angiograms and later modified for wall motion and wall thickness analysis of left ventricular short-axis views[35,36].
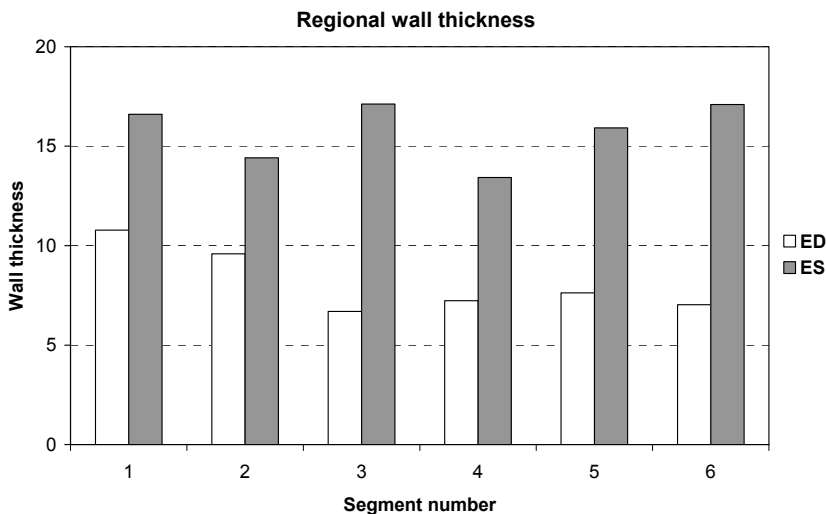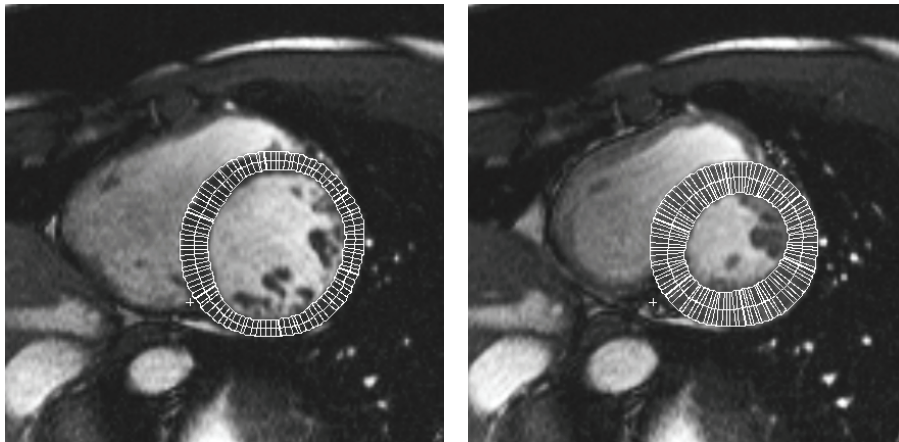
Figure 2-7. Mid-ventricular end-diastolic (top left) and end-systolic (top right) short-axis images of the left ventricle with endocardial and epicardial contours defined. Wall thickness chords are constructed for measurement of wall thickness in six myocardial segments. The segments are defined starting at the posterior junction of the right ventricular wall with the left ventricle. Segments are numbered from 1 through 6 in clockwise order. The graph in the bottom panel presents the wall thickening in each of the six defined myocardial segments.

As depicted in Figure 2-7, the centerline method uses a path in between the endo- and epicardial contours (the "centerline") and perpendicular to that path at evenly spaced intervals, starting at a clearly visible anatomical reference point chords are constructed from endocardium to epicardium. The length of such a chord represents the local wall thickness and the ratio between the end-systolic and end-diastolic chord length equals the local end-systolic wall thickening. A sufficient number of chords should be chosen such as not to miss small anatomical abnormalities. Normal values for end-systolic wall thickening can be used for comparison to determine which myocardial regions are abnormal; subsequently the size, extent and severity of a wall thickening abnormality can be quantified[36]. In case the MRI slice is not exactly perpendicular to the local myocardial orientation, the normal two-dimensional centerline method may lead to a wall thickness overestimation. Buller *et al*. describe a method to correct for this error by estimating the local angle between the imaging plane and the myocardial wall for each centerline chord[37]. They demonstrated the improved accuracy of this method in phantom studies and also showed that the overestimation of wall thickness near the apex of the heart in short-axis studies can be minimized.

To facilitate the interpretation of the large amount of quantitative data of regional ventricular function, optimized visualization methods need to be implemented. When standardized imaging protocols are applied, normal value databases can be established for the various parameters providing more objective assessment of the observed regional function abnormalities. Bull's eye plots, as known from nuclear medicine, can be used as a visual tool to present all the relevant information in just one single graphical display. A further step is to employ three-dimensional reconstruction techniques to generate displays showing regional function data in relation to the anatomy of the patient. Figure 2-8 shows an example of such a display, providing views of the left ventricular anatomy of a patient with an antero-septal infarction.
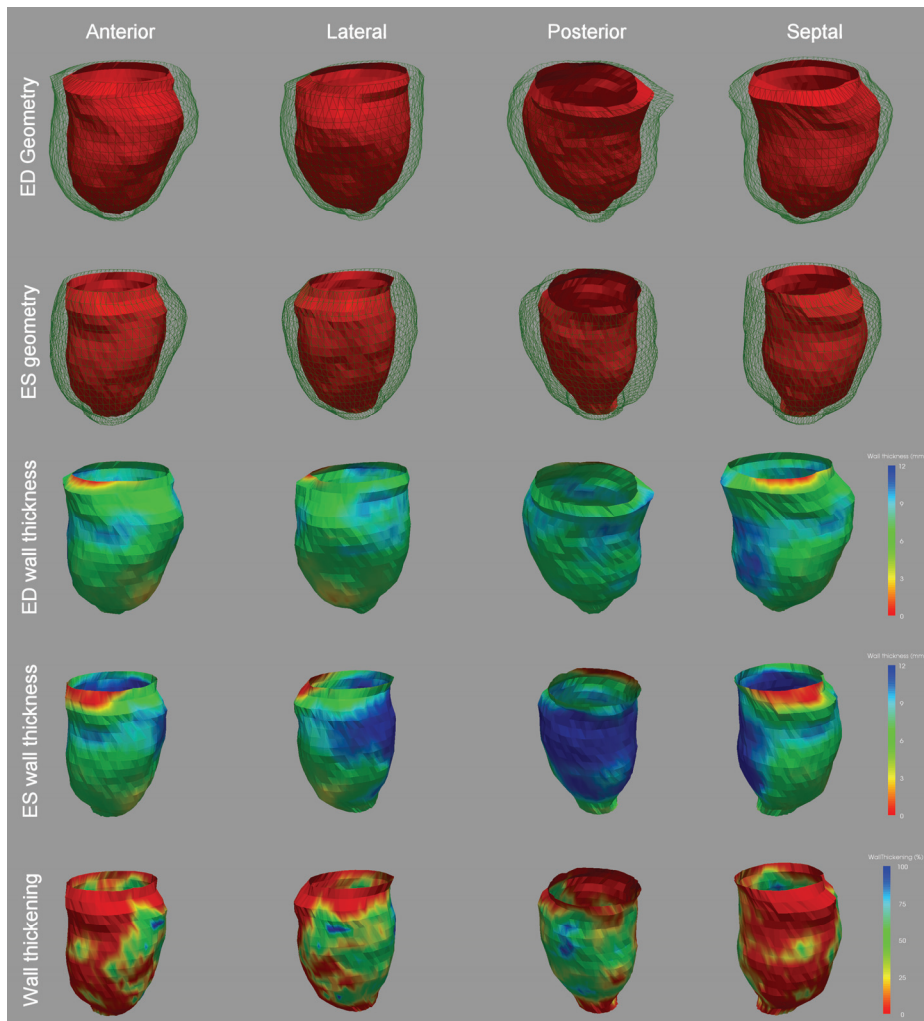
Figure 2-8. Three-dimensional reconstruction of the left ventricle from a multi-slice short-axis study of a patient ten days after acute antero-lateral infarction. The top two rows show the ventricular geometry at the ED and ES phases. The bottom three rows show the ED wall thickness, the ES wall thickness and ES wall thickening using a color-coding.

2.6 REGIONAL FUNCTION ANALYSIS USING MRI TAGGING AND VELOCITY-ENCODED MRI

Wall thickening and wall motion analysis from conventional cine MR imaging suffers from the through-plane motion of the heart. Furthermore, conventional cine MRI only allows quantification of radial myocardial deformation. Three-dimensional myocardial tagging is a powerful MRI

technique that allows quantification of myocardial strain in all three dimensions. With the use of MRI tagging, cine MR images are acquired with a superimposed parallel, rectangular or radial grid of dark saturation lines. These tagging lines are induced by a special pre-pulse sequence immediately following the R-wave of the ECG and can subsequently be followed over the cardiac cycle. Dedicated computer algorithms have been developed to automatically track the intersection points of the tagging lines over the cardiac cycle to be able to quantify intramural myocardial deformations[38]. By applying this technique in multiple slices in both short-axis and long-axis directions, 3D-strain measurements can be performed[39]. Alternatively, these measurements can be derived directly by processing of the Fourier spectrum of the tagged MR data, a technique currently known as HARmonic Phase (HARP) imaging[40,41].
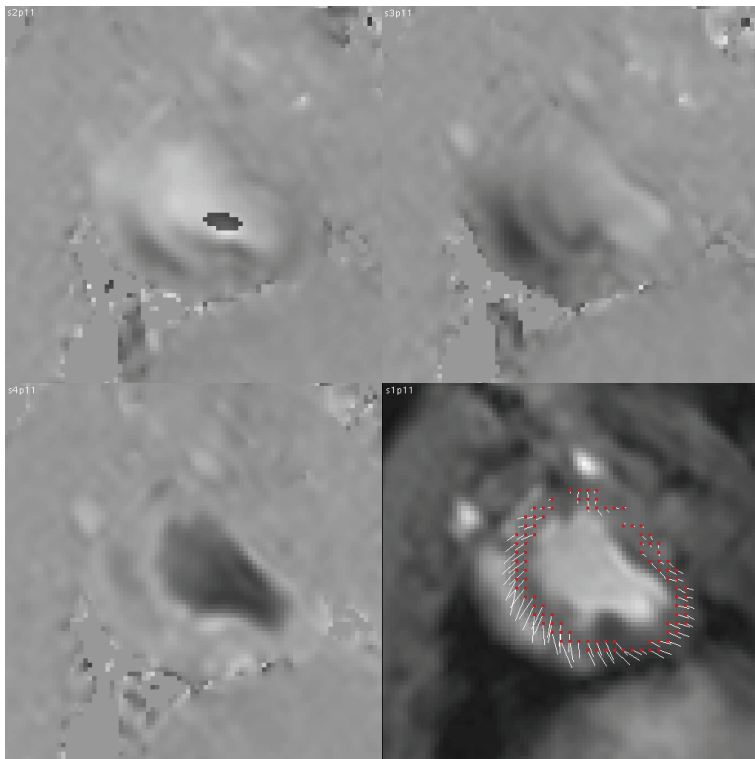
Figure 2-**9.** Short-axis images obtained by phase-contrast cine MRI at early diastole. The images are obtained from a pig after acute myocardial infarction. The velocity images (x, y, z) depict the myocardial velocities in x, y and z direction using a gray-scale encoding. The in-plane velocity vectors (v) are reconstructed from the x- and y-velocity maps and show both the direction and magnitude of myocardial velocity. The relatively low velocities in the anterio-lateral region illustrate the diastolic function abnormality in this region.

Velocity-encoded cine MRI may be used to quantitatively assess the three-dimensional velocity of the myocardium over the cardiac cycle. With this acquisition technique the myocardial velocities can be measured in three orthogonal directions for each pixel within the imaging plane[42-44]. In contrast to MR tagging methods, this technique can be used in combination with retrospective gating such that data over the complete cardiac cycle is obtained. For quantitative analysis two different approaches can be followed. Motion tracking techniques, which are based on velocity integration, can be applied to obtain two- or three-dimensional trajectories of myocardial sample points[45]. An alternative approach is the direct quantification of myocardial strain-rate by calculating the spatial velocity gradient along different directions[46]. Both approaches are sensitive to imperfections of the images such as insufficient temporal or spatial resolution, blood-related artifacts and beat-to-beat variations. These problems may well be resolved by future improvements in image acquisition techniques.

2.7 Automated contour detection in short-axis multi-slice cine MRI

Despite the fact that the time required for image acquisition has been reduced tremendously over the last few years, a cardiac evaluation based on CMR including quantitative analysis remains time consuming due to the required post processing of the large amount of images. Assuming a ventricle which is imaged in ten imaging sections, twenty endocardial contours need to be defined for the assessment of basic global function parameters such as the ejection fraction and stroke volume. Ten addition epicardial contours are needed for quantification of left ventricular mass. Manual image analysis requires tracing of these myocardial outlines which is a time-consuming procedure that takes between 10 minutes and one hour depending on the software used. It also may introduce undesirable inter- and intraobserver variabilities.

A considerable number of groups, including ours, have contributed to the development of algorithms for the automated extraction of the left ventricular myocardial outlines from short-axis cine MR imaging studies[47-61]. The development of automated contour detection algorithms is a challenging problem because variations in gray value in MRI depend on many factors such as the imaging parameters used, spatial dependency in case surface coils are used and flow dependency. Additionally, the geometry of the cardiac chambers and its contraction pattern may be abnormal in pathological situations, causing automated segmentation methods that rely too much on an expected shape or contraction pattern to fail in such circumstances. Ideally, an automated algorithm should be

insensitive to variations in image characteristics and be applicable to MR images obtained from different MR scanners. In case the algorithm can operate without any user-interaction, the actual computation time is not of major importance. If user interaction is required to control the algorithm, such as providing seed points or initial contours for each of the imaging slices, the actual algorithm should be must faster to increase the time efficiency of the operator.
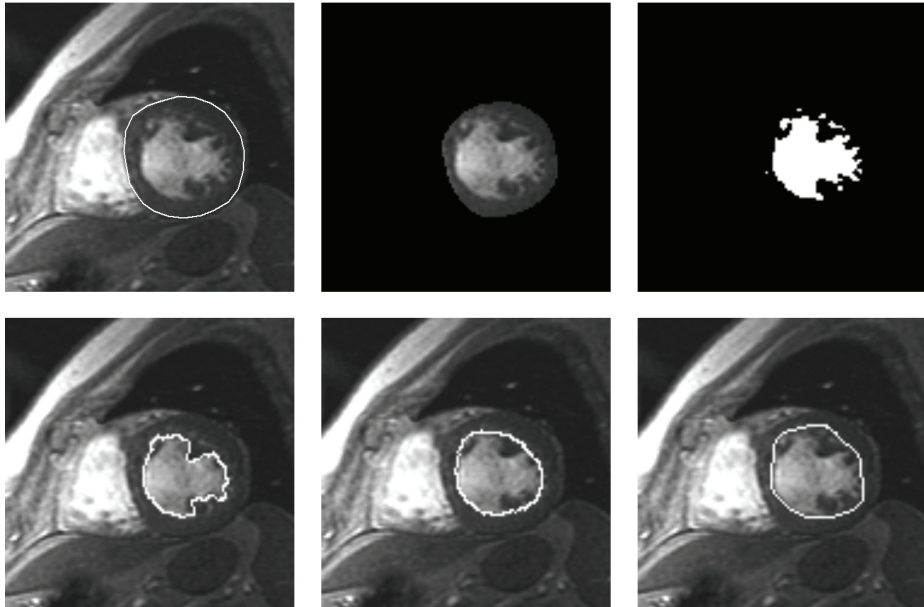
Figure 2-10. Automated detection of the endocardial contour. A) Original image with epicardial contour; B) Search region for the endocardial contour. The region outside the epicardial contour and a small region at the inside of the epicardial contour is masked out from the original image; C) Result after determination of the optimal threshold; D) Contour around the thresholded region serves as a starting contour for the subsequent edge-based contour detection; E) When papillary muscles needs to be excluded from the myocardium, a smooth convex hull contour around the initial contour is determined; F) Final result after minimum cost contour detection.

In the next section a short description is given of the underlying methods and validation results from the algorithms developed at our laboratory which have been integrated in a software package, MASS[51]. Our contour detection method follows a model-based approach and is directed to the definition of the endocardial and epicardial contours in all the phases and slices of an imaging study. The amount of user-interaction required to obtain reliable contours is limited, and is minimal in case the images are of good quality. The algorithm accommodates for anatomical and MRI related

variations in image appearance by providing a certain learning behavior. Manually traced or edited contours are assumed to be correct and the contour detection algorithm was designed to generate a consistent set of contours for the total image dataset using the manually defined contours as models. The contour detection starts by searching for circular objects in the imaging slices to find the approximate long axis of the left ventricle, which result in an approximate left ventricular center point in each image. Using this center point, epicardial contours are found in the first phase and subsequently in the remaining phases using a frame-to-frame contour detection procedure. This frame-to-frame epicardial contour detection procedure is based on matching of line profiles that are positioned perpendicularly to the model contour (derived from the first phase) and then automatically positioned at the corresponding tissue transitions in other phases within the same slice level. By this approach the algorithm is able to deal with the fact that the epicardial boundary of the myocardium is adjacent to regions having different gray value characteristics. A first estimate of the endocardial contour is found using an optimal thresholding technique within the region described by the epicardial contour. The final endocardial contour is found by using a model-based edge-detection technique, known as the Minimum Cost Algorithm[62]. Figure 2-10 illustrates the algorithmic steps that are carried out to detect an endocardial contour given an image with an available epicardial contour.

2.7.1 Automated contour detection optimization for different MR pulse sequences

A major challenge when designing and implementing a reliable automated contour detection algorithm is to deal with the large variations in image characteristics due to differences in MR pulse sequences used, the usage of different receiver coils and differences between MR scanners from different vendors. Consequently, for optimal performance, an automated segmentation method needs to be optimized for a specific type of acquisition procedure. We have recently developed a contour detection optimization procedure, which enables tuning the different parameters that control the automated contour detection[63]. Figure 2-11 illustrates the mechanism of the contour detection tuning method. Based on a set of short-axis exams with expert drawn reference contours available, automated contour detection is performed using different settings of the contour detection procedure. Contour detection settings that are varied are the convolution kernels that are used for edge detection in the images, parameters that control the smoothness of the detected contours and many others. The automatically detected contours generated using a specific

parameter setting are compared to the reference contours by computing the degree of similarity between both contour sets. A Genetic Algorithm is used to generate new sets of parameter settings based on the results of the previously evaluated sets. By iterating this procedure numerous times, an optimal set of parameters can be found for a specific set of images. The degree of similarity, which is used to evaluate the quality of the detected contours, is defined as the percentage of contour points that lie within a 2 mm distance of the corresponding reference contour. It was shown that for SSFP type acquisitions, the degree of similarity for manually traced endocardial contours obtained by repeated analysis of the same observer was 77%. Therefore, since the reference contours are generated manually, the similarity between automatically detected contours and the reference contours has a theoretical upper bound of 77%. The described optimization approach was evaluated on a set of 30 SSFP examinations from the three main MR scanner vendors to assess the improvement in the performance of automated contour detection. In all 30 studies endocardial contours were carefully traced in the end-diastolic and end-systolic phases which were used as reference. Automated contour detection was performed in all studies with and without optimized settings. When using the unoptimized settings the average degree of similarity was 49.5%, which increased to 63.3 percent when using the optimized settings.
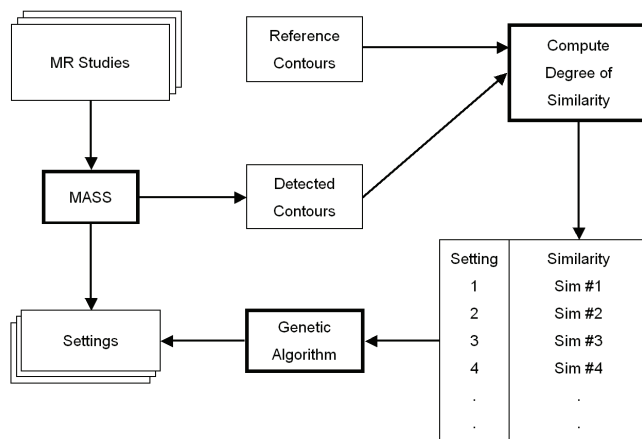
Figure 2-11. Diagram of the automated optimization procedure to find the optimal contour detection settings for a specific pulse sequence. In an iterative procedure, MASS performs automated contour detection in a set of MR studies using a number of different parameter settings. The detected contours are compared to manually defined reference contours and the average degree of similarity is computed for each parameter setting. A Genetic Algorithm is used to generate new parameter settings based on the results of the parameter settings from the previous iteration.

2.7.2 New model-based automated segmentation methods

Reliable fully automated contour detection, not requiring any user interaction, would clearly be an important step to further improve the clinical utility of CMR. Despite a lot of research in this area, two major problems limit the success rate of many of the previously described contour detection strategies for cardiovascular structures. First, due to the presence of noise and image acquisition artifacts, image information can be ill defined, unreliable or missing. In these cases a human observer is still capable of tracing the myocardial contours in the image data based on experience and prior knowledge, while many automated techniques fail. Second, a contour as drawn by an expert human observer may not always correspond to the location of the strongest local image evidence. In particular, in short-axis images the papillary muscles and trabeculae pose a problem. For example, many experts prefer to draw the left ventricular endocardial border as a convex hull around the blood pool, at a location somewhat 'outside' of the strongest edge[64,65]. A second example is the epicardial boundary, which may be embedded in fatty tissue, as a result of which the edge is strongest at the fat-air transitions. However, often the contour should be drawn on the inside of this fatty layer, an intensity transition that is marked by only a faint edge. Therefore, a decision about the exact location of the contour cannot always be made based on the strongest image evidence, but should be learned from the examples and preferences provided by expert observers.

To overcome these problems, prior knowledge about the image appearance, spatial organ embedding, characteristic organ shape and its anatomical and pathological shape variations should form an integral part of a contour detection approach. Moreover, it should be adaptive to accommodate for the preferences of an observer and to be easily adjustable to image characteristics of various pulse sequences and MR systems. Recently, Cootes *et al*. introduced the concept of Active Appearance Models (AAM's), which are trainable mathematical models that can learn the shape and appearance of an imaged object from a set of example images[66]. This method was originally developed for facial recognition and later optimized for the detection of the left ventricle in CMR[67]. An AAM consists of two components: a statistical model of the *shape* of an object, which is combined with a statistical model of the *image appearance* of the object in a set of example images. The combined model is trained to learn the shape and image structure of an organ from a representative set of example images from different subjects. The AAM can be automatically matched to a new study image by minimizing an error function expressing the difference between the model and the underlying

image evidence. During this matching process, the model is constrained to only resemble statistically plausible shapes and appearances. Consequently, AAM's are able to capture the association between observer preference and the underlying image evidence, making the AAM's highly suitable to model the expert observer's analysis behavior. Moreover, AAM's can model multiple objects (in our case the left- and right cardiac ventricles) in their spatial embedding. In a study by Mitchell *et al*. this AAM technique showed excellent agreement with manually defined contours, both for the left- and right ventricle simultaneously[68]. Figure 2-12 shows examples of automatically detected contours for the left and right ventricle obtained using this approach. Van der Geest *et al*. investigated the value of incorporating image information of complete time-series in an AAM based contour detection method[69]. The advantage of this approach lies in the fact that information from a complete time-series is used during training and detection, which results in consistent time-continuous segmentation results, even in the presence of image frames with poor image quality.

Another interesting recent development is the use of three-dimensional statistical shape models for ventricular image segmentation. For example van Assen et al have successfully applied 3D Active Shape Models (ASM) for myocardial boundary detection in multi-slice short axis MR studies[70].
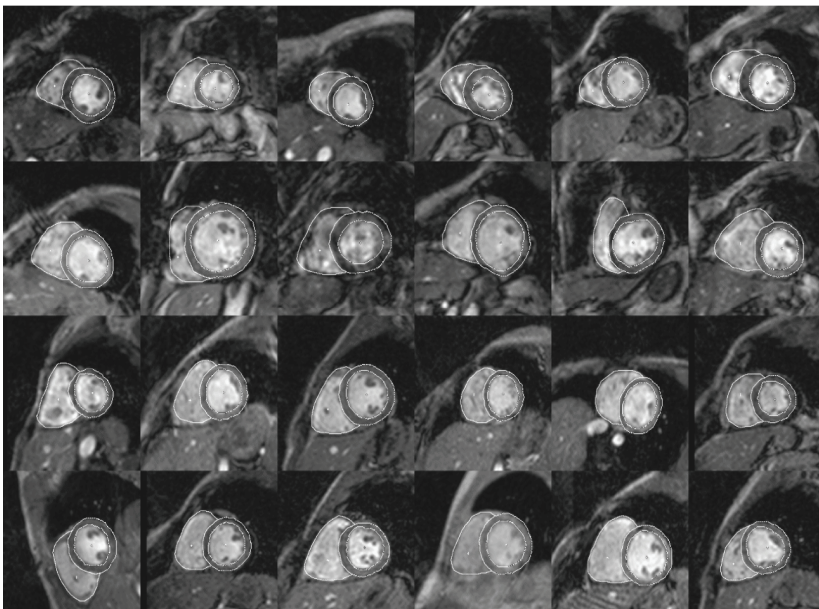
Figure 2-12. Examples of detection results of left and right ventricular contours using the Active Appearance Model contour detection method.

2.8 MRI FLOW QUANTIFICATION

Velocity-encoded cine MRI (VEC-MRI) also plays an important role in the evaluation of global ventricular function. The accuracy of this imaging technique has been demonstrated in *in-vitro* experiments using flow phantoms and comparison against other imaging techniques such as Doppler echocardiography and invasive oximetry[71,72]. Since flow measurements are obtained at high temporal resolution over the complete cardiac cycle, VEC-MRI is especially useful in the evaluation of left and right ventricular diastolic function parameters by measuring flow over the atrio-ventricular valves. Application of this technique to the proximal portion of the ascending aorta or pulmonary artery allows the assessment of left and right ventricular systolic function. After the cross section of a vessel is identified in the image by manual or automated contour detection, the instantaneous flow rate within the vessel cross section is obtained by multiplying the average velocity within the contour by its area. Ventricular stroke volume measurements are derived by integrating the flow over a complete cardiac cycle[73]. The presence of aortic or pulmonary regurgitation can be easily identified and quantified from the derived flow curve. VEC-MRI has an established role in the evaluation of patients with congenital heart disease[74-77]. Figure 2-13 illustrates how MR flow measurement can be used for quantification of shunt size in a patient with a ventricular septal defect.

2.8.1 Automated quantification of aortic flow

Application of VEC-MRI to the proximal portion of the ascending aorta allows the assessment of left ventricular systolic function by evaluating the flow over a complete cardiac cycle. Such a study requires a VEC-MRI acquisition in the transversal plane crossing the ascending aorta. The left ventricular stroke volume can be measured by integrating the flow over a complete cardiac cycle. For an accurate assessment of volume flow, contours describing the lumen of the vessels have to be obtained in the images. The in-plane motion of the greater vessels and changes in shape of the vessel cross section over the cardiac cycle would require the user to trace the luminal border of the vessel in each individual phase of the MR examination. To overcome these practical limitations, an automated analysis method was developed in our department to automatically detect the required contours in each of the cardiac phases[78]. This contour detection algorithm was integrated in the FLOW software package.
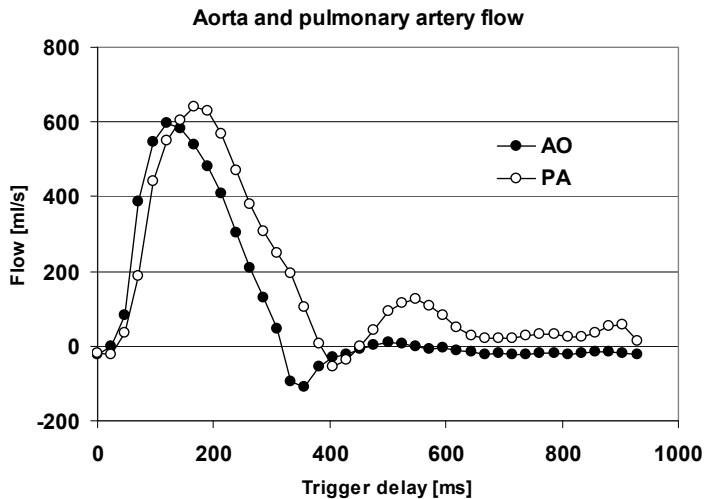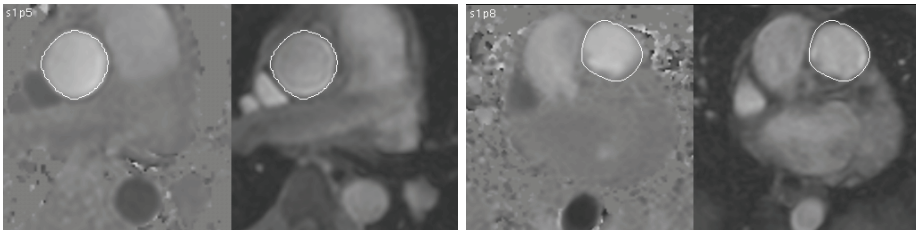
Figure 2-13. Flow velocity maps of the ascending aorta (top left) and pulmonary artery (top right) with contours defined of a patient with a ventricular septal defect. From the derived flow curves (bottom) of the respective arteries the shunt size can be accurately quantified. In this patient the aortic flow was quantified as 87 ml/heart beat (5.6 L/min) and the pulmonary flow 149 ml/heart beat (9.4 L/min).

The only user-interaction required, is the manual definition of an approximate center in one of the available images. In this first image an initial model contour is detected using gray value and edge information. The position of the same vessel at another time frame can be estimated by shifting the model contour in a limited region around the initial location and examining the edge values measured in the modulus image along the contour points. An algorithm was developed which finds the most likely contour position for each time frame, with the restriction that a contour is only allowed to displace 2 pixels (1.6 mm) from phase to phase, thereby imposing a temporal continuity of the motion. After having found the correct contour location, a final optimized contour was detected by allowing small deformations of the model contour such that it would follow the edges in the modulus image. For this purpose a two-dimensional graph searching technique was used. The resulting contour was dilated by one pixel to be sure to encompass the complete region with flowing blood. The

total contour detection process takes less than ten seconds for a study with 30 cardiac phases.

Validation was performed on flow velocity maps from a study population of 12 healthy volunteers. Two independent observers performed manual and automated image analyses. The first observer repeated the automated and manual analyses after a two-week interval to avoid learning effects. The time required for manual analysis was 5-10 minutes. During automated analysis the user had to identify the approximate location of the center of the aorta in one of the available images. The total analysis time for automated analysis was less than 10 seconds. Stroke volume measurements were obtained by integrating the flow over the complete cardiac cycle. The mean left ventricular stroke volume obtained by VEC-MRI in the group of 12 volunteers was 86.4 ml (SD: 13.6 ml). No statistically significant differences were found between the results of manual and automated analyses. The mean difference between automated and manually assessed stroke volume was 0.78 ml (SD: 1.99 ml). The intra-observer variability was 0.65 ml for manual analysis and 0.58 ml for automated analysis; the intra-observer variability was 0.99 ml for manual analysis and 0.90 ml for automated analysis. From this study, it can be concluded that the automated contour detection algorithm performs equally well as the manual method in the determination of left ventricular stroke volume derived from VEC-MRI studies of the ascending aorta.

2.9 IMAGE PROCESSING OF PERFUSION IMAGING STUDIES

First-pass contrast-enhanced MR perfusion imaging is used to detect abnormalities in myocardial blood flow, related to coronary artery disease. Typically, three to five short axis slices of the heart are acquired over 5 to 10 seconds prior to the injection of the intravenous contrast bolus, and about 60 seconds after the injection of contrast. A combination of stress and rest acquisitions can be performed to improve the differentiation of normal from abnormally perfused myocardial territories[79].

Various approaches have been described to obtain quantitative indices of myocardial perfusion from first-pass MR perfusion studies[80-82]. Jerosch-Herold *et al*. have performed extensive studies to demonstrate the feasibility of absolute perfusion quantification in ml/gram tissue/minute and have validated these methods in animal experimental studies[80]. However, more commonly, semi-quantitative analysis methods are being used. An example of a semi-quantitative approach is to use the maximal upslope of the myocardial time-intensity curve as index of myocardial perfusion. Although less-advanced, the diagnostic accuracy of the technique has been

validated against competing non-invasive and invasive modalities in single center and multicenter studies[83-85].

To derive quantitative indices related to the presence or absence of myocardial perfusion deficits, time-intensity curves need to be evaluated for regions in the myocardium. Due to the significant patient motion over the acquisition duration, time-intensity curves which are derived from a static region in the image are severely distorted. Automated image co-registration techniques have been developed to correct for this motion[86-89]. Once the images are registered, endocardial and epicardial contours can be traced in one image frame and copied to the other frames. Subsequently, time-intensity curves can be easily generated for multiple regions in the myocardium. Although these curves can be determined at a pixel level, the noise level in the images is often not sufficient to derive reliable perfusion indices at this level of detail. More typically 4 to 8 segments are defined for each imaging section, which can be further sub-divided into an endocardial and an epicardial layer[85].
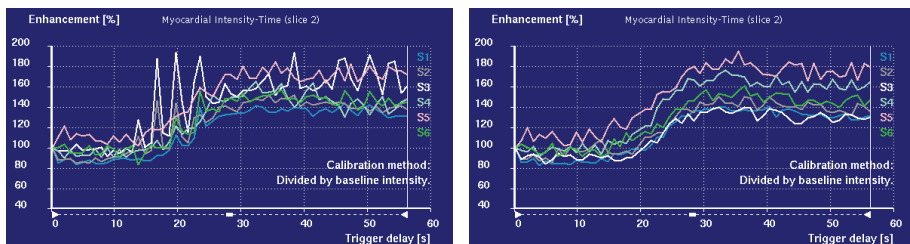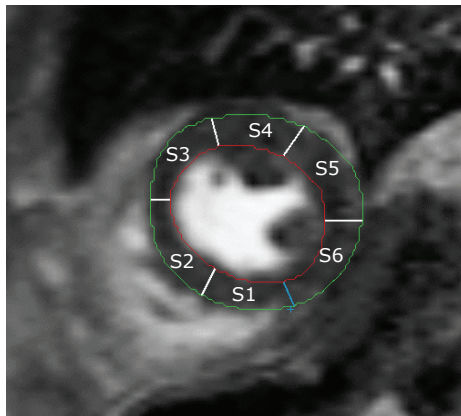
Figure 2-14. Signal-intensity versus time curves for 6 segments of the left ventricular myocardium at a mid ventricular slice level. Without motion correction (lower left) the curves are not suitable for quantitative analysis. After motion correction (lower right), perfusion indices such as maximum upslope can be derived reliably.
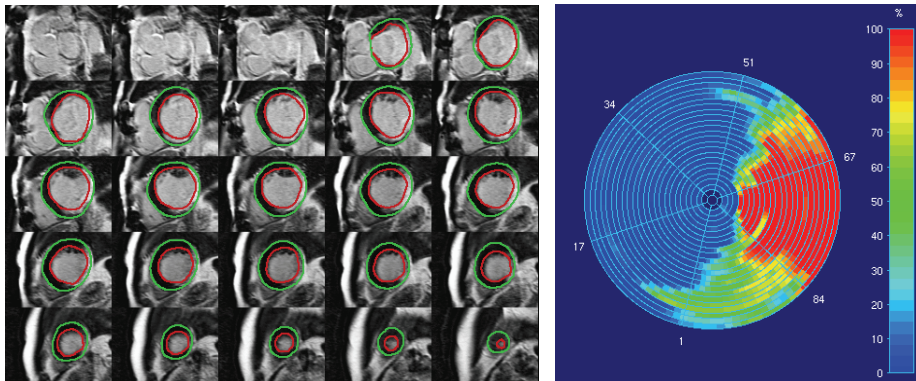
Figure 2-15. Example multi-slice short-axis LGE acquisition (left). After defining an appropriate intensity threshold, the regional transmurality of scar can be computed and visualized using a bull's-eye plot (right). This patient has a large infarction with complete transmural enhancement in the lateral region and sub-endocardial enhancement in the posterior region.

2.10 LATE GADOLINIUM ENHANCED MRI

Late gadolinium enhanced (LGE) MRI has become part of a standard MRI examination as it is extremely valuable for the assessment of viable and non-viable myocardium in infarcted and poor contractile areas[90,91]. The excellent resolution of MRI enables the depiction of both transmural and non-transmural regions of infarction. It was shown that the transmural extent of enhancement is inversely related to the likelihood of recovery of function after revascularization. Therefore, large non-transmural infarcts may have a better prognosis than relatively small transmural infarcts. Quantification of the size and distribution of the infarction involves defining a signal intensity threshold that separates normal myocardium from enhanced tissue. Various approaches have been suggested for determining the optimal intensity threshold. In the pioneering work of Kim et al. hyper-enhanced regions were defined as those regions having an intensity value >2D above the mean of the remote normal myocardium[90.] Other authors have suggested slight modifications to this approach by proposing adding 2-5 times the standard deviation[93,94]. These observations demonstrate the sensitivity of the SD-method to differences in image acquisition protocol. Schuijf *et al*. and Amado *et al*. proposes to use a Full Width Half Maximum (FWHM) criterion to objectively obtain a threshold value[95,96]. Amado *et al*. demonstrated in an animal experimental study that myocardial infarct size measurements using a FWHM criterion agreed very well with pathology[96]. The inherent properties of the Full-Width-Half-Max method makes it much less sensitive to variations in image acquisition parameters. Based on this criterion Hsu et al. developed a fully automated technique to obtain

accurate assessment of the size of myocardial infarction and validated this approach in an animal experimental setting[97]. Using the defined threshold, the enhanced regions within the myocardium are objectively defined and the regional degree of transmurality can be defined as illustrated in Figure 2-15.

2.11 INTEGRATED IMAGE ANALYSIS

The increasing routine clinical use of CMR and the overwhelming size of the typical CMR image data sets pose a significant challenge for time-efficient image quantification and interpretation. Multiple software packages with automated image segmentation and quantification methods have been introduced in the last decade to support the work of the clinician. However, these solutions primarily focus on particular elements within a CMR exam, such as the assessment of global function or myocardial perfusion. An integration of the available techniques for CMR image analysis into an integrated solution for the analysis of all the data acquired in a comprehensive CMR exam would be a major step forward. The work by Hennemuth *et al*. demonstrates the feasibility of such integrated image analysis solutions[98].

An example of an integrated analysis approach is provided in Figure 2-16. It illustrates how quantitative information obtained form two different MR acquisitions can be combined. In this example LGE MRI is combined with cine MRI information to relate infarct transmurality to the regions with poor contractility. This enables classification of regions of poor contractility into viable and non-viable regions.

2.12 CONCLUSION

Cardiovascular MRI is a valuable technique for non-invasive quantitative assessment of global and regional ventricular function. Computerized image analysis techniques can help reducing the time required for quantification and interpretation of the many images. In this chapter, analytical methods for left ventricular function and vascular flow measurements based on automated contour detection approaches have been described. Validation studies of these methods have confirmed their accuracy, precision, robustness and usefulness for clinical research studies. Fully automated contour detection methods that operate reliably in a routine clinical environment are needed and may become available in the near future.
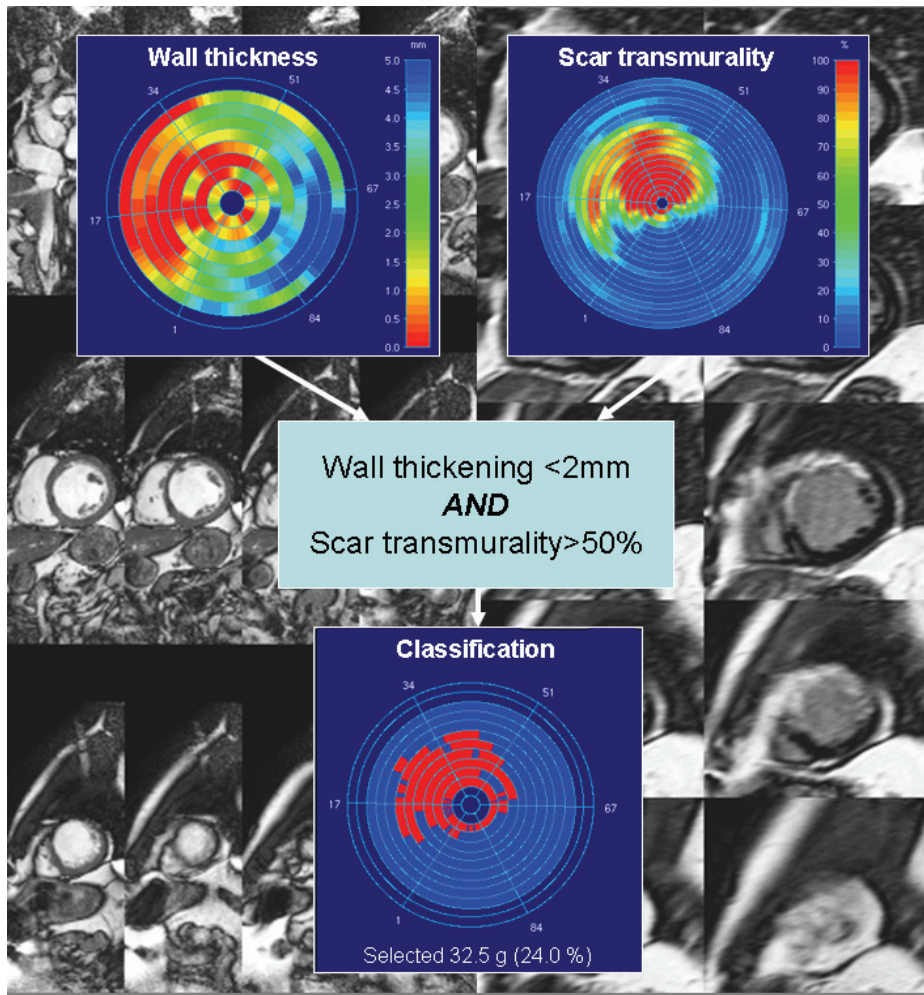
Figure 2-16. Data fusion between wall thickening information derived from cine MR and a scar transmurality derived from LGE MRI visualized using a bulls-eye displays. The red area in the bottom bull's-eye represents the non-viable myocardium where the wall thickening is less than 2 mm while scar transmurality is >50%.

2.13 REFERENCES

1. Cottin Y, Touzery C, Guy F, Lalande A, Ressencourt O, Roy S, Walker PM, Louis P, Brunotte F, Wolf JE. MR imaging of the heart in patients after myocardial infarction: effect of increasing intersection gap on measurements of left ventricular volume, ejection fraction and wall thickness. Radiology 1999; 213:513-520.
2. Rogers WJ, EPS, Weiss JL, Buchalter MB, Rademakers FE, Weisfeldt ML, Zerhouni EA. Quantification and correction for left ventricular systolic long-axis shortening by magnetic resonance tissue tagging and slice isolation. Circulation 1991; 84:721-731.

3. Marcus JT, Götte MJW, de Waal LK, Stam MR, van der Geest RJ, Heethaar RM, van Rossum AC. The influence of through-plane motion on left ventricular volumes measured by magnetic resonance imaging: implications for image acquisition and analysis. J Cardiovasc Magnetic Resonance 1998; 1:1-6.

4. Bloomer TN, Plein S, Radjenovic A, Higgins DM, Jones TR, Ridgeway JP, Sivananthan MU. Cine MRI using steady state free precession in the radial long axis orientation is a fast accurate method for obtaining volumetric data of the left ventricle. J Magn Res Imag 2002; 14:685-692.

5. Clay S, Alfakih K, Radjenovic A, Jones T, Ridgway JP, Sinvananthan MU. Normal range of human left ventricular volumes and mass using steady state free precession MRI in the radial long axis orientation. MAGMA 2006;19:41-45.

6. Florentine MS, Grosskreutz CJ, Chang W, Hartnett JA, Dunn VD, Ehrhardt JC, Fleagle SR, Collins SM, Marcus ML, Skorton DJ. Measurement of left ventricular mass in vivo using gated nuclear magnetic resonance imaging. J Am Coll Cardiol 1986; 8:107-112.

7. Maddahi J, Crues J, Berman DS, Mericle J, Becerra A, Garcia EV, Henderson R. Noninvasive quantitation of left ventricular mass by gated proton magnetic resonance imaging. J Am Coll Cardiol 1987; 10:682-692.

8. Matheijssen NAA, Baur LHB, Reiber JHC, van der Velde EA, van Dijkman PRM, van der Geest RJ, de Roos A. Assessment of left ventricular volume and mass by cine-magnetic resonance imaging in patients with anterior myocardial infarction intra-observer and inter-observer variability on contour detection. Int J Cardiac Imag 1996; 12:11-19.

9. Sievers B, Kirchberg S, Bakan A, Franken U, Trappe HJ. Impact of papillary muscles in ventricular volume and ejection fraction assessment by cardiovascular magnetic resonance. J Cardiovasc Magn Reson. 2004;6:9-16.

10. Papavassiliu T, Kühl HP, Schröder M, Süselbeck T, Bondarenko O, Böhm CK, Beek A, Hofman MM, van Rossum AC. Effect of endocardial trabeculae on left ventricular measurements and measurement reproducibility at cardiovascular MR imaging. Radiology. 2005;l;236:57-64.

11. Vogel-Claussen J, Finn JP, Gomes AS, Hundley GW, Jerosch-Herold M, Pearson G, Sinha S, Lima JA, Bluemke DA. Left ventricular papillary muscle mass: relationship to left ventricular mass and volumes by magnetic resonance imaging. J Comput Assist Tomogr 2006;30:426-432.

12. Kirschbaum S, Aben JP, Baks T, Moelker A, Gruszczynska K, Krestin GP, van der Giessen WJ, Duncker DJ, de Feyter PJ, van Geuns RJM. Accurate Automatic Papillary Muscle Identification for Quantitative Left Ventricular Mass Measurements in Cardiac Magnetic Resonance Imaging Acad Radiol 2008;15:1227-1233.

13. Janik M, Cham MD, Ross MI, Wang Y, Codella N, Min JK, Prince MR, Manoushagian S, Okin PM, Devereux RB, Weinsaft JW. Effects of papillary muscles and trabeculae on left ventricular quantification: increased impact of methodological variability in patients with left ventricular hypertrophy. J Hypertens. 2008;26:1677-1685.

14. Niwa K, Uchishiba M, Aotsuka H, Tobita K, Matsuo K, Fujiwara T, Tateno S, Hamada H. Measurement of ventricular volumes by cine magnetic resonance imaging in complex congenital heart disease with morphologically abnormal ventricles. Am Heart J 1996; 131:567-575.

15. Jauhiainen T, Järvinen VM, Hekali PE, Poutanen VP, Penttilä A, Kupari M. MR gradient echo volumetric analysis of the human cardiac casts: Focus on the right ventricle. J Comp Assist Tomogr 1998; 22:899-903.

16. Alfakih K, Thiele H, Plein S, Bainbridge GJ, Ridgeway JP, Sivananthan MU. Comparison of right ventricular volume measurement between segmented k-space gradient-echo and steady-state free precession magnetic resonance imaging. J Magn Res Imag 2002; 16:253-258.

Chapter

2

17. Semelka RC, Tomei E, Wagner S, Mayo J, Kondo C, Suzuki J, Caputo GR, Higgins CB. Normal left ventricular dimensions and function: Interstudy reproducibility of measurements with cine MR imaging. Radiology 1990; 174:763-768.
18. Miller S, Simonetti OP, Carr J, Kramer U, Finn JP. MR Imaging of the heart with cine true fast imaging with steady-state precession: influence of spatial and temporal resolutions on left ventricular functional parameters. Radiology. 2002;223:263-269.
19. Dulce MC, Mostbeck GH, Friese KK, Caputo GR, Higgins CB. Quantification of left ventricular volumes and function with cine MR imaging: comparison of geometrical models with three-dimensional data. Radiology 1993; 188:371-376.
20. Chuang ML, Hibberd MG, Salton CJ, Beaudin RA, Riley MF, Parker RA, Douglas PS, Manning WK. Importance of imaging method over imaging modality in noninvasive determination of left ventricular volumes and ejection fraction: assessment by two- and three-dimensional echocardiography and magnetic resonance imaging. J Am Coll Cardiol 2000; 35:477-484.
21. Sakuma H, Fujia N, Foo TKF, Caputo GR, Nelson SJ, Hartiala J, Shimakawa A, Higgins CB. Evaluation of left ventricular volume and mass with breath-hold cine MR imaging. Radiology 1993; 188:377-380.
22. Lamb HJ, Singleton RR, van der Geest RJ, Pohost GM, de Roos A. MR imaging of regional cardiac function: Low-pass filtering of wall thickness curves. Magnetic Resonance in Medicine 1995; 34:498-502.
23. Lorenz CH, Walker ES, Morgan VL, Graham TP, Klein SS. Normal human right and left ventricular mass, systolic function and gender differences by cine magnetic resonance imaging. J Cardiovasc Magn Reson 1999; 1:7-21.
24. Rominger MB, Bachmann GF, Pabst W, Rau WS. Right ventricular volumes and ejection fraction with fast cine MR imaging in breath-hold technique: Applicability, normal values from 52 volunteers, and evaluation of 325 adult cardiac patients. J Magn Reson Imag 1999; 10:908-918.
25. Alfakih K, Plein S, Thiele H, Jones T, Ridgway JP, Sivananthan MU. Normal human left and right ventricular dimensions for MRI as assessed by turbo gradient echo and Steady-State Free Precession imaging sequences. J Magn Res Imag 2003; 17:323-329.
26. Lee VS, Resnick D, Bundy JM, Simonetti OP, Lee P, Weinreb JC. Cardiac function: MR evaluation in one breath hold with real-time True Fisp imaging with steady-state precession. Radiology 2002; 222:835-842.
27. Wei LI, Stern JS, Mai VM, Pierchala LN, Edelman RR, Prasad PV. MR assessment of left ventricular function: Quantitative comparison of fast imaging employing steady-state acquisition (FIESTA) with fast gradient echo cine technique. J Magn Res Imag 2002; 16:559-564.
28. Maroules CD, McColl R, Khera A, Peshock RM. Interstudy reproducibility of SSFP cine magnetic resonance: impact of magnetic field strength and parallel imaging. J Magn Reson Imaging. 2008 May;27:1139-1145.
29. Azhari H, Sideman S, Weiss JL, Shapiro EP, Weisfeldt ML, Graves WL, Rogers W, Beyar R. Three-dimensional mapping of acute ischemic regions using MRI: wall thickening versus motion analysis. Am J Physiol 1990; 259 (Heart Circ. Physiol. 28):H1492-H1503.
30. van Rugge FP, van der Wall EE, Spanjersberg SJ, de Roos A, Matheijssen NAA, Zwinderman AH, van Dijkman PRM, Reiber JHC, Bruschke AVG. Magnetic resonance imaging during dobutamine stress for detection of coronary artery disease; quantitative wall motion analysis using a modification of the centerline method. Circulation 1994; 90:127-138.
31. Haag UJ, Maier SE, Jakob M, Liu K, Meier D, Jenni R, Boesiger P, Anliker M, Krayenbuehl HP. Left ventricular wall thickness measurements by magnetic resonance: a validation study. Int J Cardiac Imag 1991; 7:31-41.

32. Baer FM, Smolarz K,   PT, Voth E,   HS, Sechtem U. Regional 99mTc-methoxyisobutyl-isonitrile-uptake at rest in patients with myocardial infarcts: comparison with morphological and functional parameters obtained from gradient-echo magnetic resonance imaging. Eur Heart J 1994; 15:97-107.
33. Holman ER, Vliegen HW, van der Geest RJ, Reiber JHC, van Dijkman PRM, van der Laarse A, de Roos A, van der Wall EE. Quantitative analysis of regional left ventricular function after myocardial infarction in the pig assessed with cine magnetic resonance imaging. Magn Reson Med 1995; 34:161-169.
34. Sheehan FH, Bolson EL, Dodge HT, Mathey DG, Schofer J, Woo HK. Advantages and applications of the centerline method for characterizing regional ventricular function. Circulation 1986; 74:293-305.
35. von Land CD, Rao SR, Reiber JHC. Development of an improved centerline wall motion model. Comput Cardiol 1990;687-690.
36. Holman ER, Buller VGM, de Roos A, van der Geest RJ, Baur LHB, van der Laarse A, Bruschke AVG, Reiber JHC, van der Wall EE. Detection and quantification of dysfunctional myocardium by magnetic resonance imaging: A new three-dimensional method for quantitative wall-thickening analysis. Circulation 1997; 95:924-931.
37. Buller VGM, van der Geest RJ, Kool MD, van der Wall EE, de Roos A, Reiber JHC. Assessment of regional left ventricular wall parameters from short-axis MR imaging using a 3D extension to the improved centerline method. Invest Radiol 1997; 32:529-539.
38. Guttman MA, Prince JL, McVeigh ER. Tag and contour detection in tagged MR images of the left ventricle. IEEE TMI 1993; 13:74-88.
39. Moore CC, McVeigh ER, Zerhouni EA. Quantitative tagged magnetic resonance imaging of the normal human left ventricle. Topics in MRI 2000; 11:359-371.
40. Garot J, Bluemke DA, Osman NF, Rochitte ER, McVeigh ER, Zerhouni EA, Prince JL, Lima JA. Fast determination of regional myocardial strain fields from tagged cardiac images using harmonic phase MRI. Circulation 2000; 101:981-988.
41. Osman NF, McVeigh ER, Prince JL. Imaging heart motion using harmonic phase MRI. IEEE Trans Med Imag 2000; 19:186-202.
42. Jung B, Markl M, Föll D, Hennig J. Investigating myocardial motion by MRI using tissue phase mapping. Eur J Cardiothorac Surg. 2006;29 Suppl 1:S150-157.
43. Jung B, Föll D, Böttler P, Petersen S, Hennig J, Markl M. Detailed analysis of myocardial motion in volunteers and patients using high-temporal-resolution MR tissue phase mapping. J Magn Reson Imaging 2006 ;24:1033-1039.
44. Föll D, Jung B, Schilli E, Staehle F, Geibel A, Hennig J, Bode C, Markl M. Magnetic resonance tissue phase mapping of myocardial motion: new insight in age and gender. Circ Cardiovasc Imaging 2010;3:54-64.
45. Pelc NJ, Drangova M, Pelc LR, Zhu Y, Noll DC, Bowman BS, Herfkens RJ. Tracking of cyclic motion with phase-contrast cine MR velocity data. J Magn Reson Imag 1995; 5:339-345.
46. Hennig J, Schneider B, Peschl S, Markl M, Krause T, Laubenberger J. Analysis of myocardial motion based on velocity measurements with a black blood prepared segmented gradient-echo sequence: methodology and applications to normal volunteers and patients. J Magn Reson Imaging 1998; 8:868-877.
47. McInerney T, Terzopoulos D. A dynamic finite element surface model for segmentation and tracking in multidimensional medical images with application to cardiac 4D image analysis. Comput Med Imaging Graph 1995; 19:69-83.
48. Matsumura K, Nakase E, Haiyama T, Utsunomiya S. Automatic left ventricular volume measurements on contrast-enhanced utrafast cine magnetic resonance imaging. Eur J Radiol 1995; 20:126-132.
49. Goshtasby A, Turner DA. Segmentation of cardiac cine MR images for right and left ventricular chambers. IEEE Trans on Med Im 1995; 14:56-64.

50. Baldy C, Doueck P, Croisille P, Magnin IE, Revel D, Amiel M. Automated myocardial edge detection from breath-hold cine-MR images: evaluation of left ventricular volumes and mass. Magn Reson Imaging 1994; 12:589-598.
51. van der Geest RJ, Buller VGM, Jansen E, Lamb HJ, Baur LHB, van der Wall EE, de Roos A, Reiber JHC. Comparison between manual and automated analysis of left ventricular volume parameters from short axis MR images. J Comput Assist Tomogr 1997; 21:756-765.
52. Butler SP, McKay E, Paszkowski AL, Quinn R, Shnier RC, Donovan JT. Reproducibility study of left ventricular measurements with breath-hold cine MRI using a semiautomated volumetric image analysis program. J Magn Reson Imaging 1998; 8:467-472.
53. Kaushikkar SV, Li D, Haacke EM, Dávilla-Román VG. Addaptive bloodpool segmentation in three-dimensions: application to MR cardiac evaluation. J Magn Reson Imaging 1996; 6:690-697.
54. Singleton HR, Pohost GM. Automatic cardiac MR image segmentation using edge detection by tissue classification in pixel neighborhoods. Magn Reson Med 1997; 37:418-424.
55. Furber A, Balzer P, Cavaro-Menárd C, Croué A, Da Costa E, Lethimonnier F, Geslin P, Tadéi A, Jallet P, Le Jeune JJ. Experimental validation of an automated edge-detection method for a simultaneous determination of the endocardial and epicardial borders in short-axis cardiac MR images: application in normal volunteers. J Magn Reson Imaging 1998; 8:1006-1014.
56. Nachtomy E, RC, Vaturi M, Bosak E, Vered Z, Akselrod S. Automatic assessment of cardiac function from short-axis MRI: Procedure and clinical evaluation. Magn Reson Imag 1998; 16:365-376.
57. Lalande A, Legrand L, Walker PM, Guy F, Cottin Y, Roy S, Brunotte F. Automatic detection of left ventricular contours from cardiac cine magnetic resonance imaging using fuzzy logic. Invest Radiol 1999; 34:211-217.
58. Hautvast G, Lobregt S, Breeuwer M, Gerritsen F. Automatic Contour Propagation in Cine Cardiac Magnetic Resonance Images IEEE Trans Med Imag 2006;25:1472-1482.
59. Cocosco CA, Niessen WJ, Netsch T, et al. Automatic image-driven segmentation of the ventricles in cardiac cine MRI. J Magn Reson Imaging 2008; 28:366-374.
60. Codella NC, Weinsaft JW, Cham MD, Janik M, Prince MR, Wang Y. Left ventricle: automated segmentation by using myocardial effusion threshold reduction and intravoxel computation at MR imaging. Radiology 2008;248:1004-1012.
61. Lee HY, Codella N, Cham M, Prince M, Weinsaft J, Wang Y. Left ventricle segmentation using graph searching on intensity and gradient and a priori knowledge (lvGIGA) for short-axis cardiac magnetic resonance imaging. J Magn Reson Imaging. 2008;28:1393-1401.
62. Amini AA, Weymouth TE, Jain RC. Using dynamic programming for solving variational problems in vision. IEE Trans PAMI 1990; 12:855-867.
63. Angelié A, de Koning PJH, Danilouchkine M, van Assen HC, Koning G, van der Geest RJ, Reiber JHC. Optimizing the automated segmentation of the left ventricule in magnetic resonance images. Med Phys 2005; 32:1-7.
64. Pattynama PMT, Lamb HJ, van der Velde EA, van der Wall EE, de Roos A. Left ventricular measurements with cine and spin-echo MR imaging: a study of reproducibility with variance component analysis. Radiology 1993; 187:261-268.
65. Lamb HJ, Doornbos J, van der Velde EA, Kruit MC, Reiber JHC, de Roos A. Echo-panar MRI of the heart on a standard sytem: validation of measurement of left ventricular function and mass. J Comp Assist Tomogr 1996; 20:942-949.
66. Cootes TF, Beeston C, Edwards GJ, Taylor CJ. A unified framework for atlas matching using active appearance models. Proc Information Processing in Medical Imaging 1999, Lecture Notes in Computer Science 1999; 1613:322-333.

67. Mitchell SC, Lelieveldt BPF, van der Geest RJ, Bosch JG, Reiber JHC, Sonka M. Multistage hybrid active appearance model matching: Segmentation of left and right ventricles in cardiac MR images. IEEE Trans Med Imaging 2001; 20:415-423.

68. Mitchell SC, Lelieveldt BPF, van der Geest RJ, Bosch JG, Reiber JHC, Sonka M. Segmentation of cardiac MR images: An active appearance model approach. proc. SPIE Medical Imaging 2000 Image Processing 2000; 3979:224-234.

69. van der Geest RJ, Lelieveldt BPF, Angelié A, Danilouchkine M, Swingen C, Sonka M, Reiber JHC. Evaluation of a new method for automated detection of left ventricular boundaries in time series of magnetic resonance images using an Active Appearance Motion Model. J Cardiovasc Magn Reson 2004; 6:609-617.

70. van Assen HC, Danilouchkine MG, Frangi AF, Ordás S, Westenberg JJM, Reiber JHC, Lelieveldt BPF, SPASM: a 3D-ASM for Segmentation of Sparse and Arbitrarily Oriented Cardiac MRI Data, Med. Image Analysis 2006; 10:286-303.

71. Karwatowski SP, Brecker SJD, Yang GZ, Firmin DN, Sutton MStJ, Underwood SR. Mitral valve flow measured with cine MR velocity mapping in patients with ischemic heart disease: comparison with Doppler echocardiography. J Magn Res Imag 1995; 5:89-92.

72. Beerbaum P, Körperich P, Barth P, Esdorn H, Gieseke J, Meyer H. Noninvasive quantification of left-to-right shunt in pediatric patients. Phase-contrast cine magnetic resonance imaging compared with invasive oximetry. Circulation 103, 2476-2482. 2001.

73. Kondo C, Caputo GR, Semelka R, Foster E, Shimakawa A, Higgins CB. Right and left ventricular stroke volume measurements with velocity-encoded cine MR imaging: In vitro and in vivo validation. AJR 1991; 157:9-16.

74. de Roos A, Helbing WA, Niezen RA, Rebergen SA, van der Wall EE, Ottenkamp J. Magnetic resonance imaging in adult congenital heart disease. In: Higgins CB, Inwall JS, Pohost GM, editors. Current and future applications of magnetic resonance in cardiovascular disease. Armonk, NY: Futura Publishing Company, Inc, 1988: 163-172.

75. Powel AJ, Geva T. Blood flow measurement by magnetic resonance imaging in congenital heart disease. Pediatr Cardiol 2000; 21:47-58.

76. Rebergen SA, de Roos A. Congenital heart disease. Evaluation of anatomy and function by MRI. Herz. 2000;25:365-383.

77. Valente AM, Powell AJ. Clinical applications of cardiovascular magnetic resonance in congenital heart disease. Cardiol Clin. 2007;25:97-110.

78. van der Geest RJ, Niezen RA, van der Wall EE, de Roos A, Reiber JHC. Automated measurement of volume flow in the ascending aorta using MR velocity maps: evaluation of inter- and interobserver variability in healthy volunteers. J Comp Assist Tomogr 1998; 22:904-911.

79. Gerber BL, Raman SV, Nayak K, Epstein FH, Ferreira P, Axel L, Kraitchman DL. Myocardial first-pass perfusion cardiovascular magnetic resonance: history, theory, and current state of the art. J Cardiovasc Magn Reson. 2008;28;10:18.

80. Jerosch-Herold M, Swingen C, Seethamraju RT. Myocardial blood flow quantification with MRI by model-independent deconvolution. Med Phys 2002; 29:886-897.

81. Pack NA, DiBella EVR, Rust TC, Kadrmas DJ, McGann CJ, Butterfield R, Christian PE, Hoffman JM. Estimating myocardial perfusion from dynamic contrast-enhanced CMR with a model-independent deconvolution method. J Cardiovasc Magn Reson 2008;10:52.

82. Lee DC, Johnson NP. Quantification of absolute myocardial blood flow by magnetic resonance perfusion imaging. JACC Img 2009;2:761-770.

83. Al-Saadi N, Nagel E, Gross M, Bornstedt A, Schnackenburg B, Klein C, Klimek W, Oswald H, Fleck E. Noninvasive detection of myocardial ischemia from perfusion reserve based on cardiovascular Magnetic Resonance. Circulation 2000;101:1379-1383.

84. Nagel E, Klein C, Paetsch I, Hettwer S, Schnackenburg B, Wegscheider K, Fleck E. Magnetic resonance perfusion measurements for the noninvasive detection of coronary artery disease. Circulation 2003; 108:432-437.
85. Schwitter J, Wacker CM, van Rossum AC, Lombarid M, Al-Saadi N, Ahlstrom H, Dill T, Larsson HBW, Flamm SD, Marquard M, Johansson L. MR-IMPACT: comparison of perfusion-cardiac magnetic resonance with single-photon emission computed tomography for the detection of coronary artery disease in a multicentre, multivendor, randomized trial. Eur Heart J 2008; 29:480-489.
86. Bidaut LM, Vallee JP. Automated registration of dynamic MR images for the quantification of myocardial perfusion. J Magn Reson Imaging 2001;13:648-655.
87. Adluru G, DiBella EVR, Schabel MC., Model-Based Registration for Dynamic Cardiac Perfusion MRI. J Magn Reson Imag. 2006;24:1062–1070.
88. Adluru G, DiBella EV, Schabel MC. Model-based registration for dynamic cardiac perfusion MRI. J Magn Reson Imaging. 2006;24:1062-1070.
89. Milles J, van der Geest RJ, Jerosch-Herold M, Reiber JH, Lelieveldt BPF. Fully automated motion correction in first-pass myocardial perfusion MR image sequences. IEEE Trans Med Imaging. 2008;27:1611-1621.
90. Kim RJ, Fieno DS, Parrish TH, Harris K, Chen EL, Simonetti O, Bundy J, Finn JP, Klocke FJ, Judd RM. Relationship of MRI delayed contrast enhancement to irreversible injury, infarct age, and contractile function. Circulation 1999; 100:1992-2002.
91. Kim RJ, Wu E, Rafael A, Chen EL, Parker MA, Simonetti O, Klocke FJ, Bonow RO, Judd RM. The use of contrast-enhanced magnetic resonance imaging to identify reversible myocardial dysfunction. New J Med 2000; 343:1445-1453.
92. Oshinski JN, Yang ZQ, Jones JR, Mata JF, French BA. Imaging time after Gd-DTPA injection is critical in using delayed enhancement to determine infarct size accurately with magnetic resonance imaging. Circulation 2001; 104:2838-2842.
93. Bondarenko O, Beek AM, Hofman MB, Kühl HP, Twisk JW, van Dockum WG, Visser CA, van Rossum AC. Standardizing the definition of hyperenhancement in the quantitative assessment of infarct size and myocardial viability using delayed contrast-enhanced CMR. J Cardiovasc Magn Reson. 2005; 7(2):481-485.
94. Beek AM, Bondarenko O, Afsharzada F, van Rossum AC. Quantification of late gadolinium enhanced CMR in viability assessment in chronic ischemic heart disease: a comparison to functional outcome. J Cardiovasc Magn Reson 2009;11:6
95. Schuijf JD, Kaandorp TA, Lamb HJ, van der Geest RJ, Viergever EP, van der Wall EE, de Roos A, Bax JJ. Quantification of myocardial infarct size and transmurality by contrast-enhanced magnetic resonance imaging in men. Am J Cardiol 2005; 94:284-288.
96. Amado LC, Gerber BL, Gupta VK, Rettmann DW, Szarf G, hock R, sir Kraitchman DL, ma JA. Accurate and objective infarct sizing by contrast-enhanced magnetic resonance imaging in a canine myocardial infacrtion model. J Am Coll Cardiol 2004; 44:2383-2389.
97. Hsu LY, Natanzon A, Kellman P, Hirsch GA, Aletras AH, Arai AE. Quantitative Myocardial Infarction on Delayed Enhancement MRI. Part I: Animal Validation of an Automated Feature Analysis and Combined Thresholding Infarct Sizing Algorithm. J Cardiovasc Magn Reson 2006;23:298–308.
98. Hennemuth, Seeger A, Friman O, Miller S, Klumpp B, Oeltze S, Peitgen HO. A comprehensive approach to the analysis of contrast enhanced cardiac MR images. Trans Med Imag 2008;27:1592-1610

CHAPTER

3

Comparison between manual and automated analysis of left ventricular volume parameters from short axis MR images

ABSTRACT

Objective: Goal of this study was to evaluate a newly developed semi-automated contour detection algorithm for the quantitative analysis cardiovascular magnetic resonance imaging.

Methods: Left ventricular function parameters derived from automatically detected endocardial and epicardial contours were compared to results derived from manually traced contours in short-axis multi-slice gradient echo MR imaging studies of ten normal volunteers and ten infarct patients.

Results: Compared to manual image analysis the semi-automated method resulted in the following systematic and random differences (auto-manual; mean ±standard deviation): end-diastolic volume: -5.5 ± 9.7 ml; end-systolic volume: -3.6 ± 6.5 ml, ejection fraction: 1.7 ± 4.1%; left ventricular mass: 7.3 ± 20.6 g. Total analysis time for a complete study was reduced from 3-4 hours for the manual analysis to less than 20 minutes using semi-automated contour detection.

Conclusion: Global left ventricular function parameters can be obtained with a high degree of accuracy and precision using the present semi-automated contour detection algorithm.

Chapter

3

3.1 INTRODUCTION

Cardiac magnetic resonance (MR) imaging has proven to be an accurate and reproducible imaging modality for the quantitative evaluation of left ventricular function[1-8]. Gradient echo acquisitions in the short-axis orientation are particularly suitable for the assessment of left ventricular volumes and mass, as well as regional function parameters such as wall motion and wall thickening[9-11]. The assessment of these left ventricular size and function parameters, however, currently requires manual tracing of endocardial and epicardial contours in all the images to be analyzed. A typical cardiac MRI study contains 10 slices and 20 phases per cardiac cycle, i.e. 200 images in total. For most clinical applications of cardiac MRI, image analysis is limited to the end-diastolic and end-systolic time frames. However, the temporal resolution of a gradient echo MR acquisition allows the assessment of clinically valuable parameters describing the dynamics of left ventricular systolic ejection and diastolic filling, such as the peak ejection rate and filling rate[12-14]. To study these dynamic parameters, a frame-to-frame analysis needs to be carried out. While technological developments have resulted in decreased acquisition times and further improvements of image quality, the time consuming and tedious manual analysis procedure which is required to obtain the quantitative results, remains a limiting factor in the clinical use of cardiovascular MR imaging. The development of reliable automated contour detection software would be a major stimulus for the routine application of MR imaging in the evaluation of left ventricular function. To facilitate such quantitative left ventricular function analysis, we have developed the MR Analytical Software System (MASS)[15]. This software package provides manual tracing features as well as automated detection of left ventricular endocardial and epicardial contours in short-axis MR imaging studies. The use of the automated contour detection software facilitates the quantitative analysis of all phases of a multi-slice MR imaging study, thus providing assessment of left ventricular size in the end-diastolic and end-systolic phases as well as parameters describing the dynamics of left ventricular systolic ejection and diastolic filling.

The purpose of the current study was to evaluate the level of agreement between the semi-automated contour detection and manual image analysis for the assessment of global left ventricular volume parameters in gradient echo short-axis MR imaging studies using the MASS analytical software package.

3.2 METHODS

3.2.1 Study subjects

The study population consisted of 10 patients (8 men, 2 women) who had experienced myocardial infarction 3-50 weeks prior to the MR examination (average 27 weeks). The mean age of the patients was 49.6 years (range 29 - 65 years). In addition, 10 healthy volunteers (8 men, 2 women) with normal ECG and no history of cardiac malfunction were studied; mean age for this group was 30.5 years (range 21-39 years). The patient and normal studies were randomly selected from a larger database. For both sets of study subjects, the image quality was found to be acceptable for unambiguous identification of the endocardial and epicardial borders by visual inspection in the large majority (> 80%) of the images within a study.
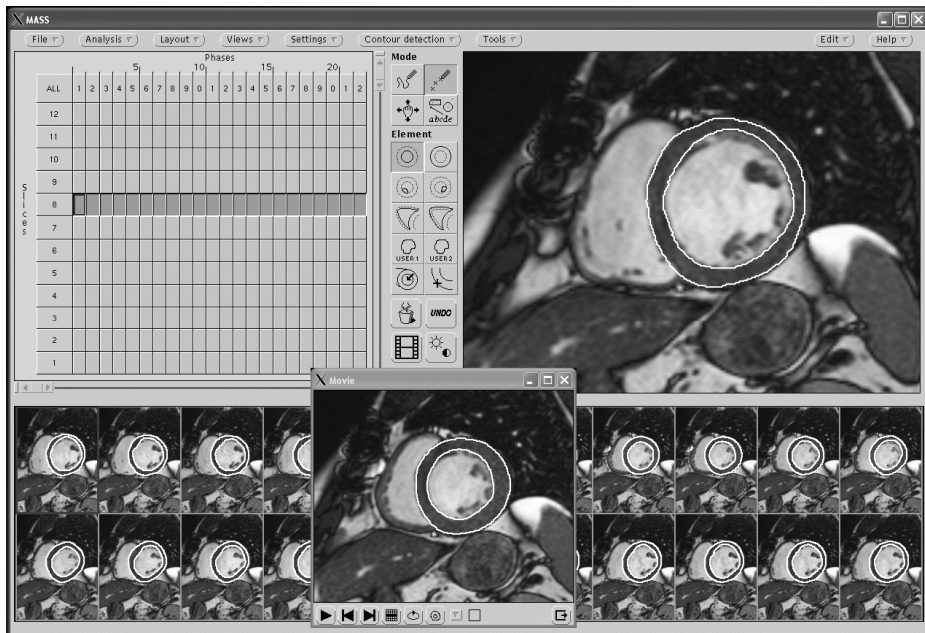
Figure 3-1. Screen layout of the MR Analytical Software System (MASS). In the upper left panel the colored bars represent all available images. The lower panel shows the time sequence of images to which the selected image belongs. The upper right panel shows the currently selected image in which contours can be edited. In a separate window a movie loop can be displayed for review of the images with the automatically detected contours.

Chapter

3

3.2.2 Image acquisition procedure

The infarct patients were examined on a 1.5 T MR scanner (Philips Gyroscan S15, Philips Medical Systems, Best, the Netherlands) using the body coil. Spin echo scout images were obtained in the coronal and sagittal imaging planes after which the short-axis plane was determined. The short-axis plane was defined perpendicular to the left ventricular long axis from the center of the mitral annulus to the apex. In the short-axis plane 10 contiguous slices of 10 mm were obtained using standard cine-MR imaging. The echo time was 13 ms, the flip angle 50°, the repetition time equal to the average R-R interval and the field of view was 400 mm^2. The temporal resolution was 54.63 ± 1.69 ms.

The MR examinations of the normal volunteers were performed on a 1.5 T MR scanner (Philips Gyroscan ACS). Multi-slice Spin echo localizing images oriented in transversal plane were obtained. From this scan a vertical long-axis and subsequently a horizontal long-axis plane were obtained using gradient echo MR imaging. The short axis was defined from both long-axis planes. In this plane 10 slices of 8 mm with a gap of 1-2 mm were obtained using standard cine-MR imaging. The echo time was 6 ms, the flip angle 50°, the repetition time equal to the average R-R interval and the field of view was 400 mm^2. The temporal resolution was 29.16 ± 1.75 ms.

3.2.3 Analysis software

Manual and semi-automated image analysis procedures were performed using the MR Analytical Software System (MASS version 2.0) developed at our laboratory (Figure 3.1). This software package incorporates a mouse controlled graphical user-interface and runs on a SUN Sparc workstation (Mountain View, California, USA). The automated contour detection algorithm follows a model-based approach which means that existing contours are used as guiding examples for the detection of contours in neighboring phases and slices[15]. The user-interface allows manual interaction with the contour detection procedure by editing or removing incorrectly detected contours. In each contour detection iteration endocardial and epicardial contours are detected in the selected images using the manually traced or automatically detected contours as models. Manual correction can be applied at any stage of the analysis. The contour detection procedure starts with the detection of epicardial contours in the first (end-diastolic) phase of a study, followed by a frame-to-frame contour detection procedure. In the following sections the developed algorithms are described in more detail.

3.2.4 Automated detection of epicardial contours in the end-diastolic phase

To identify the location and orientation of the left ventricle in the three-dimensional data set, the Hough Transform[16] for approximately circular objects was applied to the set of images belonging to the first cardiac phase. For each of the images, the Hough Transform resulted in an image with identical dimensions as the input image, with high values near center points of objects having a radius within the specified range (7.8-39 mm). The range of radii was determined such that both endocardial and epicardial edge points would contribute to the automated determination of the ventricular center. A straight line was fit through all available Hough images to estimate the long axis of the left ventricle. This procedure resulted in an estimation of the center of the left ventricle for each slice of the imaging study.

For the detection of epicardial contours, each image was transformed to polar coordinates using the available center point. A polar edge image was computed, highlighting locations of large intensity transitions in the polar image. For each radius the edge intensity in the polar edge image was summed. Using likelihood criteria for endocardial radius and myocardial wall thickness, two out of three radii with maximum edge intensity were selected, corresponding to an endocardial and epicardial circle estimation in the original image. Next, for each radial scan line the most likely epicardial radius was derived from the five edge intensity maxima for that scan line using criteria based on the distance of that point to the circular models. If no edge point satisfied the criteria, the epicardial radius for that scan line was derived afterwards by linear interpolation. The epicardial contour detected in the polar image was transformed to image coordinates.

3.2.5 Frame-to-frame detection of epicardial contours

For the detection of epicardial contours in other phases within the cardiac cycle a frame-to-frame contour detection algorithm was developed based on matching of line profiles combined with dynamic programming[17]. A similar strategy for echocardiographic images has been described before[18]. This matching approach was developed to follow each of the different gray value transitions existing between the myocardium and anatomical regions outside the myocardium. These regions have gray values which are brighter, darker or have a gray value equal to that of the left ventricular myocardium. The gray value transition to be expected at a specific position along the circumference of the myocardium can be derived from a temporal neighboring (model) image with a known epicardial contour. The algorithm is illustrated in Figure 3-2. Given a model image (A) with known epicardial

contour, a rectangular scan matrix (mask matrix) was generated by resampling the image at equidistant points along scan lines perpendicular to the local direction of the model contour. The model scan width was optimized to be large enough to include the typical shape of the gray value profile. The actual image (B) was resampled similarly using the same model contour, but with a larger scan width. The motion of an epicardial point, assumed to be perpendicular to the local contour direction, can be estimated by matching a one-dimensional scan line of the mask image at permissible locations along the corresponding scan line of the search matrix. Using this approach a third matrix was constructed by computing the match value of mask lines at every permissible location along the corresponding search line. For this purpose the correlation coefficient was used as match value and negated such that a good match resulted in a low value in the cost matrix. In this cost matrix an optimal (minimum cost) path was generated using dynamic programming techniques. The epicardial contour for image B resulted after transformation of this path to image coordinates.
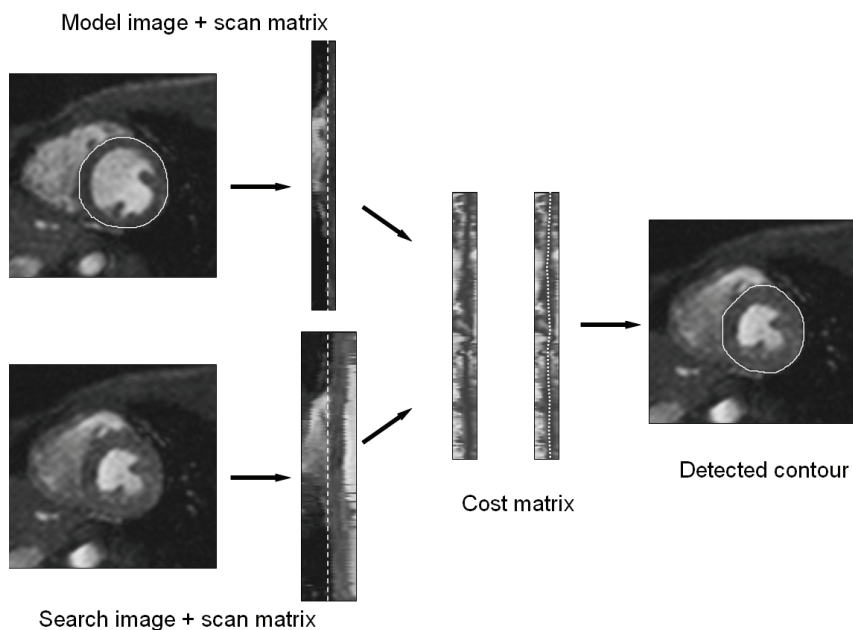
Figure 3-2. Diagram of the frame-to-frame epicardial contour detection. To detect the epicardial contour in the search image a known epicardial contour from a temporal neighboring image is used as a model. The model image is resampled perpendicularly to this epicardial contour resulting in a scan matrix. A similar scan matrix with a larger width is constructed from the search image. From both scan matrices a cost matrix is computed. The optimal path in this matrix results after transformation to the desired epicardial contour for the search image.

3.2.6 Detection of endocardial contours

The algorithm used for the detection of endocardial contours is illustrated in Figure 3-3. As a first step, an initial segmentation of the blood pool area was found using thresholding of the image within the region enclosed by the known epicardial contour. The optimal threshold was determined by generating radial scan lines emanating from the epicardial center and collecting for each scan line the gray value of the pixel with highest edge value within the epicardial contour. The mean gray value of these maximal edge pixels was designated as the optimal threshold. In a second step a smooth convex hull surrounding the blood pool area was determined resulting in an endocardial model contour. By following this approach, papillary muscles and regions caused by flow artifacts having relatively low intensity are enclosed by the contour. From this model contour a final contour was computed using minimal cost contour detection.

Chapter

3
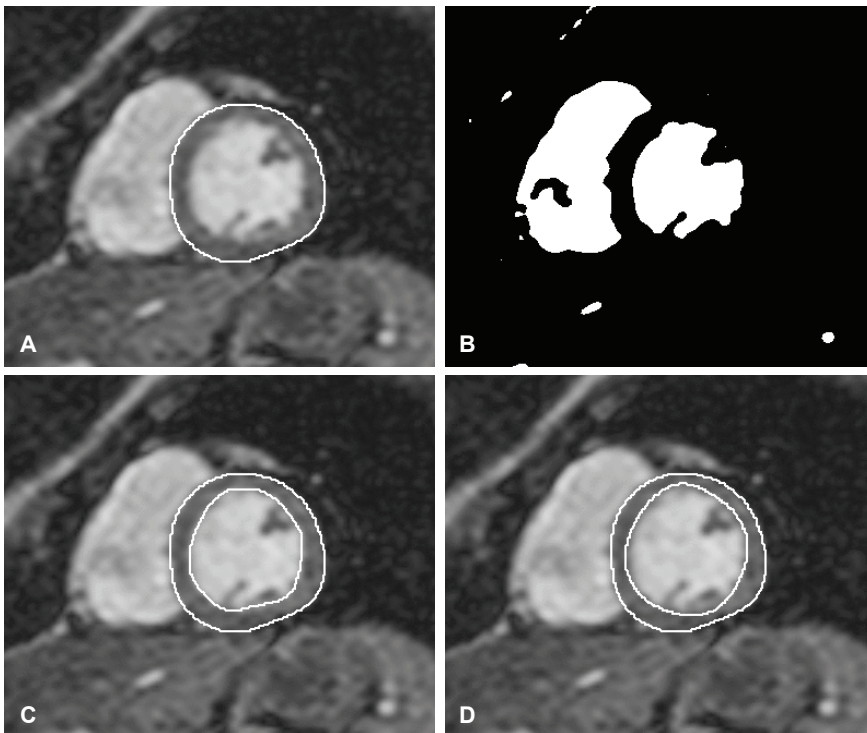
Figure 3-3. Diagram of the endocardial contour detection. The endocardial contour in an image (A) with known epicardial contour is detected by determining an optimal threshold resulting in an initial blood pool segmentation (B). A convexly shaped contour surrounding this contour is determined (C). This contour is used as a model for subsequent minimum cost contour detection resulting in the final endocardial contour (D).

3.2.7 Semi-automated analysis procedure

In this study, the following procedure was carried out. The user had to identify in which slices contours needed to be detected. In the first iteration the ventricular center was automatically detected and endocardial and epicardial contours were detected in all the selected images. After this first iteration the user was allowed to manually delete incorrect contours. In a second iteration the missing epicardial and endocardial contours were recomputed using the nearest temporal neighboring contour as the model. In case an endocardial contour was available, the region surrounding this contour was excluded from the search area of the corresponding epicardial contour. This resulted in more accurate epicardial contours in the second iteration. In case the contour detection was not entirely successful after this second iteration, the user was allowed to delete incorrect contours and manually correct at the most one single epicardial contour per slice. In the next iteration of the contour detection, the missing contours were automatically detected. In this last iteration the manually edited epicardial contour was used as the model for the detection of the missing epicardial contours in that slice. The number of manually edited epicardial contours was recorded. Manual correction to endocardial contours was not allowed at all. In the most basal slices where no complete circumference of left ventricular myocardium could be identified, the contours were traced manually.

3.2.8 Manual contour tracing

Endocardial and epicardial contours were also traced manually by an experienced observer in all the acquired phases for the slices encompassing the left ventricle. Window and level settings were standardized and kept unchanged for all studies. Papillary muscles and trabeculations were treated as being part of the blood pool[7]. In order to assess the relative overestimation of the volume of the ventricular blood pool, contours have also been traced at another occasion in the end-diastolic phase excluding the papillary muscles and trabeculations from the blood pool.

The upper slice showing at least 50% of the circumference of left ventricular myocardium was defined as the most basal slice to be included in the analysis. In this slice, the blood pool area enclosed by the myocardium and the aortic valve was included in the left ventricular volume calculations. To examine whether the contours describing the myocardial volume were traced consistently over the cardiac cycle within a single subject, the within-subject standard deviation of myocardial volume was determined for each study. A small value for this standard deviation would indicate a correct interpretation of the images over a complete cardiac

cycle. A second observer manually traced the endocardial and epicardial contours for only the end-diastolic and end-systolic phases to assess the inter-observer variabilities for this study.

3.2.9 Quantification of left ventricular mass and volume

Left ventricular volumes were measured in each phase by multiplying the contour areas by the sum of the slice thickness and slice gap. The end-diastolic volume (EDV) was obtained from the first phase after the R-wave (phase 1). End-systolic volume (ESV) was measured in the phase showing the smallest endocardial volume. Stroke volume (SV) was defined as the difference between EDV and ESV. Ejection fraction (EF) was calculated as SV divided by EDV. The left ventricular mass was determined in each phase by computing the volume of the left ventricular wall multiplied by the specific density of myocardium (1.05 g/cm^3). The peak ejection rate (PER) was defined as the maximum decrease in left ventricular volume per unit of time. The time to peak ejection rate (TPER) was defined as the time offset of the moment of PER to the R-wave. Similarly, peak filling rate (PFR) was defined as the maximum increase in left ventricular volume per unit of time. The time to peak filling rate (TPFR) was defined as the time offset of the moment of PFR from the moment of end-systole. Both PER and PFR were expressed in EDV/s.

Chapter

3

3.3 STATISTICAL ANALYSIS

Inter-observer variabilities expressed as mean difference ± standard deviation of paired differences were determined for left ventricular mass and volumetric function parameters. Single factor analysis of variance was used to determine the statistical significance of differences between normals and patients for each left ventricular function parameter. Linear regression analysis was used to quantify the correlation between results from semi-automated and manual image analysis. In addition, the level of agreement between manual and semi-automated image analysis was determined by computing the systematic and random differences in the calculated left ventricular volume parameters. A Student t-test was performed to determine the statistical significance of observed differences between the two measurement methods. A p-value of 0.05 was considered to indicate statistical significance.

3.4 RESULTS

3.4.1 Manual analysis

Endocardial and epicardial contours were traced manually in 2504 short-axis MR images. The total analysis time per study was 3 to 4 hours. Inter-observer variabilities for manual analysis were: EDV: 6.5 ± 16.7 ml, ESV: 4.4 ± 9.3 ml, SV: 2.0 ± 12.7 ml, EF: 0.2 ± 4.8% and left ventricular mass: 12.8 ± 23.5 g. The variation in myocardial volume over the different cardiac phases of a study resulted in a mean within-subject standard deviation of myocardial volume of 4.4%.

Table 3-1 lists the mean values and standard deviations of the quantified volumetric left ventricular function parameters for the two study groups separately. As expected the ventricular performance in the group of infarct patients was significantly reduced compared to the healthy volunteers. No difference was found in EDV (143.6 ml for patients versus 150.2 ml for normals; p=NS). ESV was significantly larger in patients (75.2 ml versus 46.3 ml; p<0.05) and consequently the SV (68.4 ml versus 96.4 ml; p<0.05) and EF (49.0% versus 69.1%; p<0.05) were smaller. The left ventricular mass was markedly higher in patients (177.4 versus 114.4 g; p<0.05). All of these measurements are based on endocardial contours which include papillary muscles and trabeculations. By manual analysis, it was found that these structures represent 6.5 ± 1.3% of the EDV. An estimation of the true EF can be made by adding this value to the measured EF.

Table 3-1. Mean values and standard deviations of ventricular dimensions and volumetric functional parameters assessed in normals and patients using manual tracing of endocardial and epicardial contours.

	Normals (n=10)		Patients (n=10)	
	Mean	SD	Mean	SD
EDV (ml)	150.2	20.3	143.6	32.0
ESV (ml)	46.3	8.4	75.2*	28.2
SV (ml)	103.9	15.6	68.4*	11.7
EF (%)	69.1	4.4	49.0*	9.2
Mass (g)	114.4	21.6	177.4*	26.1
PER (EDV/s)	4.07	0.64	2.41*	0.61
TPER (ms)	118	41	96	38
PFR (EDV/s)	4.32	0.97	2.09*	0.55
TPFR (ms)	138	22	181*	55

*: indicates statistical significant difference of values for patients compared to normals (p<0.05).

The parameters describing the dynamics of left ventricular ejection and filling showed a reduced PER and PFR in patients (2.41 and 2.09 EDV/s versus 4.07 and 4.32 EDV/s respectively; p<0.05). The timings of these events were not significantly different for TPER (96 ms versus 118 ms; p=NS) but TPFR was significantly prolonged for patients (181 ms versus 138 ms; p<0.05).

3.4.2 Semi-automated analysis

The semi-automated contour detection software was used to detect endocardial and epicardial contours in 2504 short-axis MR images. In the most basal slices, representing 12% of the images, the contours were traced manually. For the remaining 88% of the images the contours were detected automatically. The automated analysis time per image was in the order of 1 s per image or two minutes per study. In addition, manual correction of *epicardial* contours was necessary in 1.4% of the total number of epicardial contours (average: 2 epicardial contours per study). In 5 out of the 20 studies, the automatically detected contours did not require any manual editing. Manual editing of the automatically detected endocardial contours was not allowed in this study. The total analysis time per study for the semi-automated procedure, including careful review of the results and manual corrections, was less than 20 minutes.

Table 3-2. Systematic and random differences (auto - manual) in the assessment of left ventricular dimensions and function parameters using either semi-automated or manual image analysis.

	Normals (n=10)		Patients (n=10)		Overall (n = 20)		
	Mean	SD	Mean	SD	Mean	SD	r
EDV (ml)	-13.4*	5.7	2.4	5.7	-5.5	9.7	0.94
ESV (ml)	-5.9*	4.9	-1.4	7.1	-3.6*	6.5	0.97
SV (ml)	-7.5*	4.4	3.8	7.6	-1.9*	8.4	0.94
EF (%)	1.4	3.0	2.1	4.9	1.7*	4.1	0.95
Mass (g)	22.8*	10.2	-8.2	16.2	7.3*	20.6	0.87

EDV=end-diastolic volume; ESV=end-systolic volume; SV=stroke volume; EF=ejection fraction.

*: indicates statistical significant difference of values for patients compared to normals (p<0.05).

3.4.3 Comparison of left ventricular volume parameters and mass derived from manually and automatically detected contours

The agreement between semi-automated and manual analysis for the assessment of volumetric parameters is presented in Table 3-2 and further illustrated in Figure 3-4 using Bland and Altman graphs[19]. From Table 3-2 it is apparent that in the group of normal individuals the semi-automated contour detection produced slightly smaller endocardial contours which resulted in an underestimation of EDV (-13.4 ± 5.7 ml; p<0.05), ESV (-5.9 ± 4.9 ml; p<0.05) and SV (-7.5 ± 4.4 ml; p<0.05). This underestimation was not present in the group of patients: all differences were small and statistically not significant. An excellent agreement in EF measurement was found in both study groups; in normals a difference of 1.4 ± 3.0% (p=NS) and in patients a mean difference of 2.1 ± 4.9% (p=NS) was found. A statistically significant overestimation in myocardial mass was found in the group of healthy volunteers (22.8 ± 10.2 g; p<0.05). This difference is partly the result of the smaller automatically detected endocardial contours in this group. In patients the semi-automated contour detection resulted in smaller myocardial mass measurements, but this difference was found to be statistically not significant (-8.2 ± 16.2 g; p=NS).

Table 3-3. Systematic and random differences (auto - manual) of the semi-automated contour detection algorithm as compared to manually obtained results.

	Normals (n=10)		Patients (n=10)		Overall (n=20)			
	Mean	SD	Mean	SD	Mean	SD	r	r
PER (EDV/s)	0.57*	0.49	0.35*	0.29	0.46*	0.42	0.93	
TPER (ms)	6.4	25.6	10.6	33.5	8.5	29.9	0.70	
PFR (EDV/s)	-0.27	0.75	0.17	0.45	-0.05	0.66	0.86	
TPFR (ms)	-3.7	43.7	27.4	61.8	11.9	55.7	0.63	

*: indicates statistical significant difference (p<0.05).

3.4.4 Comparison of manually and automatically obtained left ventricular systolic ejection and diastolic filling parameters

The systematic and random differences for the measurements using semi-automated and manual image analysis are reported in Table 3-3. The semi-automated contour detection resulted in larger values for PER

(0.57 ± 0.49 EDV/s for normals and 0.35 ± 0.29 EDV/s for patients; p<0.05). No statistically significant differences were found in the determination of PFR (-0.27 ± 0.75 EDV/s for normals and 0.17 ± 0.45 EDV/s for patients). Manually and automatically determined values for TPER and TPFR were in excellent agreement in both study groups: the mean differences for TPER and TPFR ranged from -3.7 to + 27.4 ms (p=NS). The standard deviations of the differences ranged from 25.6 to 61.8 ms and were in the same order of magnitude as the temporal resolution

Chapter

3
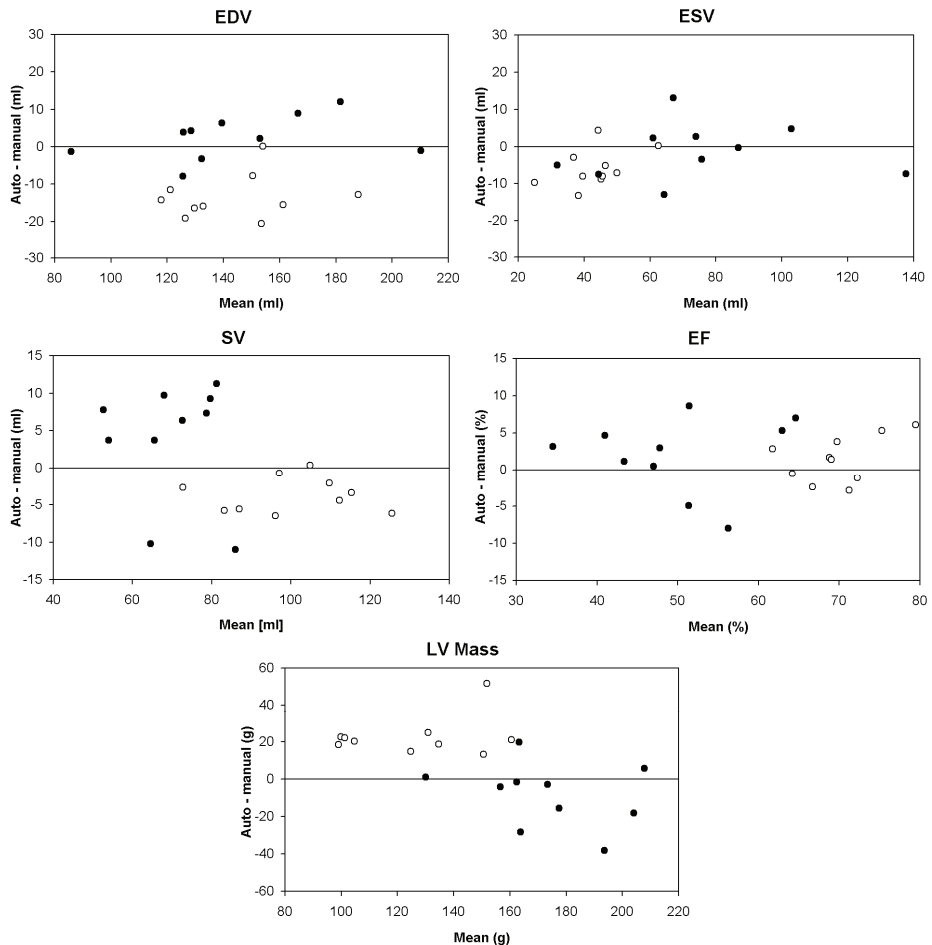
Figure 3-4. Agreement between left ventricular function parameters derived from manually traced and automatically detected contours depicted in Bland and Altman graphs. The mean value of the measurement values for automated and manual analysis is plotted along the horizontal axis; the difference between these two measurement methods is plotted along the vertical axis. Mean values of the differences and standard deviations are listed in Table 3-2. Patients are identified with a closed dot (•); volunteers are indicated by open circles (o).

3.5 DISCUSSION

Several validation studies have been performed demonstrating the accuracy and precision of left ventricular volume measurements from MR imaging acquisitions in different orientations [10-11]. The clinical value of cardiovascular MR imaging would significantly improve if the time consuming and tedious process of manual contour tracing and subsequent quantitative analysis could be automated and integrated in a dedicated software package. Towards these goals, contour detection software was developed and integrated in an analytical software package as a tool for the off-line analysis of multi-slice short-axis left ventricular MR images. As an important step towards the clinical acceptance of automated contour detection software, extensive validation is required on imaging data from normals and patients acquired on different scanners and through various imaging protocols. In the current validation study the software was utilized on MR imaging studies of normal volunteers and infarct patients acquired on two different 1.5 T MR scanners using a gradient echo pulse sequence.

3.5.1 Guidelines for tracing of endocardial contours

In the manual analysis procedure and the automated contour detection algorithm, endocardial contours were defined to describe the inner boundary of the myocardial wall[20]. With this approach the papillary muscles, either floating in the blood pool area or being connected to the myocardial wall, are considered to be no part of the myocardial muscle. This approach has two distinct advantages. First, papillary muscles and flow voids both result in dark areas within the blood pool and therefore are difficult to differentiate for an automated algorithm or a human operator. A second advantage is that the actual size of the papillary muscle is easily overestimated due to motion artifacts and partial volume effects. To be able to detect the inner wall of the myocardium according to our definition, the contours are restricted to be more or less convexly shaped. If the papillary muscles are attached to the myocardial wall or if trabeculations exist, the contour detection produces contours which cut through the attachments. A consequence of this approach is that the left ventricular blood volumes are slightly overestimated, resulting in an accurate assessment of stroke volumes, but slightly lower ejection fractions measurements. It is assumed that this disadvantage is balanced by the reduction in observer variabilities. By manual analysis it was found that the volume of the papillary muscles represents 6.5 ± 1.3% (mean ± SD) of the EDV. Consequently the true EF is 6.5% higher than the EF assessed from the endocardial contours according to our definition.

3.5.2 Guidelines for analyzing basal slices

It has been advocated that the multi-slice short-axis acquisition is ideal for left ventricular volume measurements since no geometrical assumptions are required for the analysis[21]. One of the drawbacks of this type of acquisition is that due to the relative large slice thickness that is commonly used, the most basal slices are inadequately visualized. As a result, the partial volume effect which occurs in these slices makes a correct delineation of the left ventricular myocardium often not possible unambiguously. Different observers may incorporate different guidelines to define the region belonging to the left ventricular blood pool volume and the region to be included as being left ventricular myocardium. Another factor which complicates the analysis of these basal slices in a short-axis acquisition is the fact that it is well known that the left ventricle performs not only motion in the in-plane direction, but is also characterized by a through-plane motion which is in the order of 13 mm for the normal heart[22]. This through-plane motion which extends over more than one slice makes that the shape and size of the left ventricular contours may change abruptly in the upper slices from phase to phase. Given these complications, it was decided to manually trace the contours in the endocardial and epicardial contours in the most basal slice. The circumference of the left ventricular myocardium had to extend over at least 50 percent of the circumference to be included. By comparing the variation in myocardial volume over the cardiac phases it was examined whether the contours were traced consistently. In our study the within-subject standard deviation of left ventricular myocardial volume was 4.4%, which confirms that both endocardial and epicardial contours were accurately traced in this study.

3.5.3 Automated contour detection results

The results listed in Table 3-2 should be compared to the inter-observer variabilities which were assessed in this study. The mean differences reflect a systematic over- or underestimation of one measurement technique compared to the other. Since no true gold standard is available it remains unclear which of the two techniques is more accurate. The automated contour detection algorithm resulted in smaller endocardial contours and larger epicardial contours in the group of healthy volunteers, resulting in relatively large systematic differences. Since these differences were much smaller in the studies of the infarct patients, this may have been the result of the differences in image characteristics between the two acquisitions protocols. Although two different MRI scanners were used for the patients and the normal volunteers, the main reason for the differences in image

characteristics, probably is the fact that in patient studies problems related to ECG registration and motion result in more blurring of the images. In general, systematic differences of an automated contour detection algorithm are relatively easy to solve by adjusting specific parameters in the algorithm. The standard deviations in the inter-observer analyses are relatively high when compared to the standard deviations listed in the last column of Table 3-2. This leads to the assumption that the semi-automated analysis is less hampered by random variabilities, which is especially important in follow-up studies.

No reports are known on the assessment of inter-observer variabilities for the quantification of dynamic parameters derived from multi-slice multi-phase short-axis MR studies. Table 3-3 demonstrates that the timings of the peak ejection rate and peak filling rate were determined with high accuracy and precision by the automated contour detection software. The mean differences were close to zero, while the random errors were in the same order of magnitude as the temporal resolution. The values of the dynamic parameters are in correspondence to those reported in literature[12-14].

3.5.4 Analysis time

In our experience, the manual tracing of endocardial and epicardial contours in all the phases of a multi-slice multi-phase MR study with high temporal resolution takes approximately 3 to 4 hours depending on the heart size and image quality. Using the present cardiac MR analysis software, the analysis time was reduced to less than 20 minutes on average. The actual time required for the automated contour detection for 200 images is less than 3 minutes. Manual correction to contours was performed for only two epicardial contours per study on average. The time required for reviewing the automatically detected contours and deciding whether unsatisfactory contours should be redetected in a next iteration, contributes to most of the actual analysis time. In addition, the manual tracing of contours in the most basal slice, which is still required, takes a considerable amount of time.

3.5.5 Advantages of the present contour detection algorithm

Several other studies have reported on the development and clinical evaluation of software algorithms for the semi-automated detection of left ventricular endo and/or epicardial contours in MR image data[23-25]. All these algorithms require some sort of user interaction such as manually indicating a region of interest or indication of a left ventricular center point. Although the actual computation time can be quite low in such an

approach, the required user-interactions will result in a much longer total analysis time. In our approach the required user-interaction is very much limited leading to time efficient analysis procedures. Another advantage of the present contour detection algorithm is that the epicardial contour detection is designed to be adaptive to the image characteristics and is therefore relatively insensitive to changing scan parameter settings.

3.5.6 Limitations

In this study the automated results were compared to those of one single observer. The MR examinations were performed on two different scanners using slightly different imaging protocols. Systematic differences which were found in this study may have been introduced by observer bias or by differences in the MR examination protocols. In order to further investigate the value of the present contour detection software, additional future validation studies should be performed. Repeat measurements by the same observer on separate occasions or by different observers will reveal whether the use of automated contour detection will indeed lead to a reduction in the inter- and intraobserver variabilities as compared to the manual tracing procedures. Comparison of automated contour detection results with other imaging modalities, such as stroke volume measurement by MR flow velocity mapping, may be useful to test whether systematic errors exist in the automated contour detection requiring further optimization of certain parameters in the algorithm.

3.6 CONCLUSION

A new analytical software package (MASS) with semi-automated contour detection has been validated on cardiovascular MR image data from patients and healthy volunteers. Quantitative left ventricular function parameters derived from the automatically detected contours were compared with results derived from manual contour tracings. This study demonstrates that volumetric left ventricular function parameters and myocardial mass can be assessed accurately in a multi-slice short-axis acquisition protocol in a time-efficient manner using the present contour detection software.

3.7 ACKNOWLEDGMENT

3.8 REFERENCES

1. Florentine MS, Grosskreutz CJ, Chang W, Hartnett JA, Dunn VD, Ehrhardt JC, Fleagle SR, Collins SM, Marcus ML, Skorton DJ. Measurement of left ventricular mass in vivo using gated nuclear magnetic resonance imaging. J Am Coll Cardiol 1986; 8:107-112.
2. Sechtem U, Pflugfelder PW, Gould RG, Cassidy MM, Higgins CB. Measurement of right and left ventricular volumes in healthy individuals with cine MR imaging. Radiology 1987; 163:697-702.
3. Higgins CB, Holt W, Pflugfelder P, Sechtem U: Functional evaluation of the heart with magnetic resonance imaging. Magn Reson Med 1988; 6:121-139.
4. Buser PT, Auffermann WW, Holt WW, Wagner S, Kircher B, Wolfe C, Higgins CB. Noninvasive evaluation of global left ventricular function with use of cine nuclear magnetic resonance. J Am Coll Cardiol 1989; 11:1294-1300.
5. Semelka RC, Tomei E, Wagner S, Mayo J, Kondo C, Suzuki J, Caputo GR, Higgins CB. Normal left ventricular dimensions and function: Interstudy reproducibility of measurements with cine MR imaging. Radiology 1990; 174:763-768.
6. Semelka RC, Tomei E, Wagner S, Mayo J, Caputo G, O'Sullivan M, Parmley WW, Chatterjee K, Wolfe C, Higgins CB.. Interstudy reproducibility of dimensional and functional measurements between cine magnetic resonance studies in the morphologically abnormal LV. Am Heart J 1990;119: 1367-1373.
7. Pattynama PMT, Lamb HJ, van der Velde EA, van der Wall EE, de Roos A. Left ventricular measurements with cine and spin-echo MR imaging: a study of reproducibility with variance component analysis. Radiology 1993; 187:261-268.
8. Boxt LM, Katz J, Kolb T, Czegledy FP, Barst RJ: Direct quantitation of right and left ventricular volumes with magnetic resonance imaging in patients with primary pulmonary hypertension. J Am Coll Cardiol 1992; 19:1508-15.
9. Lotan CS, Cranney GB, Bouchard A, Bitner V, Pohost GM. The value of cine nuclear magnetic resonance imaging for assessing regional ventricular function. J Am Coll Cardiol 1983; 52:960-964.
10. van Rugge FP, van der Wall EE, Spanjersberg SJ, de Roos A, Matheijssen NAA, Zwinderman AH, van Dijkman PRM, Reiber JHC, Bruschke AVG. Magnetic resonance imaging during dobutamine stress for detection of coronary artery disease; quantitative wall motion analysis using a modification of the centerline method. Circulation 1994; 90:127-138.
11. Holman ER, Vliegen HW, van der Geest RJ, Reiber JHC, van Dijkman PRM, van der Laarse A, de Roos A, van der Wall EE. Quantitative analysis of regional left ventricular function after myocardial infarction in the pig assessed with cine magnetic resonance imaging. Magn Reson Med 1995; 34:161-169.
12. Bonow RO, Bacharach SL, Green MV, Kent KM, Rosing DR, Lipson LC, Leon MB, Epstein SE. Impaired left ventricular diastolic filling in patients with coronary artery disease: Assessment with radionuclide angiography. Circulation 1981; 2:315-323.
13. Mancini GBJ, Slutsky RA, Norris SL, Bhargava V, Ashburn WL, Higgins CB. Radionuclide analysis of peak filling rate, filling fraction and time to peak filling rate: Response to supine bicycle exercise in normal subjects and patients with coronary artery disease. Am J Cardiol 1983; 51:43-51.
14. Miller TR, Goldman KJ, Sampathkumaran KS, D.R B, Ludbrook PA, Sobel BE. Analysis of cardiac diastolic function: Application in coronary artery disease. J Nucl Med 1983; 24:2-7.
15. van der Geest RJ, Jansen E, Buller VGM, Reiber JHC. Automated detection of left ventricular epi- and endocardial contours in short-axis MR images. Comput Cardiol 1994:33-36.

16. Illingworth J, J K. A survey of the Hough transform. Computer Vision Graphics and Image Processing 1988; 44:87-116.
17. Dijkstra EW. A note on two problems in connection with graphs. Numerische Mathematik 1959; 1:269-272.
18. Bosch JG, van Burken G, Reiber JHC. Automatic frame-to-frame contour detection in echocardiograms using motion estimation. Comput Cardiol 1992: 351-354.
19. Bland JM, Altman DG. Statistical methods for assessing agreement between two methods of clinical measurement. Lancet 1986; 8:307-310.
20. Matheijssen NAA, Baur LHB, Reiber JHC, van der Velde EA, van Dijkman PRM, van der Geest RJ, de Roos A. Assessment of left ventricular volume and mass by cine-magnetic resonance imaging in patients with anterior myocardial infarction intra-observer and inter-observer variability on contour detection. Int J Cardiac Imag 1996; 12:11-19.
21. Dinsmore RE, Wismer GL, Miller SW, Thomson R, Johnston DL, Liu P, Okada RD, Saini S, Brady TJ. Magnetic resonance Imaging of the heart using imaging planes oriented to cardiac axes: experience with 100 cases. AJR 1985; 145:1177-1183.
22. Rogers WJ, Shapiro EP, Weiss JL, Buchalter MB, Rademakers FE, Weisfeldt ML, Zerhouni EA. Quantification and correction for left ventricular systolic long-axis shortening by magnetic resonance tissue tagging and slice isolation. Circulation 1991; 84:721-731.
23. Fleagle SR, Thedens DR, Stanford W, Pettigrew RI, Reichek N, Skorton DJ. Multicenter trial of automated border detection in cardiac MR imaging. J Magn Res Imag 1993; 3:409-415.
24. Fleagle SR, Thedens DR, Stanford DR, Thompson BH, Weston JM, Patel PP, Skorton DJ. Automated myocardial edge detection on MR images: accuracy in consecutive subjects. J Magn Res Imag 1993; 3:738-741.
25. Suh DY, Eisner RL, Mersereau RM, Pettigrew RI. Knowledge-based system for boundary detection of four-dimensional cardiac MR image sequences. IEEE Trans Med Imaging 1993; 12:65-72.

Chapter

3

CHAPTER

4

Automated assessment of MR velocity maps of the ascending aorta: Evaluation of inter- and intraobserver variability in the determination of left ventricular stroke volume by automated and manual analysis methods

ABSTRACT

Objective: An automated contour detection algorithm was developed for the objective and reproducible quantitative analysis of velocity encoded MR imaging studies of the ascending aorta.

Methods: The only user-interaction required is the manual definition of a center point inside the cross-section of the aorta in one of the available images. The automated contour detection algorithm detects an initial model contour in this image and subsequently corrects for motion and deformation of the aortic cross-section in each of the acquired images over the complete cardiac cycle using dynamic programming techniques. Integrating the flow velocity values for each pixel within the detected contour results in an instantaneous flow value. Next, by integrating the instantaneous flow values for each acquired phase over the complete cardiac cycle, left ventricular (LV) stroke volume (SV) measurement could be obtained. The results of the automated method were compared to results derived from manually traced contours in MR imaging studies from 11 healthy volunteers.

Results: An excellent agreement in SV measurements was observed: signed difference $0.61 \pm 1.51\%$. Inter- and intraobserver variabilities were less than 2% for both manual and automated image analysis methods. Manual tracing of contours required in the order of ten minutes; the analysis time for automated contour detection was less than 6 seconds per study.

Conclusion: The present contour detection allows fast and reliable LV stroke volume measurements from velocity encoded MR imaging studies.

Chapter

4

4.1 INTRODUCTION

Cine phase-contrast magnetic resonance (MR) flow velocity mapping has a proven clinical value in the evaluation of flow in the greater arteries[1-5]. This non-invasive imaging technique allows blood velocity measurements in vessel cross-sections at different points in the cardiac cycle at high temporal and spatial resolution. Application of this technique to the proximal portion of the ascending aorta allows the assessment of left ventricular (LV) systolic function. In the absence of mitral valve insufficiency, the LV stroke volume can be measured by integrating the instantaneous flow values over a complete cardiac cycle[4,6]. In addition, the presence and severity of aortic regurgitation may be quantified by comparing the antegrade and retrograde flow within a cardiac cycle[7,8].

For an accurate assessment of volume flow, contours describing the lumen of the vessel have to be traced in the images. Since the ascending aorta exhibits a significant in-plane and through-plane motion as well as changes in cross-sectional shape over the cardiac cycle, the user is required to trace the vessel border in each individual image of the multi-phase MR examination, thereby carefully avoiding the inclusion of flow in adjacent regions from other vessels. Since this is a time consuming and tedious procedure which introduces observer variabilities, the automation of this process would clearly enhance the clinical applicability of MR flow velocity mapping.

In this study an automated analysis algorithm is presented to be used for the automated detection of vessel boundaries in temporal series of MR flow velocity images of the ascending aorta. The required user-interaction is limited to the manual definition of an approximate center in one of the available images. The algorithm performs an automated detection of the vessel contours and corrects for motion and shape changes of the vessel cross section over the cardiac cycle. The contour detection algorithm was compared to manual tracings of the aortic contours by evaluating the derived stroke volume measurements in MR imaging studies of eleven healthy volunteers. Inter- and intraobserver analysis was performed for both manual and automated image analysis.

4.2 METHODS

4.2.1 Study subjects

The study population consisted of 11 healthy volunteers (4 men) with no history of cardiac disease. Mean age for this group was 37 years (range 25-63). All volunteers were in sinus rhythm during image acquisition and the mean heart rate was 66.6 ± 8.8 beats per minute.

4.2.2 MR examination procedure

MR examinations were performed on a 0.5 T MR scanner (Philips Medical Systems, Best, the Netherlands) using the body coil. Multi-slice spin-echo images orientated in the coronal plane were obtained to identify the orientation and course of the aortic arch. At a position 2-5 cm above the aortic valve, where the aorta was nearly parallel to the caudal cranial axis of the patient, a velocity map was acquired in the axial orientation using velocity encoded cine MR imaging. Imaging parameters for this MR scan were: echo time 8.7 ms, flip angle 45º, repetition time 25 ms, slice thickness 5 mm, field of view 200 x 140 mm, scan matrix 103 x 128, number of averages two, and the velocity sensitivity was set to 150 cm/s. Retrospective gating was applied to acquire images evenly spaced over a complete cardiac cycle resulting in twenty cardiac phases. The acquisition time was 2-3 minutes for the initial spin-echo scan and 2-3 minutes for the velocity-encoded scan depending on the heart rate of the study subject.

Chapter

4

4.2.3 Contour detection software

During a velocity encoded MR imaging study, phase difference and standard gradient echo images are acquired at multiple points in the cardiac cycle. Since the gradient echo images show good contrast even in the absence of flow, the automated contour detection algorithm was developed to operate on these images (see Figure 4-1). The actual flow velocity calculations are based on the pixel data in the corresponding phase difference images.

Over a cardiac cycle the position and shape of a vessel cross section may change due to motion of the heart and pressure changes in the artery. In general, for the ascending aorta, the change in shape is relatively little compared to the in-plane motion of the cross-section. The present contour detection algorithm deals with these two types of motion in two separate processing steps. The motion component describes the in-plane motion of the vessel's cross section; the deformation component describes the change in shape or size of the vessel's cross section. To obtain a more general applicability of the detection software, the user may adjust the parameters describing the maximum motion and deformation to be

expected for a certain type of application. In the experiments described in this study the parameters which determine the maximum allowed motion and deformation were kept fixed.

The analysis procedure starts with the detection of a model contour in one of the available images. To this end the user has to indicate an approximate center point of the vessel. This is the only manual interaction required in the total analysis procedure. To detect the contours in the other images within the temporal series, first a correction for vessel motion is performed, followed by a correction for changes in contour shape. The three steps of the automated contour detection algorithm are explained in more detail in the following sections.
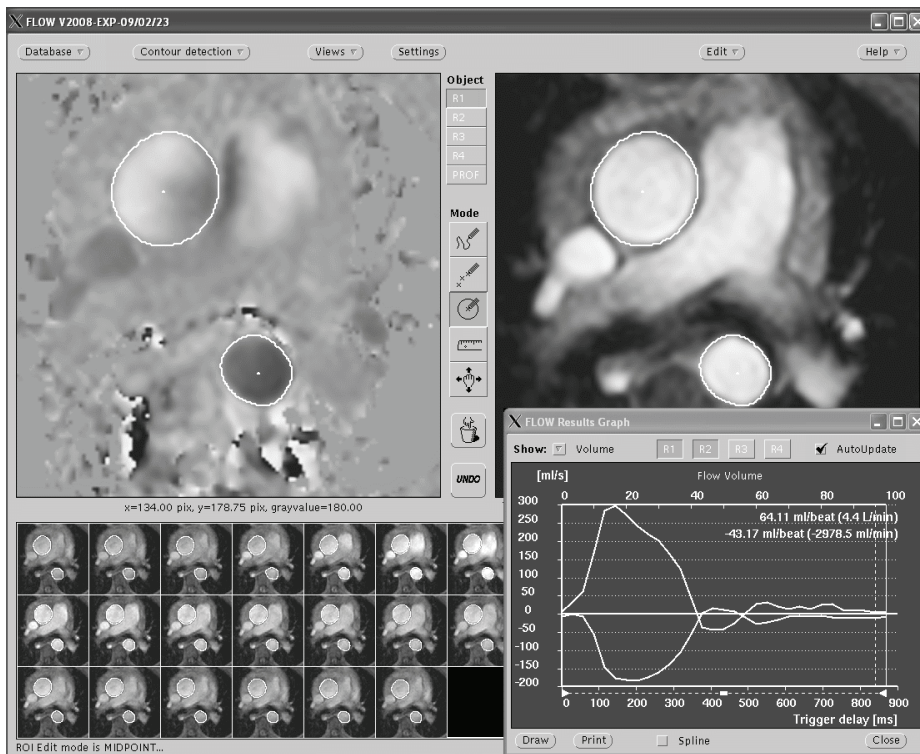
Figure 4-1. Screen lay-out of the software package FLOW. The upper panels display the phase and modulus images of one of the available cardiac phases. A volume graph is shown for the ascending and descending aorta derived from the automatically detected contours.

4.2.4 Detection of a model contour

To detect the vessel contours in a series of images, an initial model contour providing a rough approximation of the vessel boundary needs to be

detected in one of the available images. For this purpose the user has to select the phase in the cardiac cycle where the ascending aorta is shown with maximum contrast in the modulus images. In this image, the approximate center has to be indicated by the user. Following this step, radial scan lines are constructed at evenly spaced angular intervals starting at the center point. For each scan line the pixel with maximum edge strength is recorded. The search for edge pixels is limited to a distance of less than 20 mm from the indicated center point, representing a sufficiently large margin for most of the clinical cases. The size of this search distance can be adjusted manually in case the aorta appears to be enlarged. The mean gray value of these pixels is used as a threshold to obtain a rough estimation of the vessel's cross section. The contour surrounding this segmented area is used as a model contour for the vessel boundary in this image. This contour was deformed to fit on the edges in the image by applying a minimal cost contour detection algorithm, which is based on dynamic programming techniques[9,10]. The resulting contour was then used as a model contour for the next step in the automated contour detection procedure for the other phases of the study.

Chapter

4

4.2.5 Motion detection

Given the model contour describing the cross-sectional shape of a vessel in a particular time frame within the cardiac cycle, the position of the same vessel at the other time frames was estimated by shifting the model contour in a limited circular region around the initial location and examining the median edge strength measured in the modulus image along the contour points. The edge strength at a contour point was measured by taking the first derivative in a direction perpendicular to the local contour direction. The computed edge strength values were stored in a motion matrix for each of the locations (dx, dy) evaluated. Entries in the motion matrix with relatively high edge strength values, suggest a probable contour translation. If however, for each time frame the contour would be translated according to the entry in the motion matrix with the maximum edge value, the resulting temporal series of contours would often show unrealistic position changes. The algorithm as depicted in Figure 4-2 was devised to detect a series of contours that move smoothly from phase to phase. For each time frame a two-dimensional cost array was created; each element in this matrix was assigned the inverse of the median edge strength for the corresponding contour location. For the time frame from which the model contour originated, the center element of the cost array was set at cost zero and the other elements at infinity. A closed path with minimal cumulative cost through the series of cost arrays was computed

using dynamic programming strategies[9]. This path represents the displacement of the vessel of all available time frames relative to the position of the model contour. The position of the contour was allowed to move two pixels from frame to frame and 10 pixels from the original model contour position at maximum.

4.2.6 Deformation detection

Given a contour which is an approximation of the vessel boundary resulting from the algorithm which was used for motion correction, a final optimized contour was detected by allowing small deformation of the model contour such that it would follow the edges in the modulus image. For this purpose a two-dimensional graph searching technique was used, often denoted as minimum cost contour detection[10]. In short, for each time frame a rectangular scan matrix is constructed by resampling the modulus image perpendicular to the model contour. From this matrix a cost matrix is constructed by taking for each line at each position the first derivative value at the corresponding position and line in the scan matrix. An optimum closed path with minimum cost through the cost matrix is found resulting in the final contour for the image. Since this contour connects the pixel positions with maximum edge strengths, the resulting contour was dilated by one pixel to account for partial volume effects and to be sure to encompass the complete region with flowing blood.

4.2.7 Analysis procedure

Manual and automated image analyses were performed by two independent observers (RvdG, AN). To assess intraobserver variabilities, the first observer repeated the automated and manual analyses after a two week interval. The flow quantification package ran on a commercially available SUN Ultra Sparc 1 workstation (Sun Microsystems, Mountainview, Ca).

4.2.8 Manual analysis

During manual tracing of contours the observer was allowed to use the phase and modulus image simultaneously. A movie loop showing both phase and modulus images, with superimposed contours was used to facilitate the interpretation of the images. Great care was taken to include all visible flow in the phase images and to avoid regions of flow belonging to the inferior vena cava often lying adjacent to the aorta.

Modulus images for a complete cardiac cycle
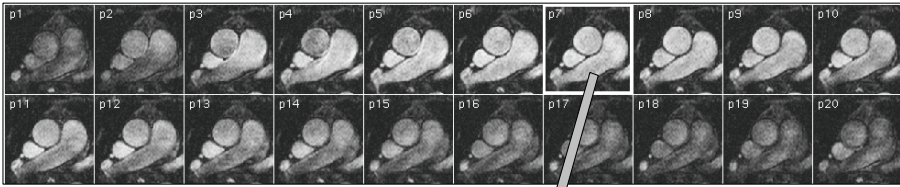
Modulus image from phase 7 with model contour automatically detected from center point
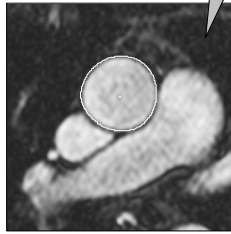
Motion matrices for phase 1 to 20 with optimal contour displacement indicated (+).
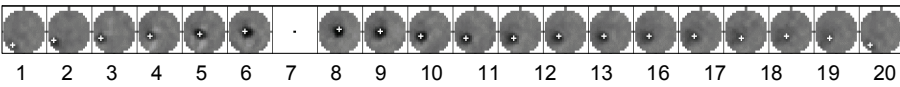
Result after motion detection
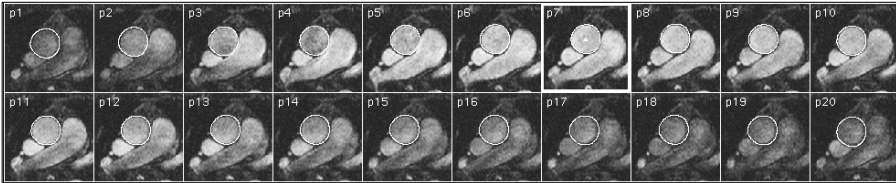
Result after deformation detection
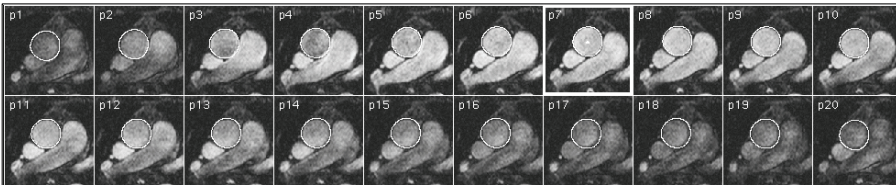
Figure 4-2. Graphical representation of the individual steps of the automated contour detection algorithm for a time-series of images of the ascending aorta.

4.2.9 Automated analysis procedure

The image analysis using the automated contour detection algorithm started with loading of all the phase and modulus images of a study into the flow quantification package. The time frame with optimal vessel depiction in the magnitude image was selected for display. In most cases this time frame corresponded to a cardiac phase in early diastole. In case the magnitude image showed overlap of the ascending aorta with the pulmonary artery, another time frame was selected. In the selected image an approximate center was manually indicated. From this center a contour was detected automatically. In case of a failure of the contour detection for this image, the next or previous time frame was selected to initiate the contour detection procedure. Subsequently, the motion detection algorithm was applied to estimate the translation of the vessel cross section for each time frame. The resulting contours were used as models for the deformation detection algorithm, resulting in optimally adjusted contours for each image. In no case were manual corrections allowed.

In the experiments described in this study, the model contour was allowed to deform ± 4 pixels (3.1 mm) in the radial direction. The maximum motion allowed was set to ± 10 pixels (7.8 mm). In one subject the amount of motion of the ascending aorta was much larger than this value and the maximum allowed motion for this case was set to ± 15 pixels. The total analysis time for automated analysis was approximately 6 seconds. The resulting contours and the location of the manually indicated center point of an analysis session were saved on disk.

4.2.10 Data analysis

From the vessel boundary contours which were manually traced by the first observer the actual in-plane motion and deformation of the vessel boundary over the cardiac cycle was evaluated within the study population. The center of gravity of each contour was computed and the maximum displacement of this point with respect to the end-diastolic time frame was computed. To study the shape changes of the vessel boundary of the aorta over the cardiac cycle, the relative increase of the contour area from the end-diastolic phase (time frame 1) to the time frame with maximum area was computed for each study.

From the automatically and manually determined contours, flow curves were constructed by computing instantaneous flow (i.e. the product of the contour area and mean flow velocity within the contour) at each time frame. From these curves, stroke volume measurements were obtained by integrating the flow over the complete cardiac cycle. Results derived from manual contour tracing were compared to results from automated contour

detection by computing the mean and standard deviation of the paired signed differences. The same measurements were performed to compare repeat measurements of the same observer and between the two observers for both manual and automated analysis. The mean and standard deviation of the paired differences of repeat measurements were expressed as a percentage of the mean. A Student t test was used to test the statistical significance of the differences observed between and within observers. Statistical significance was defined as p<0.05.

Table 4-1. Mean values and inter- and intraobserver variabilities for the assessment of stroke volume using either manual contour tracing or automated contour detection. The mean and standard deviations of paired differences of repeat measurements are presented

		Manual	Auto
Luminal area	Mean [cm^2]	7.26 ± 1.56	6.98 ± 1.40*
	Intraobserver difference [%]	-2.08 ± 6.28*	0.34 ± 2.15*
	Interobserver difference [%]	0.73 ± 5.43*	0.75 ± 2.56*
Stroke volume	Mean [ml]	88.14 ± 14.48	87.73 ± 14.49
	Intraobserver difference [%]	-0.23 ± 0.85	0.72 ± 1.25*
	Interobserver difference [%]	0.83 ± 1.59	0.55 ± 1.20
*: indicates statistical significant difference (p<0.05).			

Chapter

4

4.3 RESULTS

On an average the maximum displacement of the contour center relative to the end-diastolic phase was 7.1 ± 2.1 mm (9.0 ± 2.6 pixels); range 5.1-12.0 mm (6.5-15.4 pixels). The average increase in cross-sectional area of the aorta relative to the end-diastolic phase was 24.0 ± 10.9%.

Figure 4-2 shows an example of flow curves of one of the study subjects, obtained by manual and automated contour detection. The mean stroke volume within the study population obtained by manual contour tracing was 88.1 ± 14.5 ml. Figure 4-3 demonstrates that the results of automated contour detection were in excellent agreement with the results from manual image analysis. The mean signed difference between the two methods of contour definition was found to be 0.41 ± 0.77 ml (0.61 ± 1.15%, p=NS), representing a small but non-significant underestimation in stroke volume by the automated contour detection method. In Table 4-1, the results of intra- and interobserver analysis are presented. For both manual and automated image analysis, the reproducibility of stroke volume measurement proves to be excellent. The signed differences and the standard deviations of the differences are always less than 2% of the mean values.
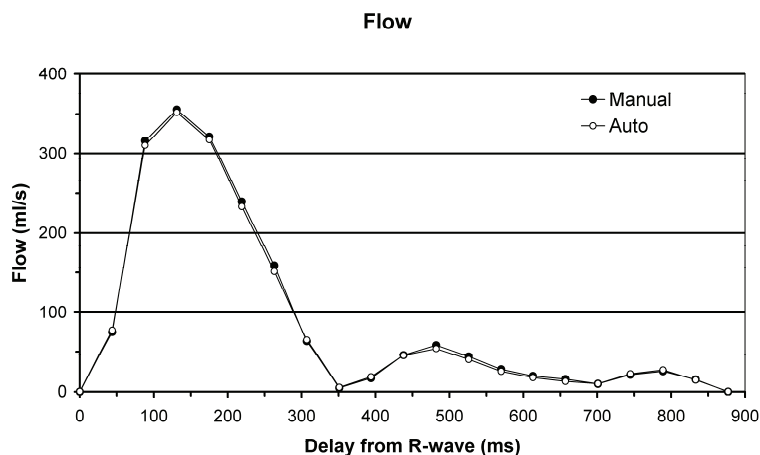
Figure 4-3. Example of flow curves obtained from manually (●) and automatically (○) determined contours. Along the horizontal axis the cardiac phase number is displayed; the vertical axis depicts the instantaneous flow rate.

4.4 DISCUSSION

Velocity-encoded MRI of the ascending aorta provides a non-invasive means of assessing left ventricular stroke volume. The accuracy and reproducibility of this technique has been proven in various studies [6,7]. In the current study a conventional phase-contrast MRI technique was used, requiring 2-3 minutes of acquisition time. Faster imaging techniques which are based on echo-planar, or segmented k-space (multi-shot) techniques make it possible to reduce the imaging time to a single breath hold, and are becoming widely available on most modern MR scanners [11,12]. Quantification of stroke volumes from the acquired MR images requires an accurate delineation of the boundaries of the aortic lumen in each of the images, which is a time-consuming and tedious procedure when performed manually. From the measured maximum in-plane displacement of 7.1 ± 2.1 mm ($25 \pm 7.3\%$ of the average ED diameter) and the maximum observed change in cross-sectional area of $24 \pm 11\%$, corresponding to a change in diameter of about 3.19 mm or 4.1 pixels, it is evident that the contours to be drawn need to be repositioned and adjusted for each individual phase. In the current study the number of acquired phases was only twenty, but still the time required for manual contour tracing was in the order of ten minutes. If this technique is to be used for clinical purposes, it would be beneficial to reduce the analysis time. The present contour detection algorithm performs the automated detection in less than 6 seconds and is in excellent agreement with manually defined contours. Also, both the

inter- and intraobserver variabilities of the automated contour detection of less than 2% of the mean stroke volume demonstrate the robustness of this new approach. The variability of the measurements is explained by the required operator interaction, which is the manual definition of the aortic center in one of the available images. The contour automatically derived from this center, serves as a model (example) for the automated detection in the other phases within the study. Since in this study the operator was free in choosing in which image the center was indicated, some variability will be introduced in both the motion estimation step and the final deformation detection due to differences in the model contour.
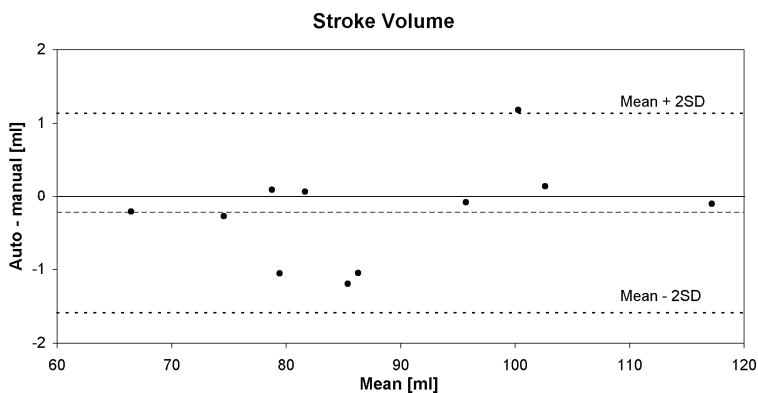
Figure 4-4. Differences in stroke volume measurements obtained by manual contour tracing and by automated contour detection as a function of the mean stroke volume.

4.4.1 Limitations

Since the automated contour detection algorithm exclusively uses the information from the gradient echo modulus images for the determination of the vessel boundaries, the detected contour may in some cases deviate from the visible flow in the corresponding phase image. Since the blood velocity near the vessel border normally is much lower than in the central region of the vessel, this resulted in no significant error in stroke volumes. Further improvement in the contour detection may be obtained by combining the information from the phase and modulus images simultaneously. However, in many clinical situations the information in the phase image may be misleading since the flow may be zero during most of diastole, and forward and backward flow may exist simultaneously.

In the present study, the new automated contour detection technique was compared to manual contour tracing by comparing just one quantitative parameter (SV). Additionally, no imaging studies from cardiac patients were included in the study subjects, and therefore the image

quality may have been relatively good. It is suggested that a more extensive validation study be performed on a wider variety of patients, including those with aortic regurgitation and aortic valve stenosis, to fully assess the clinical value of the presented automated contour detection algorithm.

The simple fact that a good agreement in SV was found does not necessarily mean that the manual and automated derived contours were nearly identical since the inclusion of regions of stationary tissue or blood in a contour does not affect the stroke volume measurements. However, in the case of the ascending aorta, many regions of flow in different directions are present in the neighborhood of the ascending aorta which definitely would have affected the results. By visual inspection of the manual and automatically detected contours in a cine mode, it could be noted that the automatically detected contours were somewhat more irregular in shape in those phases with little or no flow in the ascending aorta. Since in these phases the velocities in the neighboring regions are also close to zero, this introduced no significant errors in the stroke volume measurements.

4.5 CONCLUSION

In conclusion, an automated contour detection algorithm for the automated assessment of stroke volume from velocity-encoded MR of the ascending aorta has been presented and was validated on MR studies of 11 volunteers. When compared with results by manual analysis, the algorithm has proven to be 50 times faster, while the agreement was excellent and the inter- and intraobserver variabilities were less than 2%. Therefore, the described automated contour detection algorithm will contribute to the clinical applicability of MR velocity mapping in the evaluation of flow in the ascending aorta.

4.6 REFERENCES

1. Firmin DN, Nayler GL, Klipstein RH, Underwood SR, Rees RSO, Longmore DB. In vivo validation of MR velocity imaging. J Comput Assist Tomogr 1987; 11:751-756.
2. Mohiaddin RH, Wann SL, Underwood SR, Firmin DN, Rees S, Longmore DB. Vena cava flow: assessment with cine MR velocity mapping. Radiology 1990; 17:537-541.
3. Rebergen SA, van der Wall EE, Doornbos J, de Roos A. Magnetic resonance measurement of velocity and flow: Technique, validation and cardiovascular applications. Am Heart J 1993; 126:1439-1456.
4. Bogren HG, Klipstein RH, Firmin DN, Mohiaddin RH, Underwood SR, Rees RSO, Longmore DB. Quantitation of antegrade and retrograde blood flow in the human aorta by magnetic resonance velocity mapping. Am Heart J 1989; 117:1214-1222.
5. Szolar DH, Sakuma H, Higgins CB. Cardiovascular application of magnetic resonance flow and velocity measurements. J Magn Res Imag 1996; 6:78-89.

6. Kondo C, Caputo GR, Semelka R, Foster E, Shimakawa A, Higgins CB. Right and left ventricular stroke volume measurements with velocity-encoded cine MR imaging: In vitro and in vivo validation. AJR 1991; 157:9-16.
7. Dulce MC, Mosbeck GH, O'Sullivan MM, Cheitlin V, Caputo GR, Higgins CB. Severity of aortic regurgitation: interstudy reproducibility of measurements with velocity-encoded cine MR imaging. Radiology 1992; 185:235-40.
8. Sondergaard L, Lindvig K, Hildebrandt P, Thomsen C, Stahlberg F, Joe T, Hendriksen O. Quantification of aortic regurgitation by magnetic resonance velocity mapping. Am Heart J 1993; 125:1081-1090.
9. Bellman RE. Applied dynamic programming: Princeton Univ. Press, 1962.
10. van der Geest RJ, Buller VGM, Jansen E, Lamb HJ, Baur LHB, van der Wall EE, de Roos A, Reiber JHC. Comparison between manual and automated analysis of left ventricular volume parameters from short axis MR images. J Comput Assist Tomogr 1997; 21:756-765.
11. Mohiaddin RH, Gatehouse PD, Firmin DN. Exercise-related changes in aortic flow measured with spiral echo-planar MR velocity mapping. J Magn Res Imag 1995; 5:159-163.
12. Debatin JA, Leung DA, Wildermuth S, Botnar R, Felblinger J, McKinnon GC. Flow quantitation with echo-planar phase-contrast velocity mapping: In vitro and in vivo evaluation. J Magn Reson Imag 1995; 5:656-662.

Chapter

4

CHAPTER

5

Assessment of regional left ventricular wall parameters from short axis MR imaging using a 3D extension to the improved Centerline method

ABSTRACT

Rationale and objectives: Short-axis magnetic resonance images of the cardiac left ventricle, acquired in multiple slices and phases, may be used for the quantitative assessment of regional wall parameters. Conventional two-dimensional (2D) methods for wall thickness measurement rely on information within one imaging plane which may result in overestimation of the true thickness depending on the local direction of myocardial wall with respect to the imaging plane.

Methods: In order to perform wall thickness measurements truly perpendicular to the myocardial wall, a three-dimensional (3D) wall thickness calculation algorithm has been developed based on the 2D improved centerline method. An evaluation was performed on left ventricular-shaped software phantoms, and on the MRI data obtained from 20 healthy individuals.

Results: The 3D method applied to software phantoms with an angulation within $20°$ of the true short-axis orientation demonstrated only a 1.6% overestimation of wall thickness at the mid to low slices, and a 10.6% error at the apex (2D measurements: 8.1% and 28.6%, respectively). Three-dimensionally calculated wall thickness in the healthy individuals was systematically and significantly smaller than corresponding 2D wall thickness (by 11.2%, 8.7% and 2.6% at the apical, low and mid slices, respectively).

Conclusions: Cardiac wall thickness measurements from short-axis MR studies can be obtained with a higher accuracy by the newly developed 3D approach than with the conventional 2D approach.

Chapter

5

5.1 INTRODUCTION

Cardiac magnetic resonance (MR) has been generally accepted as an accurate and reproducible modality for the quantitative evaluation of left ventricular (LV) function. Multi-slice, multi-phase (MSMP) MR acquisitions have been found suitable for the accurate assessment of left ventricular volumes[1-3] and mass[4,5], as well as for the assessment of local functional parameters such as wall thickness and wall thickening or thinning[6].

Magnetic resonance imaging acquisitions, in particular in the short-axis orientation, have proven their usefulness for the determination of regional wall parameters[7-10]. Local wall thickness can be derived from these acquisitions by manual or automatic outlining of the endocardial and epicardial boundaries in each short-axis image[9,11,12]. Because true wall thickness is only acquired when measurements are performed perpendicular to the myocardium, achieving this within-image perpendicularity is the goal of advanced two-dimensional (2D) algorithms such as the improved centerline method (Figure 5-1)[13,14].
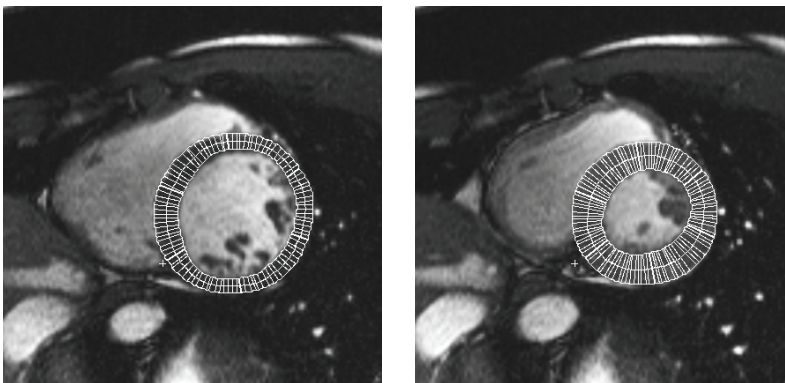
Figure 5-1. A typical short-axis image of a normal individual in the end-diastolic (left) and end-systolic (right) phases of the cardiac cycle with manually drawn contours and centerline chords for planar wall thickness measurement.+ indicates the posterior junction of the right ventricle with the left ventricular wall, where the clockwise numbering of the 100 centerline chords was started

Because such methods are confined to measurements within individual 2D images, the implicit assumption is made that the myocardial wall itself is always perpendicular to the acquisition plane. However, because of the ellipsoidal cardiac geometry this assumption is rarely true, even when true short-axis images are obtained. In particular near the apex, the myocardium exhibits a through-plane curvature which causes the

myocardium and imaging plane to intersect at an oblique angle. Planar, 2D wall thickness methods will therefore inevitably overestimate true wall thickness in a systematic manner (Figure 5-2A). In addition, a randomly distributed error may be introduced in 2D wall thickness measurements in every individual slice if different myocardial regions are inclined differently to the imaging plane. This effect may either occur due to cardiac geometry or be caused by an inaccurate determination of the short-axis orientation (Figure 5-2B).
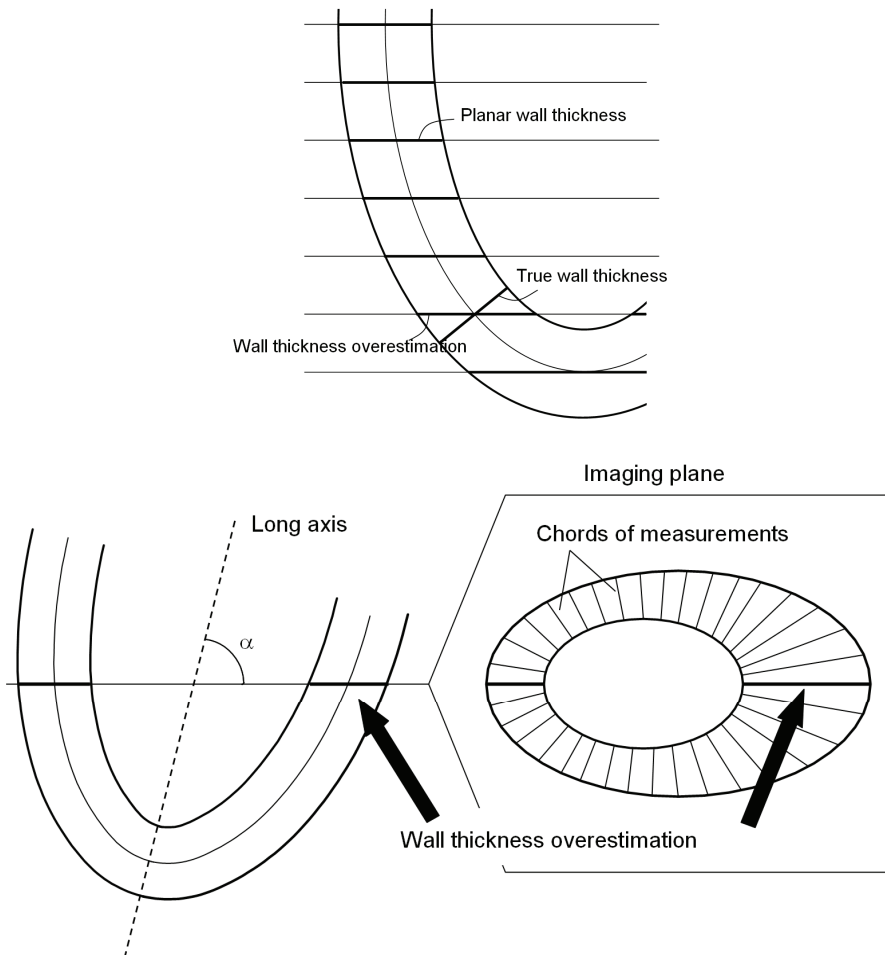
Figure 5-2. (A) Planar wall thickness measurements will overestimate true wall thickness in the lower slices of the left ventricle. The degree of overestimation depends on the angle [alpha], which should be 90° in the ideal situation. (B) Planar wall thickness accuracy will vary along the circumference of the myocardial wall if different segments of the wall have a different inclination with the imaging plane-for example, because of an imprecisely determined short-axis orientation.

However, the myocardial boundaries of a multi-slice, multi-phase MRI acquisition contain three-dimensional (3D) shape information which may be used to prevent both these systematic and random overestimations (Figure 5-3). Therefore, a new 3D wall thickness calculation algorithm has been developed to measure wall thickness always perpendicular to the myocardium, and thus to effectively estimate true wall thickness. In comparison to the existing planar methods, this method was expected to demonstrate a decreased wall thickness in the apical slices, and an increased wall thickness homogeneity within individual images.

In normal patient studies, the new 3D algorithm was expected to decrease wall thickness inter-subject variation because its results would be independent of the cardiac geometry and the orientation of the MR acquisitions. Consequently, 3D calculated wall thickness would result in smaller normal value ranges. The comparison of wall thickness in patients to these smaller normal value ranges may lead to higher sensitivities and specificities in the assessment of the extent and severity of dysfunctional myocardium in patients.

The purpose of this study was an evaluation of the newly developed 3D wall thickness method based on software phantoms as well as on multi-slice, multi-phase short-axis MR acquisitions obtained from 20 healthy individuals.
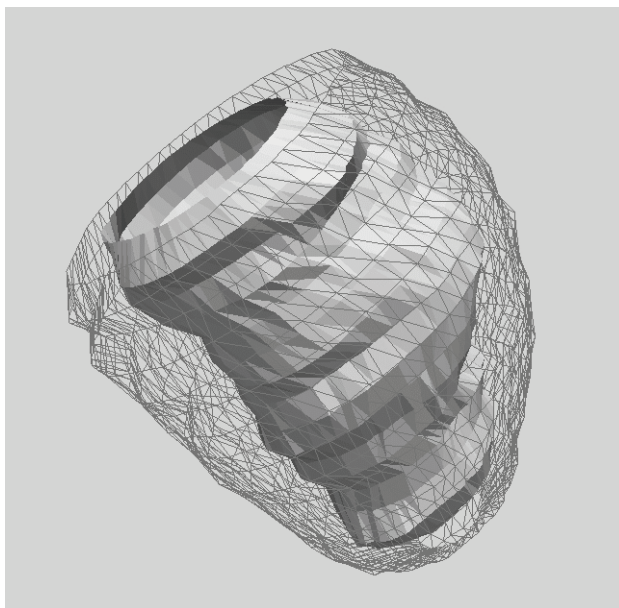
Figure 5-3. A short-axis, multi-slice magnetic resonance imaging acquisition comprises a detailed three-dimensional description of the cardiac left ventricle.

5.2 MATERIALS

5.2.1 The software phantoms

In order to compare the accuracy and precision of the 3D wall thickness method with the conventional 2D method and the true wall thickness values, a software phantom with an overall true wall thickness of 10 mm was constructed. The phantom was given an approximate end-diastolic left ventricular shape and size to ensure a natural occurrence of systematic and random errors in the two-dimensional measurements. To this purpose, the lower portion of the phantom was modeled as an ellipsoid of 70 mm epicardial height, extended at the base by a cylinder with an epicardial diameter of 70 mm (Figure 5-4). The phantom was given a vertical, true short-axis orientation. Twelve similar phantoms were each created at a different, unique tilt angle from the short-axis orientation (from 5° to 60°, in 5° increments).

Chapter

5

All phantom study imaging parameters were chosen similar to the in-vivo normal acquisitions used in this study. The image resolution was 256×256 pixels at a field of view of 400×400 mm², resulting in an average wall thickness of 6.4 pixels. Slice thickness was 10 mm with no inter-slice distance. Slice number 1, the lowest slice, was acquired at the epicardial point of the apex. The slices at levels 2, 3, 5 and 7, representing the apical, low, mid and basal slices of a normal left ventricle, were selected for analysis.
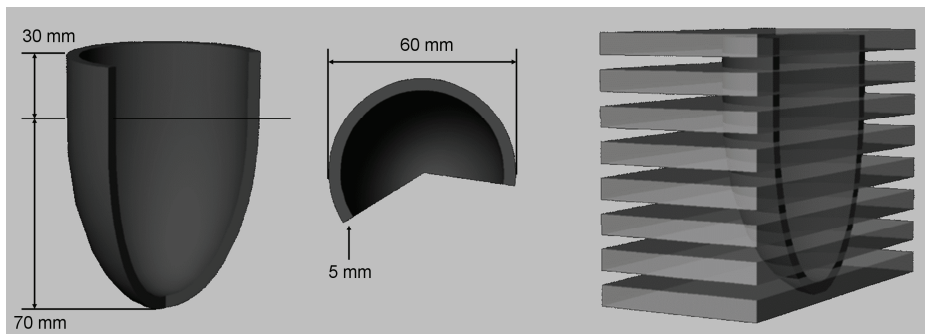
Figure 5-4. The 13 software phantoms were created for the in vitro study. The dimensions of all software phantoms were identical, but only the angle of acquisition was different for each.

5.2.2 In-vivo study data

Twenty normal individuals were selected based on the criteria defined in the Framingham trial[7]. Each included individual had a normal ECG and no

clinical signs or history of cardiac disorder. The mean age for the group was 37.4 years (range 21-78). The gradient-echo MRI studies were acquired on 0.5T (10 cases) and 1.5T (10 cases) MR scanners using the body coil (Philips Medical Systems, Best, The Netherlands). The short-axis orientation was determined by visual inspection of end-diastolic (ED) and end-systolic (ES) phases in a four chamber scout view, such that the short-axis imaging slices were selected perpendicular to the left ventricular long axis. The images were acquired at a field of view of 400x400 mm² and an image resolution of 256×256 pixels. Ten slices of thickness 10 mm (10 cases) or 8 mm (10 cases) were acquired with either a slice gap of 1 mm (15 cases) or 2 mm (5 cases). From these slices basal, mid, low and apical slices were selected independently in both ED and ES phases based on the following criteria: The basal slice was the second slice from the ventricular base to encompass the complete myocardium; the mid slice was the lowest slice in which papillary muscles were still clearly distinguishable from the myocardium, and the low and apical slices were the second and first slice up from the apex with complete endocardial and epicardial outlines.

5.3 METHODS

5.3.1 Software description

5.3.2 The two-dimensional improved centerline method

Two-dimensional wall thickness was calculated with the improved centerline method[13,14]. This planar method allows the assessment of wall thickness at a high resolution, and is independent of generally disregarded geometrical model assumptions such as an approximately circular myocardial shape or a predefined cardiac center point[15]. Instead, the improved centerline method begins by defining a 'centerline' midway between the endo- and epicardial boundaries in each individual image. One hundred measurement chords are then placed at equal distances perpendicular to this centerline. The length of each chord within the myocardium is then a measure of local wall thickness. In a subsequent iterative procedure, crossing chords and other possible anomalies are solved by redistribution and reorientation of the chords in problem areas (Figure 5-1b). The chords were then numbered in clockwise order, starting at the posterior junction of the right ventricle with the LV wall. The independent definition of this starting location in all images at the ED and ES phases compensated for the rotational motion of the left ventricle. Due to the large number of 100 chords per image, a sufficiently high measurement resolution was guaranteed in all images.

5.3.3 The three-dimensional wall thickness calculation

The 3D method extends the planar improved centerline method by incorporating 3D ventricular shape information, and performing wall thickness measurements perpendicular to the ventricular wall.

The 3D method constructs a 3D mid-myocardial surface S, describing the shape of the ventricular wall, through all the centerlines calculated by the planar centerline method (Fig 5-5a). By definition, all midpoints of the 2D centerline chords are on this surface S. At each of these midpoints a tangent plane P is constructed to the surface S from an in-plane or horizontal ($\vec{h}$) and a vertical ($\vec{v}$) vector component (Figure 5-5d). The horizontal vector $\vec{h}$ at a particular position is calculated by vector-averaging the centerline chord at hand with its two neighbors and rotating the resulting vector through 90° within the horizontal plane (Figure 5-5b). The vertical vector $\vec{v}$ is derived by averaging the two upward pointing vectors between the midpoint and its closest neighboring points in the two adjacent slices (Figure 5-5c).

Next, the angle α (see Figure 5-2b) between the normal vector of the imaging plane and the normal vector of the constructed plane P is calculated. The three-dimensional wall thickness WT_{3D} may then be derived from the 2D wall thickness measurement WT_{2D} using equation 5-1:

$$WT_{3D} = WT_{2D} \times \sin(\alpha) \qquad\qquad (5\text{-}1)$$

The basic 3D algorithm described above uses planar measurements from the current slice and its two adjacent slices. A variant algorithm was conceived for the uppermost and lowest slices where only one neighboring imaging slice is present. In these cases the vertical vector $\vec{v}$ is defined to be equal to the vector between the current centerline midpoint and its closest neighboring midpoint in the adjacent slice.

5.3.4 Evaluation methods

Phantom study data

A quantitative evaluation concerning the accuracy and precision of the planar and 3D methods was performed on the software phantom data. To assess the presence and extent of random errors introduced by deviations in short-axis orientation, wall thickness was measured in software phantoms at all given acquisition angles. The 100 chord measurements per slice were averaged, and minimum, maximum and standard deviations

were calculated. In order to also establish the presence and extent of the systematic error due to the curvature of the cardiac wall near the apex, results at 4 different slice levels were determined.
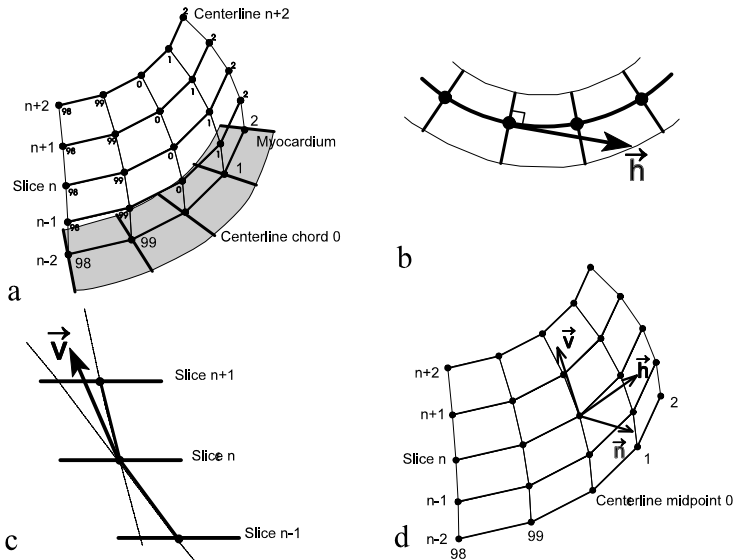
Figure 5-5. (A) A surface can be constructed from a stack of centerlines running midway between the endocardium and epicardium. At each center point on this surface (B) horizontal and (C) vertical direction vectors can be constructed from adjacent centerline chords. (D) These vectors define a plane tangent to the mid-myocardial surface. The angle between the normal vector of this plane and a normal vector of the imaging plane then defines the local inclination between myocardium and imaging plane.

In-vivo study data

In order to determine the effectiveness of the 3D method on clinical data and in the establishment of accurate normal value ranges, a quantitative evaluation was carried out on the in-vivo studies of 20 healthy volunteers.

In each in-vivo study the endocardial and epicardial contours were manually traced by an experienced observer in all images with a completely visible myocardium (distinguishable endocardial and epicardial boundaries, slices only below aortic valve level). These contours were traced to encompass only the myocardial wall, and to exclude papillary muscles and trabeculae. In case the myocardial boundary was imaged with some blurring due to the partial volume effect, the contour location was chosen to be on the center of the visible boundary. All manual analyses were performed under identical lighting conditions and fixed display window and level settings.

In each study ED and ES phases were selected as the first imaged cardiac phase and the phase with the smallest calculated blood pool volume, respectively. Wall thickness was measured with both methods at 100 chord positions in all slices of both phases. The 100 chord measurements per slice were averaged, and minimum, maximum and standard deviations were calculated.

The wall thickness measurements were further grouped into three anatomical regions using the clockwise order of the centerline chords. Starting at the posterior junction of the right ventricle with the left ventricular wall, the first 20% of the chords was considered septal and the next 30% anterior. The remaining 50% was defined a lateral/posterior region. Wall thickness calculated by both planar and 3D methods in these three regions were compared in slices from base to apex.

5.4 STATISTICAL ANALYSIS

Student's paired t-tests were used to compare planar and 3D wall thickness measurements at each of the defined slice levels. Wall thickness normal bands were computed based on the 20 normal individuals with both the planar and 3D methods. Normal ranges were defined by the mean plus/minus twice the standard deviation (SD) to approximate the 95% probability interval.

Chapter

5

5.5 RESULTS

5.5.1 Phantom study

Figure 5-6 shows a comparison between the wall thickness results computed by the 3D and 2D methods for the slices 2, 3, 5 and 7 of the software phantoms. The planar (2D) measurements (left column) demonstrate an obvious overestimation of true wall thickness in those phantoms which have been positioned at an oblique angle with the imaging plane. In slice 7 one can see that wall thickness is rather accurately calculated in the true short-axis phantom (at zero degrees in each graph), but that both average and maximum measured wall thickness values rapidly increase when the phantoms become more angulated with respect to the short-axis orientation. The wall thickness results acquired with the 3D method do not display such overestimation, not even in the phantom with the largest angulation of 60° to the true short-axis orientation. The precision of the individual 2D centerline measurements is expressed in terms of the standard deviation calculated over the one hundred measurement chords in each phantom image. At all four slice levels, this standard deviation increases when examining phantoms at increasing

acquisition angles. In contrast, results assessed with the 3D method demonstrate a standard deviation which is insensitive to acquisition angle, and is therefore generally much lower than comparable planar measurements.

Table 5-1. Wall thickness (in mm) in five software phantoms at an approximately short-axis orientation

Angle	Dimension	Slice 2 (Apical) Mean (±SD)	Slice 3 (Low) Mean (±SD)	Slice 5 (Mid) Mean (±SD)	Slice 7 (Basal) Mean (±SD)
0 º	2D	12.8 (0.41)	11.2 (0.28)	10.5 (0.35)	10.0 (0.24)
	3D	11.0 (0.34)	10.1 (0.26)	10.3 (0.33)	10.0 (0.24)
5º	2D	12.9 (0.56)	11.2 (0.42)	10.4 (0.30)	9.9 (0.33)
	3D	11.1 (0.33)	10.1 (0.35)	10.3 (0.28)	9.9 (0.33)
10 º	2D	13.0 (0.66)	11.1 (0.59)	10.4 (0.30)	10.1 (0.30)
	3D	11.2 (0.34)	10.1 (0.30)	10.2 (0.26)	10.0 (0.31)
15 º	2D	12.7 (1.02)	11.2 (0.71)	10.4 (0.33)	10.2 (0.33)
	3D	11.0 (0.38)	10.1 (0.36)	10.2 (0.30)	10.1 (0.30)
20 º	2D	12.8 (1.11)	11.0 (0.73)	10.5 (0.40)	10.2 (0.31)
	3D	11.1 (0.39)	9.9 (0.36)	10.2 (0.24)	9.9 (0.26)

Planar and three-dimensional wall thickness figures in mm from five near short-axis software phantoms at different inclinations with the imaging plane, as mean (± SD). The angles denote the deviation from the short-axis orientation. Overall true phantom wall thickness was 10.0 mm.

The effect of the curvature of the myocardium towards the apex, the second possible cause of overestimation in 2D assessed wall thickness, may be isolated from the aforementioned effects by only examining the true short-axis phantom at different slice levels. Figure 5-6 demonstrates that 2D acquired average wall thickness in this phantom displays the largest overestimation of true wall thickness in slices close to the apex (shown for slice 2). Table 5-1 lists the wall thickness results in phantoms up to 20° from the short-axis orientation in tabular form. It shows that at a 10° deviation from the true short-axis orientation for example, which may be considered comparable to clinical practice, measured wall thickness varied from 10.1 mm to 12.5 mm (mean 11.1 mm) at slice 3, and from 11.8 to 14.3 mm (mean 13.0 mm) for the apical slice 2. In comparison to the phantom true wall thickness of 10.0 mm, maximum errors of up to 43% at the apex (mean error 30%) occur. The 3D measurements significantly reduced this error to mean values of 12% and 1% for slices 2 and 3, respectively.
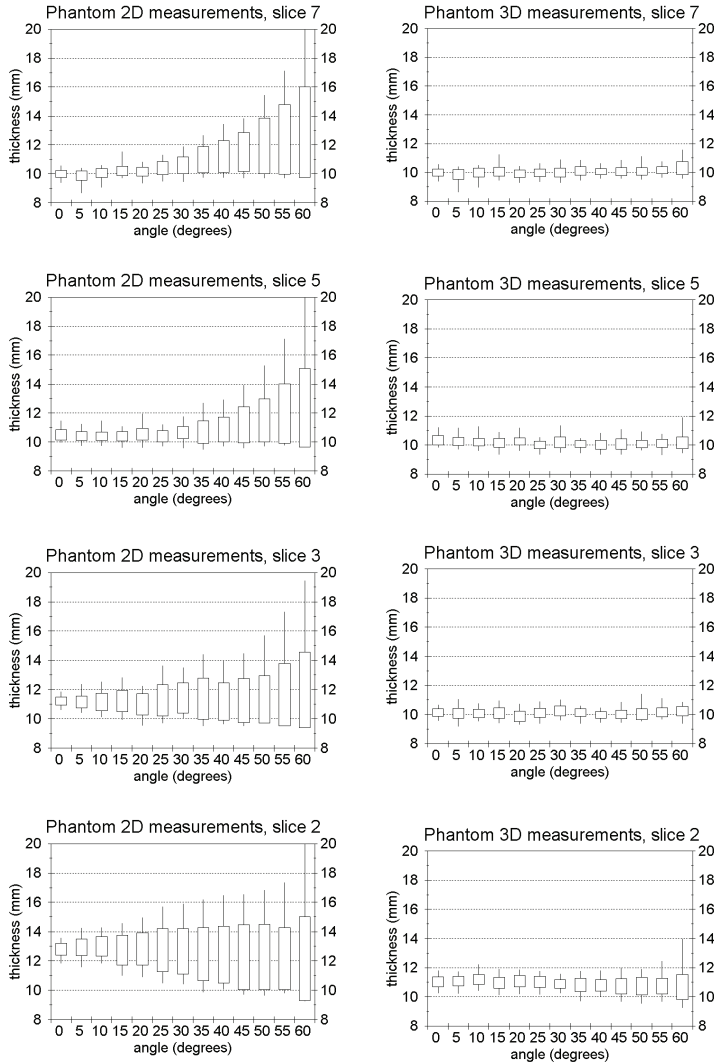
Figure 5-6. Two-dimensional (2D) and three-dimensional (3D) measurements from software phantoms at angulations between 0° and 60° from the short-axis orientation. The graphs on the left (A, C, E, G) display the results for the 2D measurements for slice 7, 5, 3, and 2 respectively; on the right (B, D, F, H) the corresponding results for the 3D measurements are shown.

5.5.2 In-vivo study

Table 5-2 lists the wall thickness measurements from 20 normal individuals by both the 2D and 3D methods, performed at each slice level (Apical / Low / Mid / Basal) in the two cardiac phases (ED/ES). The difference between both methods is also expressed as a percentage decrease in measured wall

thickness implied by the 3D method's correction. All these differences including those at the highest slice level were statistically significant (p<0.05). Table 5-2 also lists the standard deviation (SD) of the 100 measurement chords within each single image, averaged over the 20 individuals. The 3D method also results in a smaller standard deviation compared to the 2D measurements, as is shown by the percent difference between the methods.

Table 5-2. Wall thickness at four levels in 20 healthy volunteers			
	Apical	Low	Mid	High
ED	Mean (SD)	Mean (SD)	Mean (SD)	Mean (SD)
2D [mm]	6.52 (1.00)	6.92 (0.93)	7.09 (0.87)	7.62 (0.92)
3D [mm]	5.79 (0.77)	6.32 (0.84)	6.90 (0.87)	7.56 (0.91)
Diff. [%]	11.24* (22.90)	8.67* (10.13)	2.57* (0.31)	0.73* (0.90)
ES				
2D [mm]	11.43 (2.18)	12.90 (1.96)	13.30 (2.07)	12.84 (1.81)
3D [mm]	10.63 (1.90)	12.22 (1.73)	12.97 (1.92)	12.73 (1.79)
Diff. [%]	6.96* (12.89)	5.28* (11.64)	2.51* (7.44)	0.92* (1.47)

Mean (in-slice SD) wall thickness in 20 healthy volunteers, and the percent difference in mean between the 2D and 3D methods. Both mean and SD were lower when calculated in 3D (* p<0.05).

The differences between both methods in average wall thickness are also reflected in the normal value graphs for the low and apical slice levels (Figure 5-7). In these graphs the normal values have both smaller ranges as well as a lower average value when assessed in 3D compared to the planar method. It is also shown however, that this observed global difference between the 3D and 2D thickness methods is not equally large in different regions along the myocardial circumference. As a result, the 3D graphs show a much more homogeneous wall thickness pattern along the myocardial circumference compared to the planar measurements.

When the myocardial circumference is divided into three distinct anatomical regions, it is apparent that regional planar wall thickness results are increasingly different in slice levels close to the apex, whereas the 3D results are not (Figure 5-8). In all slices, the septal region displays almost identical planar and 3D results, while the anterior region shows very different results computed by the planar and 3D methods.

Overall it can be observed that the large wall thickness inhomogeneity associated with the planar measurements is decreased by applying the WT3D method. There is, however, a difference between ED and ES in percentage wall thickness decrease imposed by the 3D method, which makes this decrease in inhomogeneity much less obvious at ES.
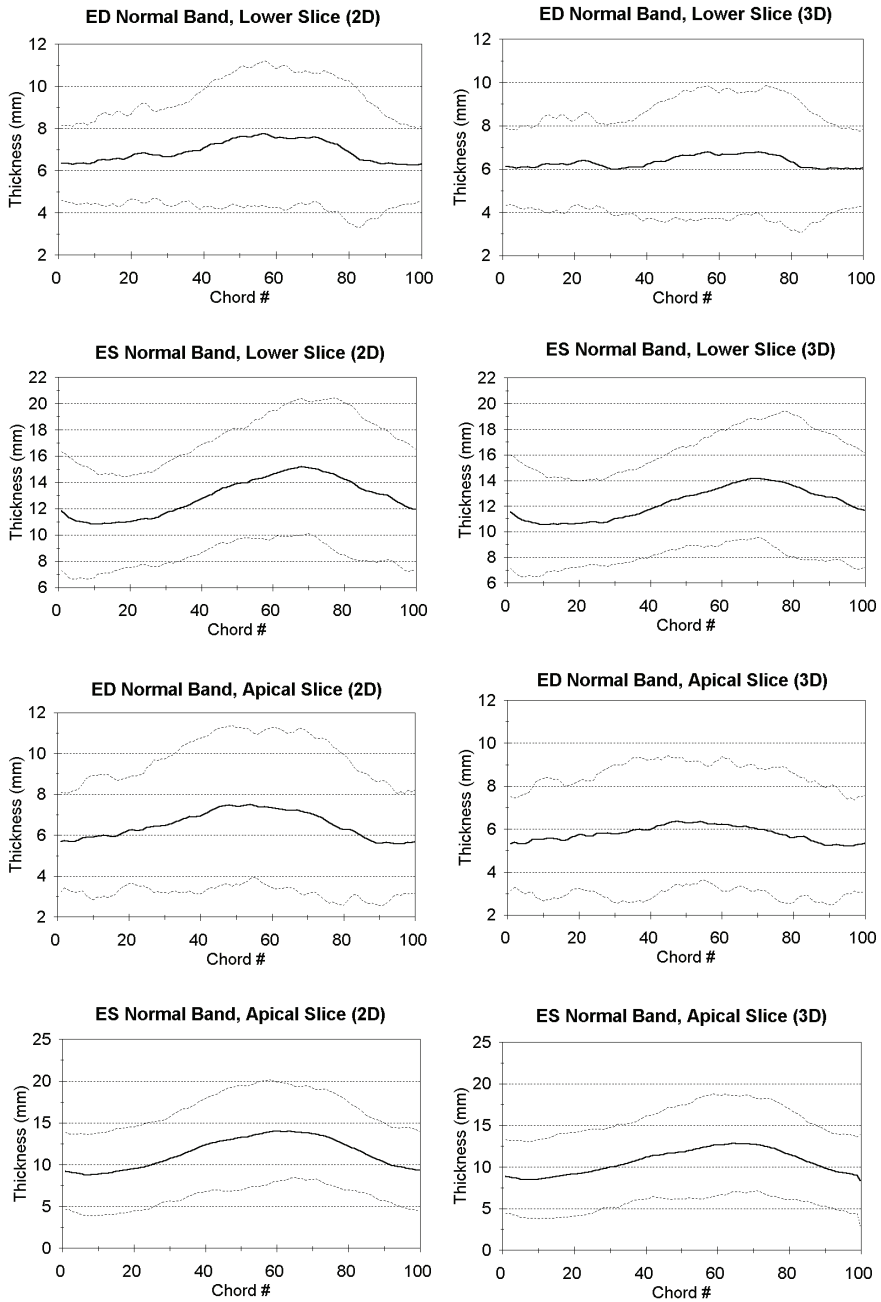
Figure 5-7. The normal wall thickness values in the end-diastolic (ED) and end-systolic (ES) phases determined from the 20 healthy volunteers plotted for two-dimensional (A, C, E, G) and three-dimensional (B, D, F, H) measurements in the lower slice and the apical slice.
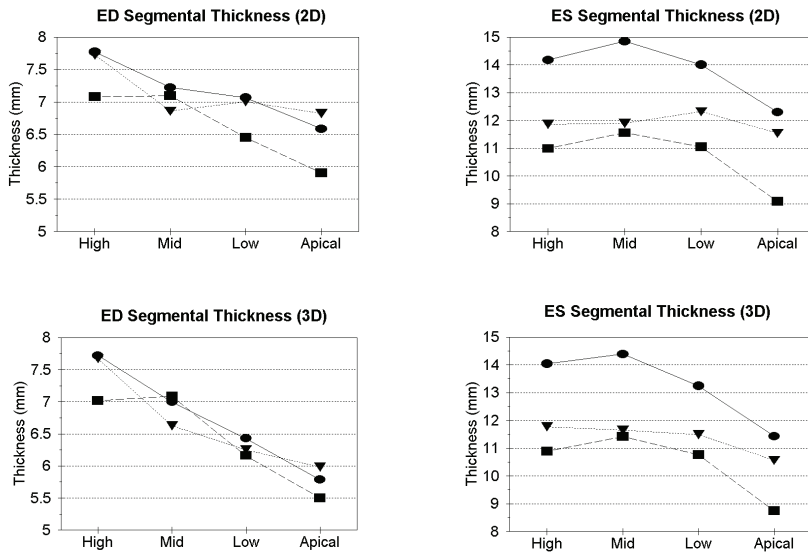
Figure 5-8. Wall thickness values for the individual anatomical regions (septal= chord 1-20; anterior = 21-50; lateral/posterior = 51-100). Results are shown for two-dimensional (top row) and three-dimensional (bottom row) measurements in the end-diastolic and end-systolic phases.

5.6 DISCUSSION

The three-dimensional nature of a multi-slice, multi-phase short-axis MR acquisition of the left ventricle makes it an excellent choice for assessing regional functional parameters, such as wall thickness and thickening or thinning. Straightforward 2D wall thickness measurements within the imaging plane however, overestimate true thickness depending on the location of the measurement along the myocardial wall.

5.6.1 Accuracy of 3D wall thickness assessment

In order to accurately estimate true myocardial wall thickness, a 3D wall thickness calculation algorithm was developed and evaluated. Since the algorithm was based on a correction of the planar measurements by the known improved centerline method, a high planar resolution was achieved. In addition, 2D and 3D measurements could be performed at identical positions along the myocardium enabling a one-to-one comparison of 2D and 3D measurements. Planar wall thickness measurements with the Improved Centerline method on the ventricular shaped phantoms confirmed the expected inaccuracies of the planar method. At the apical slice wall thickness was systematically overestimated, and in the phantoms

with a tilt relative to the imaging plane an increase in random error was observed. In contrast, the developed 3D method did accurately estimate true wall thickness, independent of slice location and long-axis orientation. At places where the imaging plane was indeed perpendicular to the phantom's myocardium, and the 2D centerline method was thus a good measure of the true wall thickness, the correction by the 3D method was minimal and results similar to the 2D measurements were obtained. At the level of the most apical slice, the 3D method was only able to compensate for approximately half the planar error. This is caused by the myocardial surface model used in the calculations, which only extends as far as the acquired basal and apical slices. Local, vertical myocardial curvature at these outer slices could therefore not accurately be estimated. Extrapolation of the surface model towards the apex based only on the visible epicardium might solve this problem. However, special care should be taken not to introduce new errors into the results.

Chapter

5

5.6.2 Alternative solutions to 3D wall thickness assessment

The need to use 3D techniques to accurately estimate true wall thickness from multi-slice short-axis acquisitions has been reported earlier[16-18]. Specific implementations of such techniques have been suggested, all of which based on volume element algorithms. These volume element algorithms partition the myocardium into relatively large myocardial volumetric segments, often in-between the image slices, and derive average wall thickness for each element from its volume and geometric assumptions about its shape. Volumetric methods further define myocardial segments in each myocardial volume ring by either an MR radial tagging acquisition protocol[18,19] or software generated radii from a given ventricular center point[16]. The number of segments thus defined along the circumference of the myocardium is limited, for example to 8, 12 or 16 segments[17,18,20]. Applied to image material from this study only the latter method would achieve an in-slice measurement sampling rate that is comparable to the 10 mm distance between the imaging slices.

A minimum requirement for any wall thickness assessment method must be a correct mapping of myocardial segments to a distribution map of the coronary arteries in order to enable a correlation between impaired myocardial function and reduced coronary arterial supply. In practice, this mapping is very difficult to obtain in a straightforward fashion, and is therefore substituted by a mapping based on anatomical features obtained from the image[21]. To facilitate an accurate mapping of myocardial segments, and to prevent obscuring of small details in the regional functional analysis due to the averaging process, a sufficiently high planar

sampling resolution is required. The presented 3D method makes use of the high image resolution present by performing 100 measurements per image, and thereby facilitates a more than accurate mapping to anatomical features in the image.

5.6.3 Effects of 3D assessment on the normal population results

The greater 3D circumferential wall thickness homogeneity within imaging slices of the normal population was in accordance with the expectations dictated by theory and the phantom experiments. This phenomenon is also in accordance with reports from Beyar[16,17], whose experiments on normal canine hearts also demonstrated a lower standard deviation per slice when thickness was measured in three dimensions.

Figure 5-8 demonstrated that the difference between planar and 3D methods is largest at the anterior region, most likely due to a larger myocardium-to-imaging plane inclination compared to other myocardial regions. In contrast, almost no difference between both wall thickness methods exists in the septal region, where myocardial wall and imaging plane can be expected to be almost perpendicular. It is thus shown that planar wall thickness measurements are likely to randomly overestimate regional thickness even in optimally acquired, true short axis acquisitions.

Although the 3D method decreased differences in normal wall thickness between different myocardial segments, it could not be attributed to significantly smaller normal bands. Differences in myocardial wall inclination therefore can not be a main cause for planar thickness variation between normal subjects. The wide range in normal thickness results is thus more likely attributed to differences in each normal individual's anatomy associated with age and physical condition which were not explicitly defined in this study.

5.6.4 3D assessed wall thickening

Wall thickening is a well known measure for local myocardial function, and is superior to other methods such as wall motion in discriminating between normal and dysfunctional myocardium when calculated in-plane[9] as well as in three dimensions[20]. It is, however, very sensitive to the accuracy of wall thickness measurements, especially in the end-diastolic phase[11]. Application of more accurate 3D wall thickness assessment may thus be advantageous in achieving a more accurate description of cardiac function.

5.7 CONCLUSION

A new 3D wall thickness method has been developed which demonstrated the ability to estimate true wall thickness in phantom studies with a higher accuracy and precision than current planar methods. The method makes use of the well-established, accurate 2D improved centerline method and therefore performs measurements at a high planar resolution. It exploits the 3D information present in multi-slice, multi-phase short-axis MR images of the left ventricle, providing a detailed insight into local left ventricular functioning. Application of the 3D method to short-axis MR studies of 20 healthy volunteers has shown an increase in wall thickness homogeneity along the circumference of the LV wall, leading to more homogeneous wall thickness normal values at each individual slice level. The use of a 3D method is an essential prerequisite for the derivation of accurate wall thickness normal data from a population of normal individuals, and may also be important in the assessment of regional wall thickening.

Chapter

5

5.8 REFERENCES

1. Dinsmore RE, Wismer GL, Miller SW, Thomson R, Johnston DL, Liu P, Okada RD, Saini S, Brady TJ. Magnetic resonance Imaging of the heart using imaging planes oriented to cardiac axes: experience with 100 cases. AJR 1985; 145:1177-1183.
2. Buser PT, Auffermann WW, Holt WW, Wagner S, Kircher B, Wolfe C, Higgins CB. Noninvasive evaluation of global left ventricular function with use of cine nuclear magnetic resonance. J Am Coll Cardiol 1989; 11:1294-1300.
3. Semelka RC, Tomei E, Wagner S, Mayo J, Kondo C, Suzuki J, Caputo GR, Higgins CB. Normal left ventricular dimensions and function: Interstudy reproducibility of measurements with cine MR imaging. Radiology 1990; 174:763-768.
4. Shapiro EP, Rogers WJ, Beyar R, Soulen RL, Zerhouni EA, Lima JAC, Weiss JL. Determination of left ventricular mass by magnetic resonance imaging in hearts deformed by acute infarction. Circulation 1989; 79:706-711.
5. Pattynama PMT, Lamb HJ, van der Velde EA, van der Wall EE, de Roos A. Left ventricular measurements with cine and spin-echo MR imaging: a study of reproducibility with variance component analysis. Radiology 1993; 187:261-268.
6. Fisher MR, von Schulthess GK, Higgins CB. Multiphasic cardiac magnetic resonance imaging: normal regional left ventricular wall thickening. AJR 1985; 145:27-30.
7. Haag UJ, Maier SE, Jakob M, Liu K, Meier D, Jenni R, Boesiger P, Anliker M, Krayenbuehl HP. Left ventricular wall thickness measurements by magnetic resonance: a validation study. Int J Cardiac Imag 1991; 7:31-41.
8. van Rugge FP, van der Wall EE, Spanjersberg SJ, de Roos A, Matheijssen NAA, Zwinderman AH, van Dijkman PRM, Reiber JHC, Bruschke AVG. Magnetic resonance imaging during dobutamine stress for detection of coronary artery disease; quantitative wall motion analysis using a modification of the centerline method. Circulation 1994; 90:127-138.

9. Holman ER, Vliegen HW, van der Geest RJ, Reiber JHC, van Dijkman PRM, van der Laarse A, de Roos A, van der Wall EE. Quantitative analysis of regional left ventricular function after myocardial infarction in the pig assessed with cine magnetic resonance imaging. Magn Reson Med 1995; 34:161-169.

10. Baer FM, Smolarz K, Theissen P, Voth E, Schicha H, Sechtem U. Regional 99mTc-methoxyisobutyl-isonitrile-uptake at rest in patients with myocardial infarcts: comparison with morphological and functional parameters obtained from gradient-echo magnetic resonance imaging. Eur Heart J 1994; 15:97-107.

11. Lamb HJ, Singleton RR, van der Geest RJ, Pohost GM, de Roos A. MR imaging of regional cardiac function: Low-pass filtering of wall thickness curves. Magnetic Resonance in Medicine 1995; 34:498-502.

12. van der Geest RJ, Jansen E, Buller VGM, Reiber JHC. Automated detection of left ventricular epi- and endocardial contours in short-axis MR images. Comput Cardiol 1994:33-36.

13. von Land CD, Rao SR, Reiber JHC. Development of an improved centerline wall motion model. Comput Cardiol 1990: 687-690.

14. Sheehan FH, Bolson EL, Dodge HT, Mathey DG, Schofer J, Woo HK. Advantages and applications of the centerline method for characterizing regional ventricular function. Circulation 1986; 74:293-305.

15. Goodyer AVN, Langou RA. The multicentric character of normal left ventricular wall motion: implications for the evaluation of regional wall motion abnormalities by contrast angiography. Cathet Cardiovasc Diagn 1982; 8:325-232.

16. Beyar R, Shapiro EO, Graves WL, Rogers WJ, Guier WH, Carey GA, Soulen RL, Zerhouni EA, Weisfeldt ML, Weiss JL. Quantification and validation of left ventricular wall thickening by a three-dimensional volume element magnetic resonance imaging approach. Circulation 1990; 81:297-307.

17. Beyar R, Weiss JL, Shapiro EP, Graves WL, Rogers WJ, Weisfeldt ML. Small apex-to-base heterogeneity in radius-to-thickness ratio by three-dimensional magnetic resonance imaging. Am J Physiol 1993; 264 (Heart Circ. Physiol. 33):H133-H140.

18. Lima JA, Jeremy R, Guier W, Guier W, Bouton S, Zerhouni EA, McVeigh E, Buchalter MB, Weisfeldt ML, Shapiro EP, Weiss JL. Accurate systolic wall thickening by NMR imaging with tissue tagging: correlation with sonomicrometers in normal and ischemic myocardium. J Am Coll Cardiol 1993; 21:1741-1751.

19. Dong SJ, MacGregor JH, Crawley AP, McVeigh E, Belenkie I, Smith ER, Tyberg JV, Beyar R. Left ventricular wall thickness and regional systolic function in patient with hypertrophic cardiomyopathy A three-dimensional tagged magnetic resonance imaging study. Circulation 1994; 90:1200-1209.

20. Azhari H, Sideman S, Weiss JL, Shapiro EP, Weisfeldt ML, Graves WL, Rogers W, Beyar R. Three-dimensional mapping of acute ischemic regions using MRI: wall thickening versus motion analysis. Am J Physiol 1990; 259 (Heart Circ. Physiol. 28):H1492-H1503.

21. Schiller NB, Shah PM, Crawford M, et al. Recommendations for quantification of the left ventricle by two-dimensional echocardiography. J Am Soc Echocard 1989; 2:358-367.

CHAPTER

6

Evaluation of a new method for automated detection of left ventricular boundaries in time series of magnetic resonance images using an active appearance motion model

ABSTRACT

The purpose of this study was the evaluation of a computer algorithm for the automated detection of endocardial and epicardial boundaries of the left ventricle in time series of short-axis MR images based on an Active Appearance Motion Model (AAMM). In twenty short-axis MR exams, manual contours were defined in multiple temporal frames (from end-diastole to end-systole) in multiple slices from base to apex. Using a leave-one-out procedure, the image data and contours were used to build twenty different AAMM's giving a statistical description of the ventricular shape, gray value appearance and cardiac motion patterns in the training set. Automated contour detection was performed by iteratively deforming the AAMM within statistically allowed limits until an optimal match was found between the deformed AAMM and the underlying image data of the left-out subject. Global ventricular function results derived from automatically detected contours were compared to results obtained from manually traced boundaries. The AAMM contour detection method was successful in 17 out of 20 studies. The three failures were excluded from further statistical analysis. Automated contour detection resulted in small, but statistically non-significant, underestimations of ventricular volumes and mass: differences for end-diastolic volume were $0.3\pm12.0\%$, for end-systolic volume $2.0\pm23.4\%$ and for left ventricular myocardial mass $0.73\pm14.9\%$ (mean$\pm$SD). An excellent agreement was observed in the ejection fraction: difference of $0.1\pm6.7\%$. In conclusion, the presented fully automated contour detection method provides assessment of quantitative global function that is comparable to manual analysis.

Chapter

6

6.1 INTRODUCTION

Accurate quantification of left ventricular (LV) dimensions is important in the diagnosis of cardiac pathologies and the monitoring of the effect of treatment in various cardiac diseases. Cardiac magnetic resonance imaging allows accurate and reproducible measurements of global LV dimensions such as the end-diastolic (ED) and end-systolic (ES) chamber volumes, the ejection fraction and LV mass[1,2]. The introduction of Steady State Free Precession (SSFP) imaging techniques has resulted in significantly improved endocardial boundary definition, especially in regions of low flow, which were often poorly visualized by the older MRI techniques[3-5]. It has been shown that the SSFP yields an improvement of intra- and interobserver agreement in the assessment of global ventricular parameters when using manually traced myocardial boundaries[6]. Additionally, it was shown that SSFP yields better performance of automated contour detection software[6].

Despite these technical advances in MR pulse sequence development, quantification of the ventricular function parameters is still very much reliant on manual tracing of endocardial and epicardial contours in a large number of images. This post processing procedure adds a significant amount of time to the MR examination and leads to intra- and interobserver variabilities. Recently the concept of Active Appearance Models was introduced as a new framework for automated detection of object boundaries in images[7]. In previous studies we have adapted this AAM technique for the detection of LV and RV contours in 2D images. In the current work we extended the AAM method to operate on temporal sequences of short-axis images acquired using SSFP MRI.

The purpose of the present study was to develop and validate a new automated method for the detection of endocardial and epicardial contours in temporal sequences of short-axis MR images. The proposed method is training-based: it uses available time-series of images with expert drawn contours to build a statistical model of the shape, motion pattern and appearance (gray value in the images) of the left ventricle in time-sequences as seen in short-axis MR images. Once trained on a sufficiently large set of patient data, the statistical model is used to automatically find the cardiac boundaries in new image series. During this step the gray value information in a complete temporal sequence of images from end-diastole to end-systole is used, which guarantees that the method finds a consistent time-continuous segmentation result over the time-sequence. The results of automated contour detection were compared to results derived from manual contour tracings.

6.2 METHODS

6.2.1 Study Population

Eighteen cardiac patients (14 male, 4 female) and two healthy volunteers (all male) without history of cardiac disease were recruited for the study. The mean age of the subjects was 56 years (range 16–76) and mean weight 97 kg (range 54–150). The patients suffered from several pathologies including heart failure (n=8), hypertrophic cardiomyopathy (n=4), transplant follow-up (n=3), chest pain or angina (n=3). All study subjects gave written informed consent to participate in this study.

6.2.2 Magnetic Resonance Imaging

Patients and volunteers underwent MR imaging using a 1.5 T MR system (Sonata; Siemens Medical Systems, Erlangen, Germany). After localizing planes were obtained, a stack of short-axis images was acquired covering the complete left ventricle from apex to base using imaging sections of 6 mm thickness and an inter-section gap of 4 mm. MRI scanning parameters were as follows: TR=3.1 ms, TE=1.6 ms, flip angle=55°, receiver bandwidth=930 Hz/pixel, matrix size=192×256 and FOV=262×350 mm^2.

Chapter
6

6.2.3 Automated Contour Detection Algorithm

Introduction to Active Appearance Models

The newly developed automated contour detection algorithm presented in this paper is based on Active Appearance Models (AAM)[8]. An AAM is a statistical model that can be used to describe the appearance of short-axis MR images, including its typical variations, derived from a training set of example images. In the training set of images, the definition of the cardiac boundaries needs to be available via manually defined contours. An AAM consists of the mean appearance and a number of eigenvariations, which describe the variation in image appearance in the training set. Appearance in this context is a combination of the shape of the ventricle as seen in short-axis images and the gray value information contained in an MR image. For application of an AAM for detection of the LV contours only an image patch containing the LV plus its close surroundings is included in the AAM. By deforming the mean appearance along the eigenvariations, new 'realistic' cardiac MR images can be generated which were not included in the training set, but which are plausible in a statistical sense. To use an AAM for contour detection in cardiac MR images, this deforming procedure is applied to find an optimal match between the deformed AAM and the underlying image. The matching criterion used in our application was the

root-mean-square difference between the image pixels of the MR image and the model synthesized image.

Extension of AAM with Motion Information: AAMM

In previous work we have demonstrated the usefulness of AAM contour detection for the segmentation of the left and right ventricular boundaries in short-axis MR images[7]. This particular algorithm was limited to single two-dimensional images and the validity of the method was demonstrated on mid-ventricular end-diastolic images only. In this work an extension of the AAM contour detection was developed which performs modeling and contour detection for complete time-series of short-axis MR images. Since the method also includes information about the cardiac motion of the left ventricle, the method is called an Active Appearance Motion Model (AAMM). The rationale for this new approach is that we hypothesize that by modeling the image information contained in a time-series of images, the automated segmentation procedure will be more robust since all image data are employed during the detection procedure. By its nature, the segmentation result using AAMM contour detection will represent a time-continuous deformation of the endocardial and epicardial boundaries.

To apply AAMM contour detection for the detection of endocardial and epicardial contours in short-axis MR image series two steps need to be carried out:
1. Building an AAMM using available image data with manually defined expert contours;
2. Matching an AAMM to a new time-series of images by deforming the AAMM until it fits on the image data.

These two procedures are explained in more detail in the following sections.

Building an Active Appearance Motion Model

In the AAMM, the appearance of the left ventricle is modeled for the systolic phase of the cardiac cycle by considering the image frames from ED to ES. An image sequence is normalized to a fixed number of frames T (6) using a nearest neighbor interpolation, so that the ED and ES frames map to the same frame number (1 and 6, respectively). In the training set the endocardial and epicardial contours are defined manually by an independent expert. In each time frame, the image appearance of the left ventricle is modeled as an appearance vector describing the pixel intensity values in an image patch spanned by the manual contour. The vectors for shape points and image patch intensities for each time frame are

concatenated and ordered according to their phase number (1-6). Only imaging sections in which the left ventricular myocardium was visualized for the full circumference in all image frames, were included in the model. Therefore, often one basal and in a few cases an apical section needed to be excluded from the training set of image series. By applying a Principal Component Analysis on the training samples the mean and the most characteristic eigenvariations (modes of variation) of appearance vectors are derived. The resulting AAM describes the average motion pattern that is associated with the cardiac contraction as seen in short-axis cardiac MR images, including the most characteristic anatomical and functional variations in the cardiac cycle (Figure 6-1). In the current implementation no distinction was made between slice levels: apical, mid and basal slices were combined in a single model.
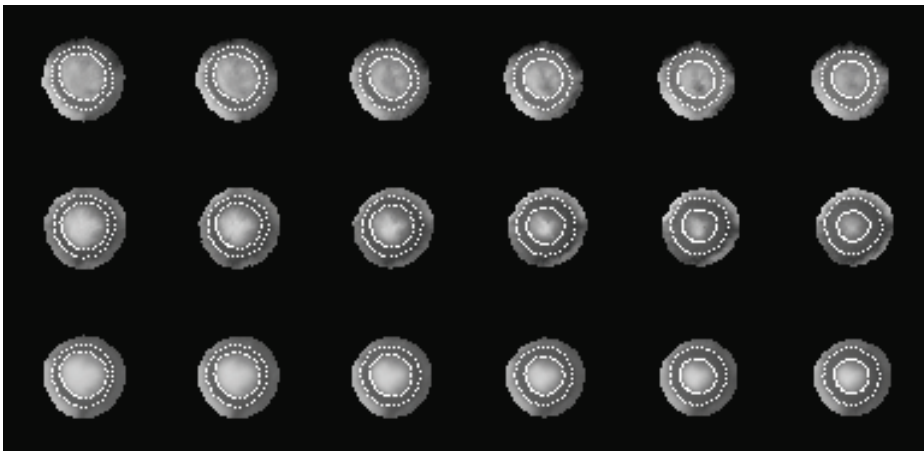
Figure 6-1. Illustration of a trained AAMM with the most important modes of variation. The top row shows the average appearance of the systolic contraction from ED to ES as seen in the short-axis MR images used to construct the AAMM. The middle and bottom rows illustrate the most significant mode of variation represented by the average AAMM plus or minus three times the standard deviation, respectively.

Matching an Active Appearance Motion Model

For each study the only manual interaction required is the definition of the ES time frame; the first time frame is assumed to represent ED. The AAMM is then positioned at the center of the LV using an automatically detected LV center point[9]. For each slice location, six evenly spaced frames from ED to ES are processed simultaneously. Contour detection is performed by automatically adjusting the AAMM parameters until the best fit is found between the deformed AAMM and the underlying image data using an iterative procedure. In the first few iterations the pose of the average appearance is modified using translation, rotation and scaling. In the

Chapter

6

following iterations the appearance is modified by changing the AAMM parameters within ±3 standard deviations. This iterative process continues until a minimum gray value difference (expressed as the root mean square error) is obtained between the model and the six time frames. The matching process results in the endocardial and epicardial contours for all six time frames.

Figure 6-2. (A) Example of a time series of images from ED to ES with manually defined endocardial and epicardial contours (top rows). The endocardial contours are traced around the trabeculations and papillary muscles, which results in a time-continuous motion pattern of the endocardial boundary. (B) Automatically detected contours generated by the AAMM contour detection method. The contours are comparable to the manually traced boundaries illustrated in (A).

6.2.4 Manual analysis

Experienced observers manually traced endocardial and epicardial contours in all cardiac phases and all slice levels in which the myocardium was visualized. Four observers performed the contour tracing, each of them analyzing five exams. The endocardial boundaries were traced around the trabeculations and papillary muscles such that a smooth convex-shaped endocardial contour resulted that exhibits a time-continuous deformation over the cardiac cycle (Figure 6-2A). Epicardial contours were traced at the outer boundary of the myocardium inside epicardial fat when present. Images at the base of the heart showing myocardium for less than 50 percent along its circumference were excluded from analysis. To avoid inconsistencies in image interpretation between observers, one of the observers reviewed all segmentation results and made adjustments to the contours if deemed necessary. In ten randomly chosen subjects manual tracing was carried out by a second observer to assess inter-observer variability. The quantitative ventricular function results derived from the manual tracings served as gold standard.

6.2.5 Comparison between Automatically and Manually Defined Contours

Chapter

6

For evaluation of the performance of the AAMM contour detection methods a leave-one-subject-out approach was used. For each study subject automated detection was carried out using an AAMM that was trained on the remaining nineteen subjects. LV volumes were assessed from the available contours using Simpson's rule. The quantitative global ventricular function results derived from the automatically detected contours were compared to the results derived from manual contour tracings. The following parameters were included in this comparison: EDV, ESV, EF and LV mass. EDV was defined as the volume of the LV in the first time frame; ESV was defined as the smallest volume of the LV; EF was defined as $100\% \times (EDV-ESV)/EDV$ and LV mass was assessed as the average volume of the myocardium in the ED and ES phases multiplied by the specific density of myocardial tissue (1.05 g/ml). For each parameter the agreement between manual and AAM results was analyzed by computing the mean and standard deviation of the paired differences.

6.3 STATISTICAL ANALYSIS

Values are expressed as mean ± SD. The paired Student t-test was used to assess statistical significance of the differences for each parameter between manual and automated analysis. A p-value<0.05 was considered statistically significant. Parameters obtained by manual and automated analysis were compared using linear regression analysis and by calculating

absolute and relative differences between methods according to the methods of Bland and Altman[10].

Table 6.1. Global ventricular function parameters derived from manually defined contours.

Parameter	Mean	SD
EDV (ml)	161	86
ESV (ml)	104	95
EF (%)	46	19
LVM (g)	126	52

EDV: End-diastolic volume; ESV: End-systolic volume; EF: Ejection fraction; LVM: Left ventricular mass (average of ED and ES values)

6.4 RESULTS

6.4.1 Manual Analysis Results

The number of slices included per study varied between 4 and 9 (average 6.7; SD 1.2). The phase number of ES varied between 6 and 10 (average 7.7; SD 1.3). Endocardial and epicardial contours were manually traced in the slices covering the left ventricle in the phases from ED to ES, resulting in contour tracings in 1010 images. Global function results derived from the manual tracings are summarized in Table 6-1. The interobserver variabilities for EDV were 3.1 ± 4.8% for ESV 2.4 ± 14.8%, for EF 2.9 ± 7.2% and for LVM 2.1±8.7% (Table 6-2). Limits of agreement between two observers using manual analysis for EDV were between −6.5% and +12.7%; for ESV between −27.2% and +32%; for EF between −11.5% and +17.3% and for LVM between −15.3% and +19.5%.

Table 6.2. Interobserver variability for quantification of global LV parameters using manual contour tracing.

Parameter	Obs1-Obs2 (abs)	Obs1-Obs2 (%)
EDV	4.2 ± 7.7 ml	3. ± 4.8%
ESV	0.5 ± 6.7 ml	2.4 ± 14.8%
EF		2.9 ± 7.2%
LVM	2.2 ± 9.0 g	2.1 ± 8.7%

EDV: End-diastolic volume; ESV: End-systolic volume; EF: Ejection fraction; LVM: Left ventricular mass (average of ED and ES values)

6.4.2 AAM contour detection

The twenty available studies were used to generate 20 different AAMM models, in each model the image data of one subject was left out and the corresponding AAM model was used for the automated detection of the left-out subject. Figure 6-1 gives an example of an AAMM model. It shows the average appearance of the systolic contraction in a short-axis MR image, including the first two most significant modes of variation. Figure 6-2B shows an example of automated contour detection results for a mid-ventricular time series of images. The contours detected are very similar to the manually drawn contours for this series shown in Figure 6-2A.

Automated AAMM contour detection was performed successfully in 17 out of twenty exams. In three studies the automated contour detection procedure failed to converge to a correct segmentation result. Visual inspection of these three studies revealed distinct features not seen in any of the other exams:

1. In one exam a bright rim of pericardial fluid (thickness 4-6 mm) was seen at the lateral wall;
2. The second study was a patient with a severely dilated ventricle with a thin ventricular wall and low ejection fraction (EDV 290 ml, average ED wall thickness 5.9 mm, EF 11%)
3. The third study was a patient with severe hypertrophic cardiomyopathy. (LV mass 252 g, local ED septal wall thickness of 26 mm; EF 79%).

Chapter

6

The results of these three studies were excluded from the statistical analysis. For the remaining 17 studies the comparative results between global functions measurements obtained by either manual contour tracing and automated contour detection are listed in Table 6-3. For all the parameters, the differences were found to be statistically non-significant. Linear regression analysis demonstrated an excellent linear correlation between methods with r-values ranging from 0.96–0.99 (p<0.01). Bland-Altman plots comparing the manually obtained and automatically obtained global function parameters are presented in Figure 6-4. In these plots the differences between the methods are displayed as relative errors. There was a very small statistically non-significant bias of the automatically determined parameters. The bias for the global function parameters was never higher than 2%. The 95% limits of agreement for the assessment of global function parameters using AAM contour detection compared to manual analysis were for EDV between −23.8 and +23.3%; for ESV between -43.8% and +47.8%; for EF between 13.0 and +13.3%; and for LVM between -28.5 and +29.9%. In Figure 6-4 a graphical presentation is

given of the differences between automated and manual analysis and observer variabilities using manual analysis.

Computation time for the detection of contours in a complete time sequence of images from ED to ES was less than 3 seconds using a 1GHz PC operating under the Linux operating system. The total computation time for all slices from apex to base was less than 20 seconds per examination.
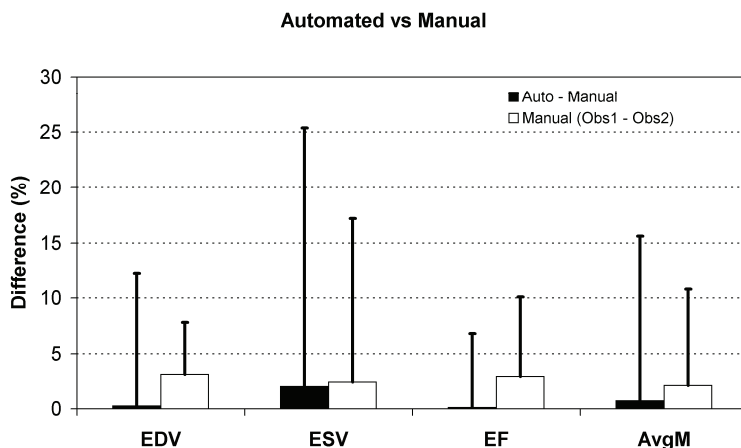
Figure 6-3. Graphical presentation of error of automated contour detection (using manual traced contours as the reference) compared with interobserver variability for manual contour tracing. The error bar shows the standard deviation of the paired differences between measurements for the given global function parameters. Abbreviations: EDV: end-diastolic volume; ESV: end-systolic volume; EF: ejection fraction; LVM: left ventricular mass (average of ED and ES values).

6.5 DISCUSSION

Automated contour detection is a prerequisite for time-efficient quantification of left ventricular function from multi-slice short-axis cine MR imaging studies. Developing of an accurate and robust detection algorithm is a challenging problem due to large variations in patient characteristics and features present in the images. It requires knowledge about the MR image sequence used and knowledge about the anatomy of the heart and neighboring structures. Only trained observers are capable to reliably and reproducibly trace the myocardial contours. It is often helpful to visualize the images in a cine mode to correctly interpret the structures seen in the images. When image information is unreliable or inconclusive, the final judgment is based on a model derived from previous experience.

Table 6-3. Global function results obtained by either manual or automated contour detection. Only those exams are included in which the AAMM contour detection converged to a valid match.

	EDV		ESV		EF		LV mass	
	Manual	Auto	Manual	Auto	Manual	Auto	Manual	Auto
1	63	71	24	31	63	57	57	43
2	171	183	121	118	29	36	147	139
3	142	135	91	82	36	39	102	104
4	81	60	39	23	52	62	90	109
5	109	125	33	43	70	66	142	169
6	209	207	140	154	33	26	145	125
7	77	77	34	34	56	56	62	49
8	72	63	38	30	47	52	47	56
9	112	114	52	43	54	62	105	131
10	173	157	94	85	46	46	123	134
11	143	143	54	62	62	57	136	121
12	300	329	217	281	28	15	217	210
13	160	175	104	115	35	34	98	105
14	146	148	81	69	44	53	121	114
15	127	138	54	53	58	61	120	126
16	127	145	64	80	50	45	96	96
17	418	408	336	361	20	11	225	221
Mean	**155**	**157**	**93**	**98**	**46**	**46**	**120**	**121**
SD	**89**	**91**	**80**	**92**	**14**	**17**	**49**	**49**

EDV: End-diastolic volume; ESV: End-systolic volume; EF: Ejection fraction; LVM: Left ventricular mass (average of ED and ES values)

Chapter

6

The presented AAMM contour detection technique is trained using previously obtained MR imaging studies with expert drawn contours. The generated AAMM contains information about the shape of the left ventricle, the motion and deformation pattern of the left ventricle and the gray value distribution in MR images. By restricting the deformation of the AAMM to statistically defined limits, each deformed AAMM represents a plausible segmentation result. Therefore, the detection algorithm uses similar a-priori knowledge as a human observer. Since the contour detection is based on the minimization of the gray value difference between the actual image data of a whole time-series of images and the deformed representation of the AAMM, the method is relatively insensitive to false edges present in the

images. This is in contrast to other contour detection approaches which rely on local image features such as gray value edges[9,11,12]. An additional advantage of the presented automated method is that it exploits all image information contained in a time-series of images during detection of the contours. This is in accordance with how manual tracing is carried out, since often images are displayed in a cine-mode in order to correctly and consistently interpret the structures seen in the images. Basic physiology dictates that myocardial motion and deformation of the ventricular wall should constitute a time-continuous pattern. The presented algorithm fulfills this constraint since the detected myocardial boundaries are smooth and represent a time-continuous pattern.

The contour detection method was evaluated on clinical cases from various cardiac pathologies. Within the study population the ejection fraction ranged from 11% - 66%; the LV mass ranged from 43 g - 221 g. Nevertheless, automated contour detection provided global ventricular function results comparable to results obtained by manual analysis. No statistically significant differences were found between results obtained by manual and automated analysis. With a processing time of less than 20 seconds for an examination, the contour detection method was proven to be time efficient. Since user interaction was limited to manually defining the ES time frame, observer bias is expected to be very much limited.
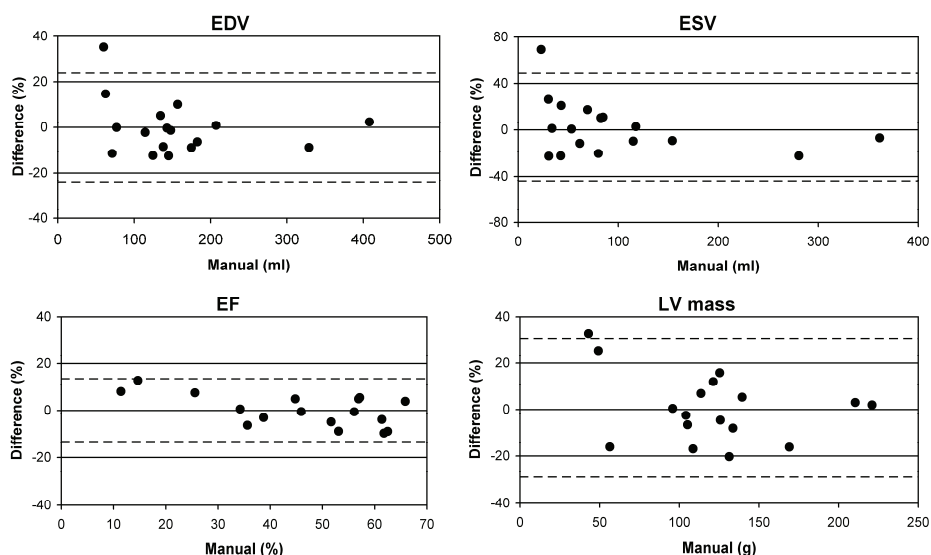
Figure 6-4. Bland-Altman plots for EDV, ESV, EF and left ventricular mass.

6.5.1 Limitations

This study has a number of limitations. In three MR examinations the automated contour detection was unable to detect reliable contours. Inspection of these examinations revealed that in each of these studies distinct features were present not seen in the other studies. Therefore, the correct segmentation for those studies could not be obtained by deforming the AAMM. The occurrence of these failures stresses the importance of using a sufficient number of representative MR studies for training the AAMM. It is assumed that by increasing the number of studies to train the AAMM, the descriptive power of the model increases and the failure rate will be reduced considerably. Currently we have not yet studied the optimal size of the training set and the optimal distribution of various pathologies within the training set.

The current implementation of the method can only be applied to imaging slices where a complete circumference of myocardium is present in all time-frames. In most patients, this condition is not fulfilled for the most basal slice location of the ED frame, since due to through-plane motion during the systolic phase, the myocardial tissue seen in the ED phase may move out of the imaging plane during contraction. Therefore, some imaging sections could not be evaluated using the proposed contour detection method. A possible solution for this problem could be to use a single-phase AAM for the most basal imaging section of the ED phase, as presented by Mitchell at al[7].

Chapter

6

6.5.2 Future studies

To further investigate the strengths and limitations of the presented AAMM contour detection technique and to explore possibilities to improve the method, further studies are required. As already mentioned, it is needed to collect additional clinical MR exams with manually drawn contours to investigate the optimal size for the AAMM training set. Additionally, it is relevant to study whether clinical data of patients with different pathologies should be incorporated in a single model, or whether it proves more successful to have separate models for specific pathologies. A similar question arises when it comes to inclusion of image data acquired with slightly different imaging protocols, or even images obtained from different MR systems in a single model or separate models. In the three cases that were excluded from statistical analysis, distinct features were present explaining why the AAMM contour detection did not perform successfully. However, to understand the sources of the differences between AAMM and manual contour detection in the remaining 17 subjects, further investigation into the sources of these differences are warranted.

Table 6.4. Comparison between manual and automated global function results for those examinations in which the AAMM contour detection converged to a valid match (n=17).

	Auto – Man (abs)	Auto - Man (%)
EDV	-2.9 ± 13.2 ml	-0.3 ± 12.0%
ESV	-5.1 ± 18.9 ml	-2.0 ± 23.4%
EF		0.1 ± 6.7%
LVM	-1.2 ± 14.1 g	-0.7 ± 14.9%

EDV: End-diastolic volume; ESV: End-systolic volume; EF: Ejection fraction; LVM: Left ventricular mass (average of ED and ES values)

6.6 CONCLUSION

A fully automated contour detection method is presented which provides quantitative indices of global function that are comparable to manual analysis. The method can be applied to images acquired with different MR systems and pulse sequences by retraining the AAMM using MR images with expert drawn contours available. Further studies are needed to establish the optimal size and distribution of patients with varying cardiac pathologies in the training set used to build the AAMM.

6.7 REFERENCES

1. Higgins, CB, Sakuma, H. Heart disease: functional evaluation with MR imaging. Radiology 1996; 199:307-315.
2. Semelka RC, Tomei E, Wagner S, Mayo J, Kondo C, Suzuki J, Caputo GR, Higgins CB. Normal left ventricular dimensions and function: Interstudy reproducibility of measurements with cine MR imaging. Radiology. 1990; 174: 763-768.
3. Carr JC, Simonetti O, Bundy J, Li D, Pereles S, Finn JP. Cine MR angiography of the heart with segmented true fast imaging with steady-state precession. Radiology. 2001; 219:828-834.
4. Barkhausen, J, Ruehm, SG, Goyen M, Buck T, Laub G, Debatin JF. MR Evaluation of Ventricular Function: True Fast Imaging with Steady-State Precession versus Fast Low-Angle Shot Cine MR Imaging: Feasibility Study. Radiology. 2001; 219: 264-269.
5. Lee VS, Resnick D, Bundy JM, Simonetti OP, Lee P, Weinreb JC. Cardiac function: MR evaluation in one breath hold with real-time True Fisp imaging with steady-state precession. Radiology. 2002; 222;835-842.
6. Plein S, Bloomer TN, Ridgeway JP, Jones TR, Brainbridge GJ, Sivananthan MU. Steady-state free precession magnetic resonance imaging of the heart: Comparison with segmented K-space gradient-echo imaging. J Magn Reson Imaging. 2001; 14:230-236.
7. Mitchell SC, Lelieveldt BPF, van der Geest RJ, Bosch JG, Reiber JHC, Sonka M. Multistage hybrid active appearance model matching: Segmentation of left and right ventricles in cardiac MR images. IEEE Trans Med Imaging. 2001; 20:415-423.

8. Cootes TF, Beeston C, Edwards GJ, Taylor CJ. A unified framework for atlas matching using active appearance models. Proc.Information Processing in Medical Imaging 1999, Lecture Notes in Computer Science. 1999: 1613:322-333.
9. van der Geest RJ, Buller VGM, Jansen E, Lamb HJ, Baur LHB, van der Wall EE, de Roos A, Reiber JHC. Comparison between manual and automated analysis of left ventricular volume parameters from short axis MR images. J Comput Assist Tomogr. 1997; 21:756-765.
10. Bland JM, Altman DG. Statistical methods for assessing agreement between two methods of clinical measurement. Lancet. 1986; 8:307-310.
11. Baldy C, Doueck P, Croisille P, Magnin IE, Revel D, Amiel M. Automated myocardial edge detection from breath-hold cine-MR images: evaluation of left ventricular volumes and mass. Magn Reson Imaging. 1994; 12:589-598.
12. Lalande A, Legrand L, Walker PM, Guy F, Cottin Y, Roy S, Brunotte F. Automatic detection of left ventricular contours from cardiac cine magnetic resonance imaging using fuzzy logic. Invest Radiol. 1999; 34:211-217.

Chapter

6

CHAPTER

7

**Time continuous tracking and
segmentation of cardiovascular magnetic
resonance images using multi-dimensional
dynamic programming**

ABSTRACT

In this article, we propose a semiautomatic method for time-continuous contour detection in all phases of the cardiac cycle in magnetic resonance sequences. The method is based on multidimensional dynamic programming. After shape parameterization, cost hypercubes are filled with image-feature derived cost function values. Using multidimensional dynamic programming, an optimal path is sought through the sequence of hypercubes. Constraints can be imposed by setting limits to the parameter changes between subsequent hypercubes. Quantitative evaluation was performed on 20 subjects. Average border positioning error over all slices, all phases and all studies, was 1.77 ± 0.57 mm for epicardial and 1.86 ± 0.59 mm for endocardial contours. The average error in end-diastolic and end-systolic volumes over all studies was small: 4.24 ± 4.62 ml and -4.36 ± 4.26 ml, respectively. The average error in ejection fraction was $4.82 \pm 3.01\%$. The reported results compare favorable to the best reported results in recent literature, underlining the potential of this method for application in daily clinical practice.

Chapter

7

7.1 INTRODUCTION

For quantitative analysis of cardiac function, clinical parameters such as end-diastolic (ED) and end-systolic (ES) volume, ejection fraction (EF), and ventricular wall motion are relevant. These parameters are usually estimated from short axis acquisitions consisting of 200 to 300 images. To quantitatively analyze global and regional cardiac function, endo- and epicardial contours of the cardiac left ventricle are required. Recently, several (semi-)automatic methods were developed for detecting the contours of the myocardium. Van Assen et al.[1] and Lötjönen et al.[2] have proposed 3-dimensional (3D) active shape models for automatic segmentation of the human cardiac left ventricle. Kaus et al.[3] have developed deformable models constrained by prior knowledge for automatic segmentation of the left ventricle. Sanchez-Ortiz et al.[4] propose a multi-scale fuzzy clustering-based segmentation algorithm for contour detection in 3D cardiac echocardiographic images. However, many of the proposed methods are suitable for segmentation in end-diastolic and end-systolic phases only, eg, [5-7] Lorenzo-Valdés et al. [8] have developed a 4D probabilistic atlas for the 4D (3D + time) segmentation of the left ventricle based on an expectation maximization method. This method yields segmentations over the full cardiac cycle. However, many manually segmented images are needed for building the atlas, and the structures are segmented independently in each timeframe. Bosch et al.[9] and van der Geest et al.[10] have demonstrated that active appearance motion models are able to yield time-continuous segmentation results for 2D echocardiographic and cardiac magnetic resonance (MR) image sequences, respectively. This method, however, needs to be trained on a training set consisting of several cardiac MR scans with manually annotated contours in all slices and all frames. For a complete overview of recent developments in cardiac segmentation techniques, see the study by Frangi et al.[11].

The mentioned methods here either do not yield time continuous segmentation results over the full cardiac cycle or require extensive manually annotated datasets for training. The goal of this work is to develop a method for time-continuous segmentation of the full cardiac cycle that does not require an extensive training set. To accomplish this, we propose an extension of the well-known 2D dynamic programming to higher dimensions. By expressing a shape with a limited number of parameters, cost hypercubes are constructed, in which each axis represents a parameter range. Each node in a hypercube represents a shape instantiation, and a connective path through a sequence of hypercubes represents a changing shape in a time sequence of images. Constraints

such as temporal or spatial continuity are imposed by setting limits to the parameter changes for each axis between subsequent hypercubes. This makes the method robust in the presence of artifacts or missing image information in individual frames. By including information from all frames in the segmentation, we expect the method to yield more robust and consistent contours in ED and ES frames, which are generally used for deriving the parameters that are needed for quantitative analysis of the cardiac left ventricle. Furthermore, other clinically relevant time-dependent parameters can be derived from the segmented full cycle such as regional wall motion, rate of wall thickening, and peak ejection/filling rate. The proposed method does not require training on large datasets, and prior knowledge on global shape or position dynamics is not needed.

7.2 MATERIALS AND METHODS

7.2.1 Background

Dynamic programming[13] is a method for solving variational problems by successively selecting the locally optimal solutions. The Dijkstra algorithm[13] is one of the best known dynamic programming algorithms and is used for solving shortest path problems, i.e., finding the optimal path from one node to another node in a weighted and directed graph. Each node has an associated weight or cost and the optimal path is the path for which the sum of the costs is minimal. An example is shown in Figure 7-1.

Chapter

7

9	5	0	9	12	8
8	7	9	2	4	4
5	2	5	8	2	2
7	8	4	3	7	5
3	5	8	6	3	3
8	3	2	6	3	8
9	6	8	7	8	4

9	5	0	9	12	8
13	7	9	2	12	12
12	9	7	10	4	14
16	15	11	7	11	9
18	16	g	13	10	12
24	18	15	16	13	18
27	21	23	20	19	17

Figure 7-1. Example of dynamic programming. In the cost matrix on the left, each element represents a node with a given cost, which is derived from an image-related cost function. Using back-propagation, an optimal path is sought from the bottom row to the top row. In the matrix on the right side, the minimal cumulative costs are shown and the optimal path (elements in gray) connects minimal cumulative costs per row, resulting in a globally optimal path.

Dynamic programming (DP) has been used widely in medical image segmentation, but mainly to enforce spatial continuity. For instance, DP has been widely applied in x-ray left ventricular angiography and coronary angiography[14] Xu *et al.*[15] have used DP for automated lung nodule segmentation in computed tomography images. Optimal 2D contours are extracted from all slices using dynamic programming with shape-based constraints. These 2D contours are stacked to obtain 3D surfaces of the nodules. Yamada *et al.*[16] have presented a 2D dynamic programming-based matching method for kidney glomerulus recognition. In this approach, a parameterization of the shape of the glomerulus is made and constraints on the range of parameters are imposed using dynamic programming. Amini *et al.*[17] and Geiger *et al.*[18] have used dynamic programming to find globally optimal solutions to variational problems in energy minimization and to allow direct and natural enforcement of constraints on deformable models.

The approaches described here were all used in static images and typically search for a one-dimensional path through a 2D graph. Little work has been described toward extending DP to higher dimensions. Sonka *et al.*[19] have proposed an extension of 2D dynamic programming by constructing a cost cube from 2 perpendicular edge images, one for each coronary edge. In this graph, each node corresponds to a combination of possible positions of the left and right coronary borders simultaneously. The optimal path through this graph results in a segmentation, in which shape changes in both coronary edges are coupled.

Thedens *et al.*[20] have developed a graph-searching method for finding the optimal surface through a 3D cost cube. Their approach is based on a data transformation of a 3D lattice into an intermediate 2D graph enabling application of traditional graph-searching techniques. To make this approach computationally feasible, they introduce a heuristic search approach potentially yielding suboptimal solutions. Li *et al.*[21] propose a computationally feasible solution for finding a surface through a 3D graph lattice by computing a minimum s-t cut through a 3D-directed graph.

7.2.2 Multidimensional Parametric Dynamic Programming

As mentioned before, higher dimensional extensions of dynamic programming have been described for finding either a surface through a 3D volume or finding a path through a 3D volume. In this work, we extend the classic dynamic programming method to higher dimensions, similar to Sonka's approach[19]. An overview of the general method is represented in Figure 7-2, whereas details on the concrete implementation of two tracking problems are described in the next section. Instead of applying dynamic programming directly to image data, we first define a parametric shape

model, expressing the shape with N parameters. An N-dimensional space can be constructed, in which the axes are spanned by the N parameters. A given shape is represented by a point in this parameter space. Thus, a given combination of the N parameters represents a shape instantiation. By discretizing each parameter axis in a limited parameter range, an N-dimensional hypercube is constructed, which is the N-dimensional equivalent of a cost matrix such as shown in Figure 7-1. For each frame in a time sequence of images, such a cost hypercube is calculated.
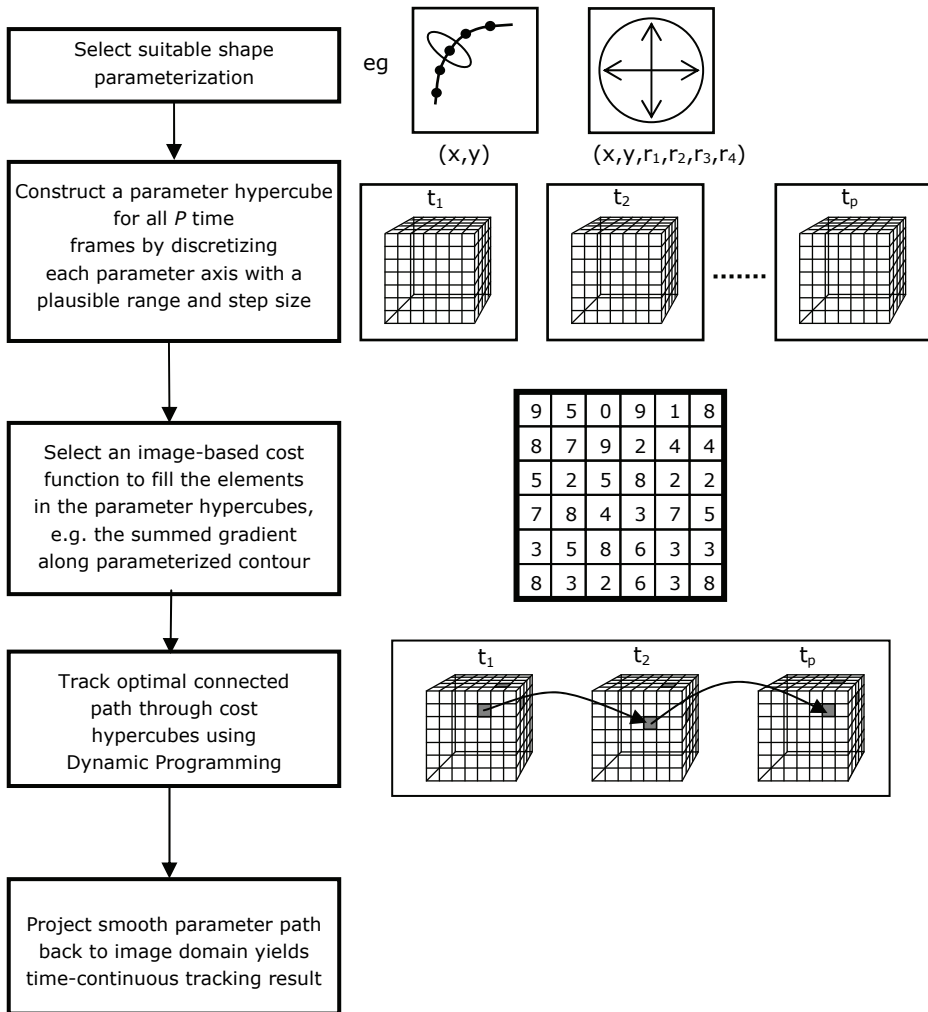
Figure 7-2. General outline of the N-dimensional dynamic programming.

For all possible combinations of the model parameters, i.e., all voxels in the hypercubes, cost values are calculated using a cost function based on image features that express the "goodness of fit" of the model instantiation to the image data. This can be, for instance, the cumulative image gradient along a contour or cross-correlation values between two regions of interest: the choice of the most suitable cost function depends on the application and the selected parameterization. Constraints on temporal or spatial continuity are imposed by setting limits to the allowed parameter changes between subsequent hypercubes for each axis. Subsequently, the optimal path is sought using dynamic programming by connecting the nodes with minimal cost from all hypercubes with each other within these connectivity constraints. This path is a curve in N-dimensional space. The nodes with minimal cost from cost cubes corresponding to different timeframes are connected, in which a connective path through a sequence of hypercubes represents a changing shape in a time sequence (see Figure 7-2). This way, depending on the type of parameterization, spatial and/or temporal continuity can be enforced to ensure smooth motion between frames.

The concrete implementation of the shape parameterization depends on the intended application. In the next section, 2 types of applications with corresponding parameterizations are elaborated.

7.2.3 Validation Studies

To investigate the performance and accuracy of the proposed method, 2 studies were conducted. The first experiment was performed to investigate the accuracy of the DP method in segmentation of short-axis MR images of the cardiac left ventricle and the effect of imposing time-continuity constraints on the robustness of the segmentation results. The second experiment involves a case study to demonstrate the method's efficacy in a higher dimensional case: tracking of the aorta in full-cycle MR images using a 6-dimensional parametric representation.

7.2.4 Data Material

Cardiac MR imaging examinations were performed in 18 cardiac patients and 2 healthy volunteers. The patients experienced several pathologies, including heart failure (n=8), hypertrophic cardiomyopathy (n=4), transplant follow up (n=3), chest pain or angina (n=3).

Short-axis images of the cardiac left ventricle were scanned using the TrueFISP protocol on a 1.5 T Siemens MR system (Sonata; Siemens Medical Systems, Erlangen, Germany) with a resolution of 256 pixels and a field of view ranging from 340 to 420 mm, which resulted in a pixel size varying

between 1.33 and 1.64 mm. The inter-slice gap was 2 mm, the slice thickness was 8 mm, and the following acquisition parameters were used: TR=3.1 ms, TE=1.6 ms, flip angle 55°, and receiver bandwidth 930 Hz/pixel. In these short-axis MR acquisitions, epi-and endocardial contours were drawn by experts in all slices and all phases following the conventions put forward in the study by Danilouchkine *et al.*[23].

To investigate the applicability of the method to higher dimensional tracking problems, an additional velocity-encoded aorta flow scan was acquired in a patient with congenital cardiac abnormalities. Images were acquired in an image plane perpendicular to the ascending aorta on a Philips Gyroscan 1.5 T MR system using a phase-contrast sequence with a VENC of 3 m/s, field of view 300×253 mm, scan matrix 128×108 reconstructed to 256×256 pixels, pixel size 1.17×1.17 mm (reconstructed), and a slice thickness of 8 mm. The full cardiac cycle was imaged in 30 phases, with TR 14 ms, TE 5.2 ms, and flip angle 20° with 2 signal averages.

7.2.5 Short-Axis Cardiac Magnetic Resonance Segmentation

An elaborate quantitative evaluation was performed in a study on full-cycle contour detection in short-axis cardiac MR images. During the cardiac cycle, the endo-and epicardial borders undergo small deformations from frame to frame; this makes the proposed dynamic programming very suitable for imposing constraints on the maximally allowed deformations between frames of the border positions, possibly yielding better segmentation results.

Chapter

7

Using the proposed dynamic programming approach, the optimal contour set for the cardiac cycle can be found as follows (see the flow chart in Figure 7-3 for an overview). After initializing manually by drawing a contour in one phase, the contour is resampled to 32 equiangularly sampled landmarks. Each landmark is parameterized by its coordinates (x,y). (Because the papillary muscles were not included in the manual drawing conform clinical standards, 32 landmarks provided sufficient detail to accurately describe the approximately circular contour shapes.). Each landmark is tracked separately over time by defining a mask in each landmark and a search space around each landmark by setting limits to the displacement parameters dx and dy, which are the allowed shifts for the center of the mask in x and y directions. The mask is positioned onto all allowed positions in the defined search space, and a cross correlation coefficient is calculated for each position with the mask in the reference frame.
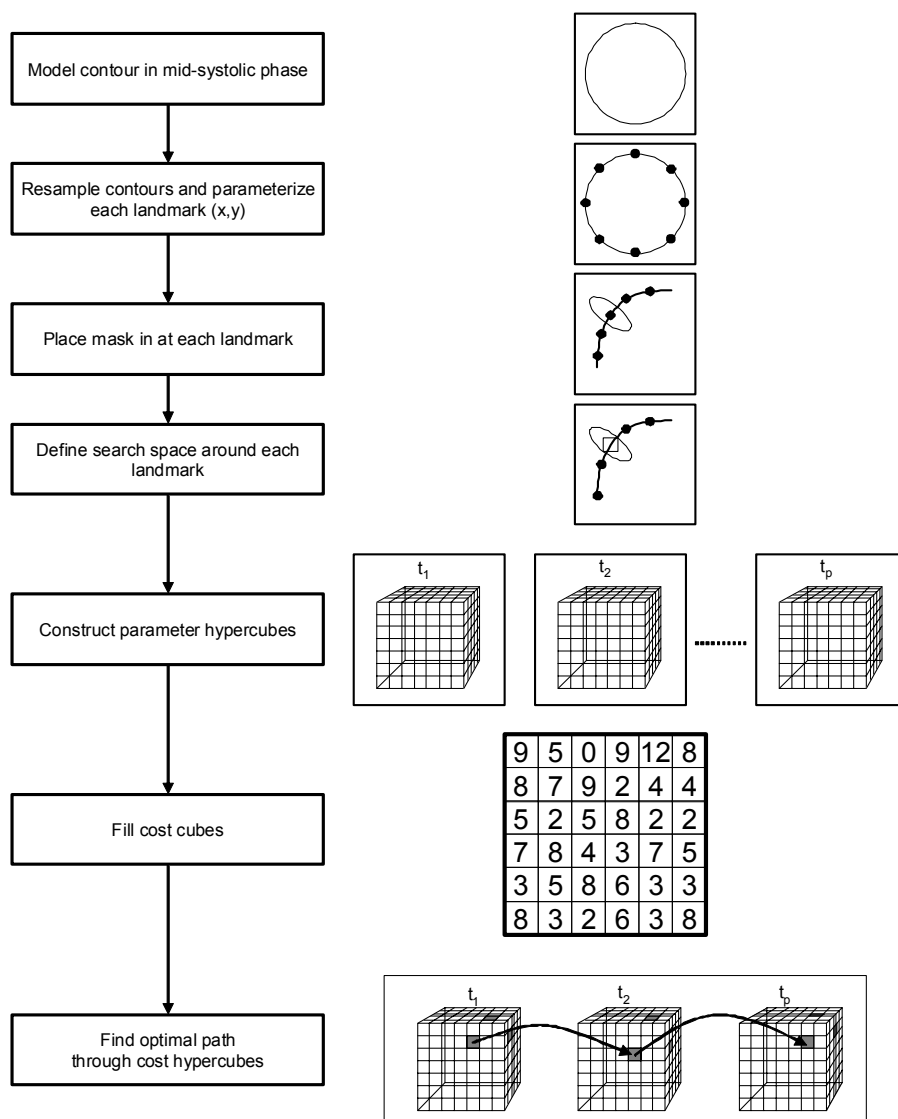
Figure 7-3. Overview of cardiac left ventricle segmentation using multidimensional dynamic programming.

Subsequently, for each landmark, the cost hypercubes are filled with the cost values associated with all shifts of the center of the mask. A 3D search space is created by combining these cost matrices, obtaining a 3D graph. The first and last frames of the graph are the matrices corresponding to the frame with the manually annotated landmarks, ie, the initialization frame. For the cost matrix corresponding to the landmarks in the initialization

frame, the center value is set to zero and all other values are set to high values, as to leave this landmark position unchanged. To find the optimal solution, a connective path is sought through the 3D graph, starting at the zero element in the first slice and crossing each layer of the graph in only one point. Each path through the graph is a possible solution. The total cost of a path is the sum of the costs of all the nodes constituting the path. The optimal solution is the path with minimal total cost. This optimal path yields translation vectors for each landmark with respect to the manually annotated landmark in the reference frame, thus giving the optimal positions for all landmarks over the full cycle.

While searching the optimal path through the graph, hard constraints can be imposed, e.g. a continuity constraint allowing a maximum side step. Because the sampling rate of the full cycle images is sufficiently high, the inter-frame movement of the borders does not exceed 2 pixels. Therefore, a maximal side step of 2 pixels was allowed to obtain time continuity between frames. To assess the effect of the constraints on the side-step parameter, experiments were repeated without side-step constraints. Initialization was performed manually in a mid-systolic phase to enable automatic detection of both end-diastolic and end-systolic frames. This way, an automatic calculation of ejection fraction was possible without introducing a bias toward either the ED or ES frame. In all slices between apex and base, endo-and epicardial contours were available for the initialization frame.

Chapter

7
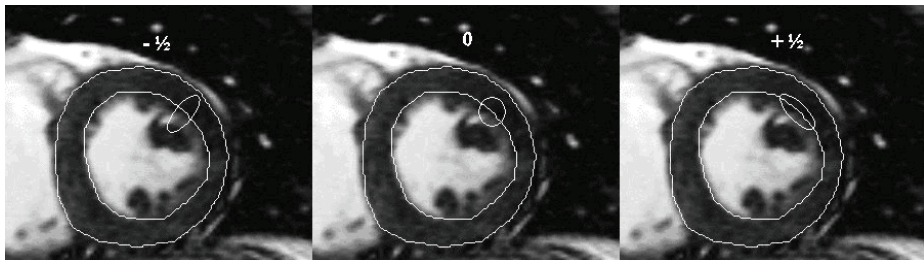
Figure 7-4. Possible settings for the shape of the mask: ellipsoid perpendicular to contour (−½), circular mask (0), and ellipsoid tangent to contour (+½).

7.2.6 Parameter Selection

Several parameters influence the performance of the method, and a brute-force search was performed to systematically select a parameter combination yielding good segmentation results. The parameters involved in the brute force search were:

- Type of cost function: 2 types of cost functions were considered. First, cross correlation of the mask in the current frame with the mask in the reference frame was considered. The cross correlation coefficients were considered as costs, i.e. the higher the correlations, the lower the cost. Second, the sum of absolute gray value differences between the masks was used. Here, a smaller difference corresponds to a lower cost value.
- Mask size: The mask size and shape define the region of interest around each landmark and the amount of information involved in the calculation of the costs. The mask must contain sufficient structure for the cost values to be accurate. However, a too-large mask may include papillary muscles or other structures, which are not present in every frame, potentially resulting in wrong landmark positions in some frames. In the detection of endocardial contours, mask clipping was applied. Because in apical slices the endocardial contours may become very small, the mask size is adapted to half of the radius of the endocardial contour in the initialization frame.
- Mask shape: The shape of the mask is varied from an ellipse tangent to the contour to a circular shape to an ellipse perpendicular to the contour by changing the parameter value between −½ and +½ (see Figure 7-4).
- Physical dimensions of the search space: The parameter limits of the search space were defined by the maximally allowed displacements in x- and y-directions. The size of the search space should be large enough to follow the movement of the myocardium between end-diastolic and end-systolic phases.

The first parameter involves the selection of cost function and is the only intensity feature-dependent choice. The other parameters describe geometric and kinematic properties of the contracting heart. Therefore, we expect the parameter selection to be largely independent of the scanning protocol, therefore generalizing well toward other cardiac MR acquisition protocols not tested here.

7.2.7 Evaluation Indices

To quantify the matching accuracy of the model, the automatically detected contours were compared with the manually defined expert contours on the basis of the point-to-curve border positioning errors, the ED and ES volumes and the EF. The point-to-curve errors were defined as the shortest distance between an automatically detected landmark and the manually drawn contour, i.e. the distance along the normal to the manually drawn curve. Average and maximum border positioning errors were measured. The ED and ES volumes were calculated as follows. In each slice, the

surface of the endocardial border, i.e. the blood pool was calculated and multiplied with the slice thickness. The sum of all slice volumes was calculated to determine the 3D volume of the cardiac left ventricle. Using the volumes in ED and ES phases of the cardiac cycle, the EF was calculated as follows:

$$EF = \frac{V_{ED} - V_{ES}}{V_{ED}}$$
(7.1)

where EF is the ejection fraction, V_{ED} the cardiac left ventricular volume in end-diastolic phase, and V_{ES} the volume in end-systolic phase.

Paired-sample t-tests were performed to determine if the errors in border positioning, volumes, and ejection fractions were significant. P values smaller than 0.05 were considered significant.
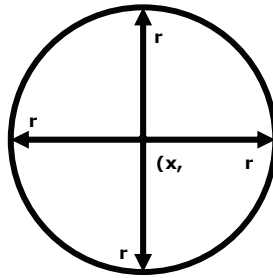
Figure 7-5. Six-dimensional parameterization of a region around the aorta with center coordinates (x,y) and 4 radii r1,r2, r3, r4.

7.2.8 Aorta Tracking

An additional experiment was performed to investigate the potential of multidimensional dynamic programming applied to higher dimensional cases. The area of the aorta was tracked over time to measure the flow[22] in images of a specific slice of the aorta, which are used to measure flow volume. In a time sequence of images, translation and deformation of the aorta occurs. To this end, the shape of the aorta was parameterized with 6 parameters (center coordinates [x,y] and 4 radii r_1–r_4) as shown in Figure 7-5. In sequential images, the center coordinates were varied as well as the 4 radii. A spline was fitted to the end points of the radii to obtain an ellipse. With this parameterization, a 6-dimensional cost hypercube was constructed. The costs associated with each instantiation of the aorta shape were defined as the cumulative image gradient along the model contour. Ranges were defined for all combinations of the mentioned parameters, ie,

all shape instantiations. The associated costs were calculated and stored in the corresponding positions in the hypercube. Next, using conventional backtracking, an optimal path with minimal total cost within time-continuity constraints was sought through the hypercubes. The optimal path yielded translation vectors for the center coordinates and deformation vectors for the radii with respect to the reference frame. The results of the experiments were evaluated visually.

Table 7-1. Optimal settings for parameters obtained with a brute-force search *

Contour	dx (pixels)	dy (pixels)	Mask size (pixels)	Mask shape
Endocardial	7	7	19	-½
Epicardial	4	4	15	0

* Mask shape 0 corresponds to a circular mask (see Figure 7-3) and -½ corresponds to ellipsoid. Results for endocardial and epicardial contour are shown.

7.3 RESULTS

7.3.1 Parameter Settings

The parameters computed in the parameter selection process are given in Table 7-1. For detection of both endocardial and epicardial contours, the cross correlation-based cost function was found to give more accurate results than the cost function based on the sum of absolute differences.

7.3.2 Segmentation Results

Epicardial and endocardial contours were detected separately. With parameter settings as shown in Table 7-1, the average border positioning error (BPE) over all slices, all phases, and all studies was 1.77±0.57 mm (average maximum BPE was 5.21 mm) for epicardial contours and 1.86±0.59 mm (average maximum BPE was 4.51 mm) for endocardial contours. In Table 7-2, the errors in volumes and ejection fractions are shown. Figures 7-6 shows Bland-Altman plots for ED and ES volumes and ejection fractions. Parameters of the regression fits are given in Table 7-3.

Figure 7-7 shows that if no time-continuity constraints are imposed, the segmentations deteriorate and large inter-frame discontinuities and border positioning errors are introduced. As can be seen from the bottom row of Figure 7-7, single landmarks can make large excursions and lock onto false positions, resulting in bad segmentation results.

Table 7-2. Average manual ED and ES volumes and ejection fractions, with average errors made by an automatic dynamic programming-based method

	Average manual	Average error	P
ED volume (ml)	171.68 ± 91.10	4.24 ± 4.62	6.14 E-4
ES volume (ml)	103.96 ± 95.96	-4.36 ± 4.26	2.05 E-4
Ejection fraction (%)	47.73 ± 19.20	4.82 ± 3.01	8.48 E-7

Typical computation times for full-cycle segmentation of a 3D short-axis cardiac MR scan (8-12 slices, 20-25 frames) amounted to approximately 4 minutes on a desktop PC with an AMD Athlon 1.8 GHz processor.
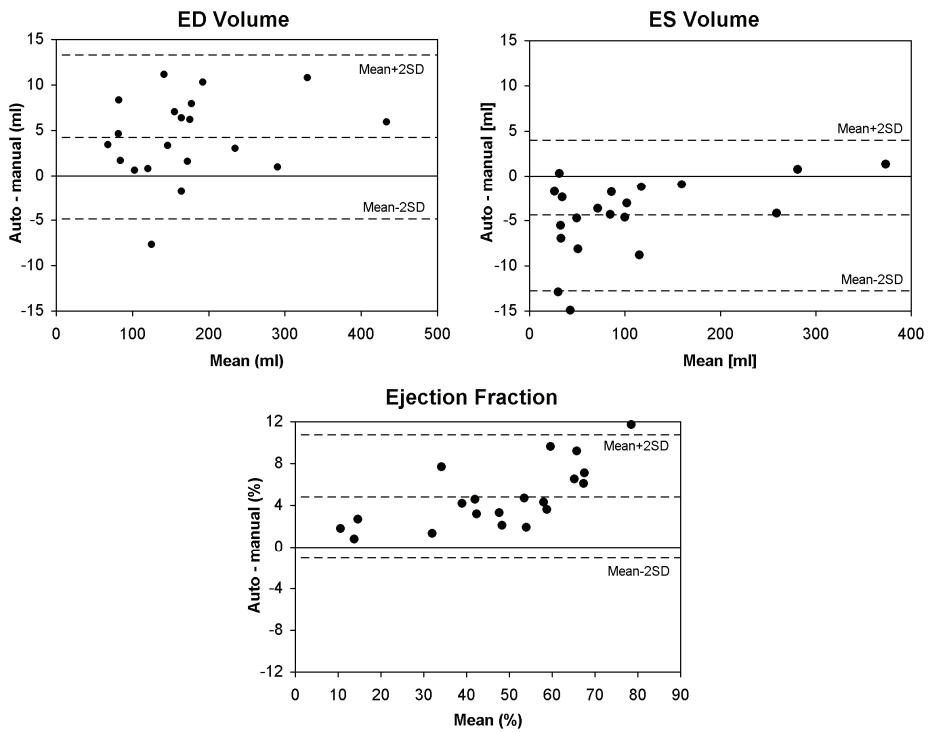
Figure 7-6. Bland-Altman plot for end-diastolic volumes (top left), end-systolic volumes (top right) and ejection fraction (bottom).

7.3.3 Tracking Results

Figure 7-8 shows the result of tracking the aorta in 30 sequential timeframes using a shape parameterization with 4 radii and 2 center coordinates.

Table 7-3. Equations of regression fits for ED and ES volumes and ejection fractions

	Regression fit	R^2
ED volumes	y = 0.99x – 2.21	0.998
ES volumes	y = 0.98x – 6.55	0.998
Ejection fractions	y = 0.89x – 0.34	0.984

7.4 DISCUSSION

A dynamic programming-based method for time-continuous segmentation of endo-and epicardial contours was presented. Conventional 2D dynamic programming was extended to higher dimensions and applied to 2 substantially different tracking and segmentation problems to illustrate the method's performance in multiple dimensions.

In the quantitative evaluation, segmentations were performed in 20 studies in all phases and all slices. Contour detection was successful in all included imaging slices and the average BPE was very good (1.86 mm and 1.77 mm for endo-and epicardial BPE, which corresponds to approximately 1 pixel), although slightly less accurate as interobserver BPE reported in the study by van Assen et al.[1] (1.27 mm and 1.14 mm for endo-and epicardial BPE, respectively). Lötjönen et al.[2] report an average segmentation error of 2.57 mm using the probabilistic atlas based method. The method presented by Kaus et al.[3] has a mean deviation from manual segmentations of 2.45 mm in end-diastolic phase and 2.84 mm in end-systolic phase, whereas van Assen et al. report 2.24 mm and 2.84 mm errors for endo-and epicardium, respectively. Lorenzo-Valdés et al.[8] report an average segmentation error of 2.21 mm for the 3 middle slices of the left ventricle over all timeframes. Also, the maximum BPE for endo-and epicardial contours (4.51 mm and 5.21 mm, respectively) compares highly favorably to the other automated methods (11–15 pixels as reported in the studies by van Assen et al.[1] and Kaus et al.[3]) and compares well to interobserver maximum errors reported in the study by van Assen et al.[1] (4.34 and 3.93 maximum BPE for endo-and epicardial contours, respectively). Therefore, we can conclude that border positioning errors presented in this article compare favorable to these other results reported in recent literature and approach interobserver variabilities resulting from manual contour drawing. Of these methods, only Lorenzo-Valdes reports

full-cycle contour detection. The other approaches report results in ED and ES phases only. An important criterion for any automated border detection method for cardiac MR images is that if morphology is important, accurate regional measurements require the border detection to yield errors at least as good as the interobserver variability resulting from manual contour drawing, because a small error can already have a significant impact on regional measurements such as wall thickness and wall thickening. Of the algorithms compared here, the proposed method best approaches this interobserver BPE.
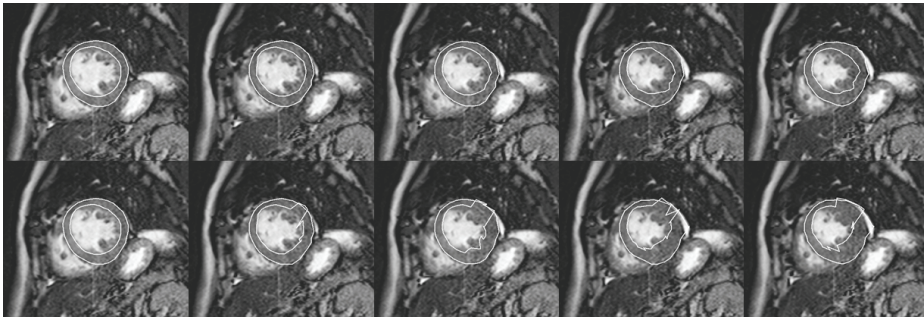
Figure 7-7. The top row shows segmentations obtained with temporal continuity constraint in 5 successive frames. The first frame is the mid-systolic phase which was used for manual initialization. In the bottom row, the same frames segmented without imposing temporal continuity constraints are shown.

Chapter

7

The automatically determined end-diastolic and end-systolic volumes showed near-perfect correlations with the volumes derived from manual contours. Also, the ejection fractions of automatically segmented and manually drawn studies correlated very well (see Table 7-3). This is a direct consequence of the small border-positioning errors, but although the volume errors are small, they are statistically significant (P<0.05). Bland-Altman plots reveal a slight systematic underestimation of the ED volumes and a slight systematic overestimation of the ES volumes. This, of course, has a negative influence on the ejection fraction estimates. The systematic over-and underestimations are most probably caused by a bias toward the reference frame. Currently, a rectangular search space around the landmarks is used (dx, dy). Defining a different search space shape, eg, allowing more radial movement, might resolve the systematic bias. The errors, however, are small and not clinically relevant; they are in the same range as interobserver variations in ventricular volumes and ejection fractions[23], comparing measurements from manually drawn contours from different observers.

As can be seen in Table 7-1, a larger search space and mask need to be defined for endocardial contour detection than for epicardial contour detection. Also, the border positioning errors are slightly larger for endocardial contours. This is caused by the fact that during the cardiac cycle, the movement of the endocardial border has larger amplitude than the epicardial border. Therefore, the texture in the masks used for tracking the endocardial borders demonstrates relatively more changes between end-diastolic and end-systolic phases. Also, the fusion of the papillary muscles with the myocardium in end-systolic phases substantially changes the mask texture. These effects deteriorate the cross correlation values, i.e. the cost function outcomes.
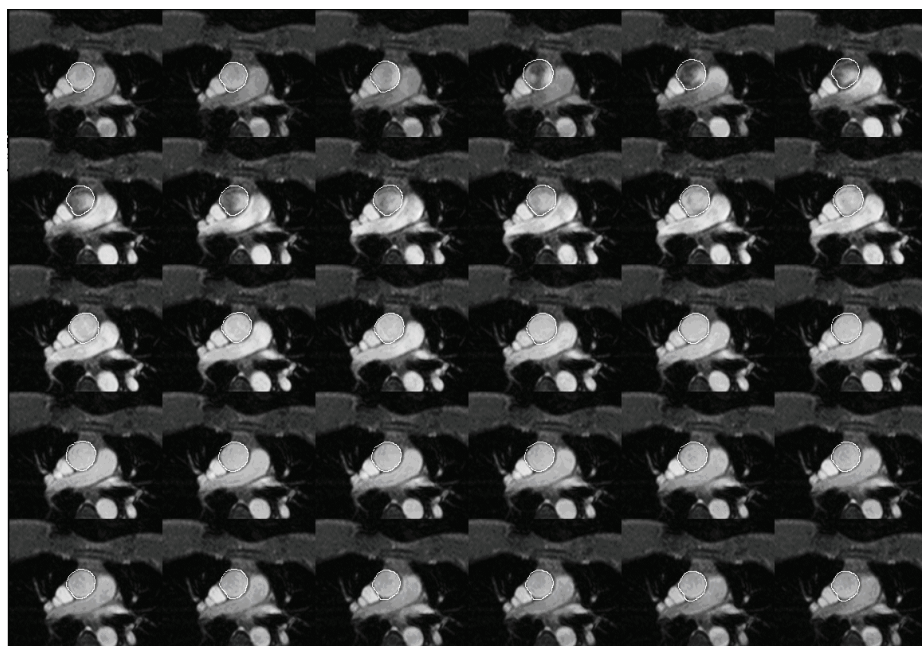
Figure 7-8. Sequential timeframes in an aortic flow scan, in which the motion and deformation aorta is tracked over the cardiac cycle. Note the smooth transitions between frames, which is a result of the imposed time continuity.

The proposed method may possibly be further improved, eg, by blurring the images before contour detection. Blurring the images reduces noise and better cross correlation values can be obtained. Another improvement might be smoothing of the contours after detection. Currently, all landmarks are detected independently and are connected with each other by straight lines. This in general gives a slight underestimation of the volumes. The underestimation is larger in basal slices and also in

end-diastolic images, because the sampling of the contours is less dense in these images. Smoothing the contours after connecting the landmarks might give a better estimate of the volumes, although landmark positions remain unchanged.

Experiments have shown that adding a time constraint to the conventional dynamic programming approach substantially improved the segmentation results. Without this constraint, single landmarks showed large inter-frame displacements, which led to locking on false edges. Imposing a maximal inter-frame displacement by means of a time constraint resolved these errors. In the current approach, endo-and epicardial contours are detected separately. However, the locations of both contours are strongly correlated. Therefore, combining both contours and detecting them simultaneously might yield still more robust results.

For each landmark, separate cost matrices are calculated for each timeframe, and the optimal positions of the landmarks are determined independently from its neighboring landmarks. In some cases, this leads to crossing landmarks and spatial discontinuities in the segmentations (see Figure 7-9). These artifacts may be resolved by following the approach in the study by Thedens *et al.*[20] and coupling neighboring landmarks to each other, preventing landmarks from crossing each other. This way, not only time-continuous, but also spatially continuous segmentations can be obtained, which may also lead to a further improvement of the border positioning errors, the volume estimations, and ejection fraction calculations.

Chapter

7
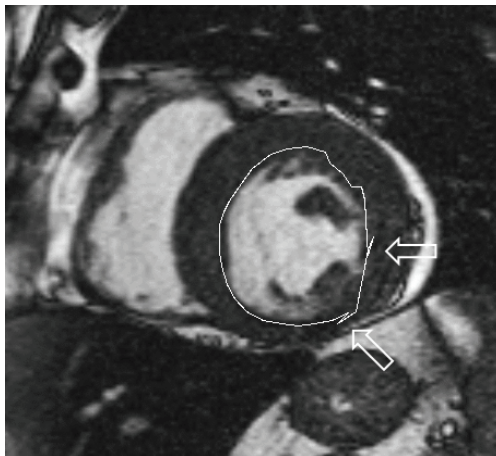
Figure 7-9. Spatial discontinuity caused by crossing landmarks in endocardial contour.

In our current approach, segmentations were performed on a slice-per-slice basis. Time-continuous segmentation results can be obtained for each slice in this manner. However, inter-slice continuity is not guaranteed. By coupling landmarks from neighboring slices with the proposed approach, inter-slice continuity may be obtained as well.

The parameter selection procedure involved systematically deriving a good parameter combination, in which most of the parameters were related to geometry and cardiac kinematics, which are independent of the applied scanning protocol. Highest accuracy was obtained with the presented values for the parameters in the tested image sets. However, we expect similar performance in other MR datasets and protocols as a result of the protocol independence of the tuned parameters.

The aorta tracking experiments have demonstrated the power of the proposed method in a 6-dimensional case study. The proposed approach was used for automatic tracking of the aorta in a time sequence of images, and visual inspection showed that a time-continuous result was obtained. This example showed that there are no theoretical obstacles for the expansion of the proposed method to high dimensions; however, further evaluation is required to quantify the performance of dynamic programming in such higher-dimensional cases.

The main limitation of the proposed method is its computational complexity, which increases exponentially with the number of parameter dimensions. Finding the optimal path through cost hypercubes is fast; however, filling the cost hypercubes may become time-consuming. This obviously depends on the dimension of the hypercubes and the type of cost function, e.g. sum of absolute differences, cross-correlation values, and so on. In the experiments that were performed, typical computing times in the order of 3 to 5 minutes per study (on average, 20 phases and 10 slices) were found. Because the analysis is performed offline and with increasing computer power, this does not impose a major limitation on clinical applicability. In addition, by pruning the search space, substantial additional performance gains can be achieved.

7.5 CONCLUSION

In conclusion, the proposed method has shown great potential in tracking and segmentation of cardiac MR time sequences. The multidimensional dynamic programming allows for direct and natural enforcement of constraints, e.g, shape-based constraints or time-continuity constraints. It is not iterative and therefore it is exact and stable. With dynamic programming, global optimality of the solution is ensured and multidimensional dynamic programming enables detection of time evolution

and full-cycle time-continuous segmentation in a series of images. The reported results compare favorably to the best-reported results in recent literature, underlining the potential of this method for application in daily clinical practice.

7.6 REFERENCES

1. van Assen HC, Danilouchkine MG, Frangi AF, et al. SPASM: segmentation of sparse and arbitrarily oriented cardiac MRI data using a 3D ASM. Proceedings FIMH 2005, Lecture Notes in Computer Science. 2005; 3504:33-43.
2. Lötjönen J, Kivistö S, Koikkalainen J, et al. Statistical shape model of atria, ventricles and epicardium from short-and long-axis MR images. Medical Image Analysis. 2004; 8:371–386.
3. Kaus MR, Von Berg J, Weese J, et al. Automated segmentation of the left ventricle in cardiac MRI. Medical Image Analysis. 2004; 8:245–254.
4. Sanchez-Ortiz GI, Wright GJT, Clarke N, et al. Automated 3-D echocardiography analysis compared with manual delineations and SPECT MUGA. IEEE Transactions on Medical Imaging. 2002; 21:1069-1074.
5. Stegmann MB, Pedersen D. Bi-temporal 3D active appearance models with applications to unsupervised ejection fraction estimation. In: Sonka M, Fitzpatrick JM, eds. Proceedings SPIE Vol. 5747, Medical Imaging 2005: Image Processing.
6. Mitchell SC, Bosch JG, Lelieveldt BPF, et al. 3-D active appearance models: segmentation of cardiac MR and ultrasound images. IEEE Transactions on Medical Imaging. 2002; 21:1167–1177.
7. Uzümcü M, Van der Geest RJ, Sonka M, et al. Multi-view active appearance models for simultaneous segmentation of cardiac 2-and 4-chamber long axis MR images. Invest Radiol. 2005; 40:195-203.
8. Lorenzo-Valdés M, Sanchez-Ortiz GI, Elkington AG, et al. Segmentation of 4D cardiac MR images using a probabilistic atlas and the EM algorithm. Medical Images Analysis. 2004; 8:255–265.
9. Bosch JG, Mitchell SC, Lelieveldt BPF, et al. Automatic segmentation of echocardiographic sequences by active appearance motion models. IEEE Transactions on Medical Imaging. 2002; 21:1374 –1383.
10. Van der Geest RJ, Lelieveldt BPF, Angelié E, et al. Evaluation of a new method for automated detection of left ventricular contours in time series of magnetic resonance images using an active appearance motion model. J Cardiovasc Magn Reson. 2004; 6:609 – 617.
11. Frangi AF, Niessen WJ, Viergever MA. Three-dimensional modeling for functional analysis of cardiac images, a review. IEEE Transactions on Medical Imaging. 2001; 20:2–25.
12. Bellman R, Dreyfus S. Applied Dynamic Programming. Princeton, NJ: Princeton University Press; 1962.
13. Dijkstra EW. A note on two problems in connexion with graphs. Numerische Matematik. 1959; 1:269-271.
14. Sonka M, Fitzpatrick JM. Handbook of Medical Imaging: Medical Image Processing and Analysis. Bellingham, WA: SPIE Press; 2000; 2:711-794.
15. Xu N, Ahuja N, Bansal R. Automated lung nodule segmentation using dynamic programming and EM based classification. In: Sonka M, Fitzpatrick JM, eds. Proc. SPIE, Medical Imaging 2002: Image Processing. 2002; 4684:666-676.
16. Yamada H, Merritt C, Kasvand T. Recognition of kidney glomerulus by dynamic programming matching method. IEEE Transactions on Pattern Analysis and Machine Intelligence. 1988; 10:731-737.

Chapter

7

17. Amini AA, Weymouth TE, Jain RC. Using dynamic programming for solving variational problems in vision. IEEE Transactions on Pattern Analysis and Machine Intelligence. 1990; 12:855-867.
18. Geiger D, Gupta A, Costa LA, et al. Dynamic programming for detecting, tracking, and matching deformable contours. IEEE Transactions on Pattern Analysis and Machine Intelligence. 1995; 17:294-302.
19. Sonka M, Winniford MD, Collins SM. Robust simultaneous detection of coronary borders in complex images. IEEE Transactions on Medical Imaging. 1995; 14:151-161.
20. Thedens DR, Skorton DJ, Fleagle SR. Methods of graph searching for border detection in image sequences with applications to cardiac magnetic resonance imaging. IEEE Transactions on Medical Imaging. 1995; 14:42-55.
21. Li K, Wu X, Chen DZ, et al. Efficient optimal surface detection: theory, implementation and experimental validation. In: Sonka M, Fitzpatrick JM, eds. Proc. SPIE, Medical Imaging 2004: Image Processing. 2004; 5370:620-627.
22. Kondo C, Caputo GR, Semelka R, et al. Right and left ventricular stroke volume measurements with velocity-encoded cine MR imaging: in vitro and in vivo validation. AJR Am J Roentgenol. 1991; 157:9-16.
23. Danilouchkine MG, Westenberg JJM, de Roos A, et al. Operator Induced variability in cardiovascular MR: left ventricular measurements and their reproducibility. J Cardiovasc Magn Reson. 2005; 7:447-457

CHAPTER

8

Automatic method for the optimization of left ventricular segmentation in cardiovascular magnetic resonance images

ABSTRACT

Automatic segmentation of the left ventricular (LV) myocardial borders in cardiovascular MR (CMR) images allows a significant speed-up of the procedure of quantifying LV function, and improves its reproducibility. The automated boundary delineation is usually based on a set of parameters that define the algorithms. Since the automatic segmentation algorithms are usually sensitive to the image quality and frequently depend heavily on the acquisition protocol, optimizing the parameters of the algorithm for such different protocols may be necessary to obtain optimal results. In other words, using a default set of parameters may be far from optimal for different scanners or protocols. For the MASS-software, for example, this means that a total of 14 parameters need to be optimized. This optimization is a difficult and labor-intensive process. To be able to more consistently and rapidly tune the parameters, an automated optimization system would be extremely desirable. In this paper we propose such an approach, which is based on genetic algorithms (Gas). The GA is an unsupervised iterative tool that generates new sets of parameters and converges toward an optimal set. We implemented and compared two different types of the genetic algorithms: a simple GA (SGA) and a steady state GA (2SGA). The difference between these two algorithms lies in the characteristics of the generated populations: "non-overlapping populations" and "overlapping populations," respectively "non-overlapping" population means that the two populations are disjoint, and "overlapping" means that the best parameters found in the previous generation are included in the present population. The performance of both algorithms was evaluated on twenty routinely obtained short-axis examinations: eleven examinations acquired with a steady-state free precession pulse sequence, and nine examinations with a gradient echo pulse sequenced. The optimal parameters obtained with the GAs were used for the LV myocardial border delineation. Finally, the automatically outlined contours were compared to the gold standard—manually drawn contours by experts. The result of the comparison was expressed as a degree of similarity after a processing time of less than 72 h to a 59.5% of degree of similarity for SGA and a 66.7% of degree of similarity for 2SGA. In conclusion, genetic algorithms are very suitable to automatically tune the parameters of a border detection algorithm. Based on our data, the 2SGA was more suitable than the SGA method. This approach can be generalized to other optimization problems in medical image processing.

Chapter

8

8.1 INTRODUCTION

Cardiac magnetic resonance (MR) imaging is playing an increasingly important role for anatomical and functional assessment of the cardiovascular system. An accurate delineation of the endocardial and epicardial boundaries is important to quantify the left ventricular (LV) dimensions. Manual segmentation requires expert knowledge and is a time consuming procedure, which limits the routine clinical use of cardiovascular MR. Moreover, the manual segmentation is observer dependent and therefore is associated with considerable inter- and intra-observer variability. Automated and semi-automated contour detection techniques have been developed in order to overcome the disadvantages of manual contour drawing, but the robustness of the currently available contour detection algorithms is still not optimal for routine use. At our laboratory, we have developed a cardiac MRI analysis software package, MASS, which includes automated contour detection[1]. A major challenge when designing and implementing a reliable automated contour detection algorithm is to deal with the large variations in image characteristics due to differences in MR pulse sequences used, the usage of different receiver coils and differences between MR scanners from different vendors. Consequently, for optimal performance, the automated segmentation method needs to be optimized for a specific type of acquisition procedure.

To date, the commonly used method of optimizing an automatic segmentation algorithm is to manually tune the parameters of the segmentation algorithm until accurate results are reached. Generally, numerous iterations are required to obtain the optimal segmentation result, and there is no guarantee that the optimal result will be achieved. To deduce the optimal value for a specific parameter, the underlying physical or geometrical constraints must be taken into consideration. But some parameters are less intuitive and therefore hard to find by means of ad-hoc search. Moreover, segmentation algorithms are often complex and the segmentation parameters are dependent upon each other (all the parameters have to be optimized together and not by means of a step-by-step analysis) and as a consequence hard to optimize manually on a trial and error basis[2].

To automate the optimization, a brute-force approach could be utilized. By such approach, all possible permutations of parameters would be taken into consideration. Taking the complexity of segmentation algorithms and the number of parameters to be optimized into consideration, this approach appears to be computationally expensive and infeasible.

The aim of this work was to design an automated optimization system based on unsupervised tools that can generate new parameter sets in order to automatically tune an automated contour detection algorithm. Previous papers presented an adaptation of the Genetic Algorithm (GA), the Parallel Genetic Algorithm (PGA), as an intelligent parameter optimization tool. The PGA has already proved to be an effective method to optimize dynamic model-based contours[5] and to improve marker placement[6]. Consequently, the main question raised in this work was to study the ability of the GA to solve the optimization problem faced in our border detection algorithms. A number of optimization techniques exist already and differ in their capability to find a global optimum, which is often hidden among local optima, and by their speed of convergence towards the global optimum[,8,9]. These algorithms are employed for finding a global optimal solution in a high-dimensional search space. Finding a global optimal solution is often difficult due to noise or perturbations, and GA-based methods have shown to be capable of finding a robust solution[8]. Therefore, GAs appear to be valuable candidates for the implementation of an optimization method.

Because the segmentation performance varies according to the pulse sequence used, we assumed that the optimized parameter setting for the segmentation of images acquired with different pulse sequences should be different too. In order to test the ability of a GA to solve the optimization problem faced, we compared the optimized parameter settings found using a GA on different images acquired with different pulse sequences.

The number of GAs existing in the literature makes the choice of the best optimization algorithm difficult. Thus, the second question raised in this paper was therefore which GA should be used in the optimization faced. Since most of the GAs can be divided into two different classes, two GAs were tested. The one using overlapping populations, the steady state GA (2SGA)[11], and the other one using non-overlapping populations, the so-called simple GA (SGA).

Chapter

8

8.2 MATERIALS

8.2.1 Material

For the reason of limiting the computation time required, and because this work aimed at examining the ability of the GA to solve our optimization problem, the study population was limited to 20 patients with a history of cardiovascular disease with a wide range of ejection fraction (4-78%). The study material consisted of eleven MR Steady-State Free Processing (SSFP, TR=3.2 ms, TE=1.6 ms, flip angle=60°) and nine MR Gradient Echo (GRE, TR=50 ms TE=4.8 ms, flip angle=20°) (three females and 17 males with a

mean age of 63 years) short axis examinations of the cardiac LV. MR images were acquired on a 1.5T MR system (Siemens Sonata). A temporal resolution or phase interval varying between 46 and 50 ms was chosen to ensure that the end-systolic phase was properly defined. The images were acquired with a FOV of 400 mm and reconstructed to a 256×256 image matrix. Slice thickness varied between 8 and 10 mm and the number of slices varied between 10 and 19; the number of cardiac phases between 13 and 26 depending on the heart rate. Image analysis was limited to the end-diastolic (ED) and end-systolic (ES) phases. Endocardial contours were drawn by an expert using MASS version 5.1 following a predefined protocol as described previously:

1. Window and level settings were standardized and kept unchanged for the entire study;
2. ED and ES phases were chosen after viewing the images in the movie mode
3. The uppermost slice showing more than 50% of the circumference of the ventricular myocardium was defined as the basal slice;
4. Papillary muscle and trabeculations were treated as being a part of the blood pool to be able to assess the wall thickness and wall thickening of the cardiovascular system.

8.3 METHODS

In this paper we tested whether the GA was suitable to find the optimal setting of the segmentation parameters used in MASS software package. We focused only on the optimization of the algorithm for automated detection of the endocardial contours of the cardiac LV.

The GA is an unsupervised tool that can generate new settings of segmentation parameters based on a sample of initial parameters sets. Each parameter set is called an individual. The GA starts with randomly chosen individuals, called population, including a fixed number of individuals. Next, the GA creates a new population of individuals by mutating and mating the best individuals from the previous population and producing new offspring. The value of each parameter is encoded in a binary string and the mutation operator flips the bits with a given probability (p_{mut})[11]. For instance, for a probability of twenty percent, 20% of the zeroes and ones in the binary string will be mutated in ones and zeroes, respectively. Then the crossover operator (with probability p_{cross}) is applied to the string population for generating new individual from two binary strings[11,12].

The first step of this study was to evaluate whether or not this tool could solve the optimization of the segmentation algorithm used in MASS. Next, we compared the optimization result of two different GAs in order to define the optimization tool to use in the scope of our study.
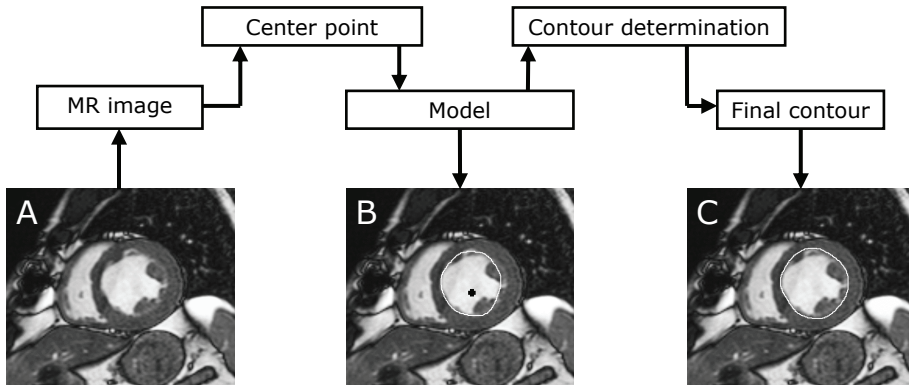
Figure 8-1. Flow chart illustrating the contour detection process and the inter-dependency of different steps and thus the segmentation parameters to optimize (A: original short-axis SSFP image; B center point and detected endocardial model contour; C: final contour).

8.3.1 GA's capability to solve the MASS optimization problem

Segmentation parameters
The automated contour detection algorithm implemented in MASS was described previously. It follows a three-step procedure as illustrated in Figure 8-1. To determine the middle point of the left ventricle, a Hough transform is applied to the images, resulting in an identically sized parameter image, with high values near the center point of the LV having a radius within a certain range defined by two parameters: minimum and maximum endocardial radius. Then, the model determination step consists of a first segmentation of the blood pool area using an adaptive thresholding technique. Two different thresholding techniques can be used. The first one consists by generating radial scan lines emanating from the detected center and collecting for each scan the gray value of the pixel with the highest edge value within the minimum and maximum radii. The second one is based on generating iso-intensity contours surrounding the center point of the LV and considering the one with the highest edge strength. The choice of which thresholding method to use is made by one parameter. The mean gray value of these edge pixels weighted by a percentage parameter is then defined as the threshold value. Next, a smooth convex hull surrounding the blood pool area is determined. A total

Chapter

8

of four parameters (the knowledge about the LV geometry, the choice of the thresholding technique to use and a weighting percentage) are required during the model determination.

In a third step, the final contour is obtained by refining the model contour using two successive minimal cost edge detection techniques[13]. Given the previous model contour, the image data in a certain neighborhood around the model is spatially transformed into a rectangular array (so-called scan array), the width of which can vary. Then all the points in this array are transformed into a cost matrix. The cost matrix is obtained using a derivative operation equivalent in a computational point of view to a convolution with a kernel that has to be optimized. The cost values included in the matrix reflect the probability that the corresponding point in the image is part of the desired contour. All possible paths through the matrix are evaluated for their total accumulated cost. Some constraints, such as the distance to look for a neighbor, or the distance towards the center of the matrix, or the orientation of the path are added to weigh the calculation of the minimal cost path. Five parameters had to be optimized for each minimal cost algorithm, resulting in a total of ten parameters optimizing in this latest step.

Since the output of each step is input for the following step in the algorithm, the optimal parameter settings for an individual step are dependent upon the parameter setting of the preceding steps. All the segmentation parameters are dependent upon the image characteristics. The differences in the pulse sequences cause discrepancies in, e.g., the brightness of the blood pool and the sharpness of the contours, which are crucial for the segmentation. Therefore, it is necessary to optimize these segmentation parameters for each specific MR pulse-sequence.

Criterion to be optimized

Optimizing the automated contour detection algorithm requires a criterion to be optimized. The criterion considered in the optimization is called the fitness value and is an indicator of the match between the automatically detected contour and a manually drawn contour (accepted as a gold standard). The aim of the fitness function is to quantitatively represent the performance of the algorithm, when using a set of segmentation parameters, called individual. We defined the fitness value as the degree of similarity $\overline{S}$ between the automatically detected contour and the manually drawn contour. The degree of similarity is defined as the percentage of points that is similar between two contours[14,15] in Eq 8-1:

$$S = \sum_{n=l}^{N} p_n(d) \quad \text{where } p_n(d) = \begin{cases} 1 \text{ if } d \leq T \\ 0 \text{ if } d > T \end{cases}, \qquad \text{Eq.(8-1)}$$

where d is the distance between each pair of corresponding points on the manually drawn contour and the automatically detected contour, N is the number of point per contour (N=100), and T is a distance threshold; distances are calculated along the entire contour[16]. Pairs of corresponding points are assumed to be similar if the distance does not exceed a certain threshold value T (T=2 mm), which approximately corresponds to the average distance $\overline{d}_{intra-observer}$ between two contours drawn by the same observer.

Optimization procedure using the GA

The GA library used in the optimization was previously described by Wall[11]. The optimization of the detection algorithm involves fourteen dependent parameters that constitute an individual. The optimization procedure was executed as a series of iterations, called generations. Each generation includes several individuals (called population) and can be described as follows:

Step 1:   automatic run of MASS package software with one individual at a time on a set of MR examinations,

Step 2:   calculate the average degree of similarity $\overline{S}$ between manual and automatically detected contours corresponding to the particular individual.

Step 3:   repeat steps 1 and 2 with all individuals included in the first population, thus creating the first generation.

Step 4:   The GA creates a new population of individuals by mating the best individuals from the current population producing new offspring (Figure 2). In each generation, the individuals are evaluated by calculating $\overline{S}$.

Step 5:   Determine whether the number of generations exceeds the preset maximum Gmax (Gmax=100 generations). If so, stop the iteration; otherwise go to Step 3.

As this process continues, the population converges towards better individuals defined by a higher $\overline{S}$.

Performance analysis: Optimization procedure for different MR pulse sequences

The GA family includes two different types of algorithm: GAs using "non-overlapping populations" and GAs using "overlapping populations". To study

Chapter

8

the ability of GAs to solve the optimization problem faced, only one GA needs to be tested. Only if this first step is fulfilled, we can go further in this work and test which GA is more appropriate to our optimization process. We considered the 2SGA belonging to the "overlapping population" GA family. We expected that using this process the optimization would converge faster than using a "non-overlapping populations" type of GA. The output of MASS was used to assess the average degree of similarity $\bar{S}$ between automatically detected contours corresponding to one individual and manually drawn contour. The best $\bar{S}$ defined the best individual per generation. Each individual is tested on the entire set of exams. 20 individuals were tested per generation on two different collections of cardiac MR images, one consisting of eleven sets acquired with a SSFP sequence and the other consisting of nine sets acquired with a GRE sequence. Ten optimization runs were performed on the two collections of examinations using Gmax=100. The average and standard deviation of the optimal parameter sets and the best fitness value ($\bar{S}$) found before and after the optimization were compared for the two collections of images.
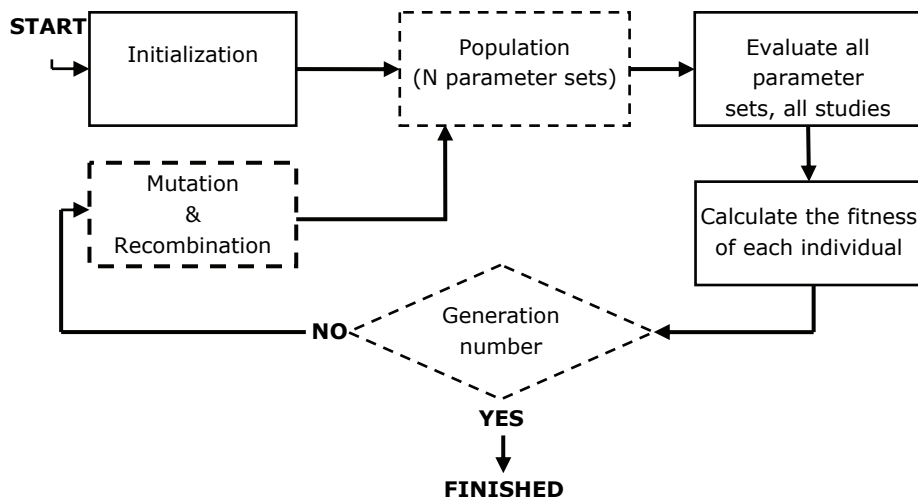
Figure 8-2. Flow chart illustrating the optimization process (the GA part is displayed in dotted lines; the solid Lines indicate the segmentation part).

8.3.2 Choice of the GA to use in the MASS optimization process

Fitness study

In this work, we tested two GA implementations (SGA and 2SGA 11) to determine which of them is more appropriate for optimizing the

segmentation algorithm used. The SGA uses non-overlapping populations of individuals. At each generation the algorithm creates an entirely new population as it was described before. Contrarily to SGA, 2SGA uses overlapping populations. In each generation the algorithm creates a temporary population of individuals, adds these to the previous population, then removes the worst individuals in order to reduce the population to its original size. The amount of overlap between generations can be specified by a replacement probability ($p_{replace}$). It corresponds to the percentage of the population that will be replaced at each new generation. The probability of mutation $p_{mut}=0.6$, combined with a crossover probability $p_{cross}=0.05$ was used with the SGA. For the 2SGA, a probability of mutation $p_{mut}=0.6$, a crossover probability $p_{cross}=0.05$, combined with a replacement probability $p_{replace}=0.9$ was fixed[11]. To test which of the two algorithms is more suitable to our optimization process, we analyzed the convergence of the fitness value $\overline{S}$ for both optimization processes on a set of 11 SSFP MR examinations using an arbitrarily chosen stop criterion ($G_{max}=100$) for 50 segmentation parameter sets or individuals. The optimal fitness values found with the SGA and the 2SGA algorithms, respectively, were compared and the algorithm with the highest fitness value was concluded to be the most suitable to solve the optimization problem under consideration.
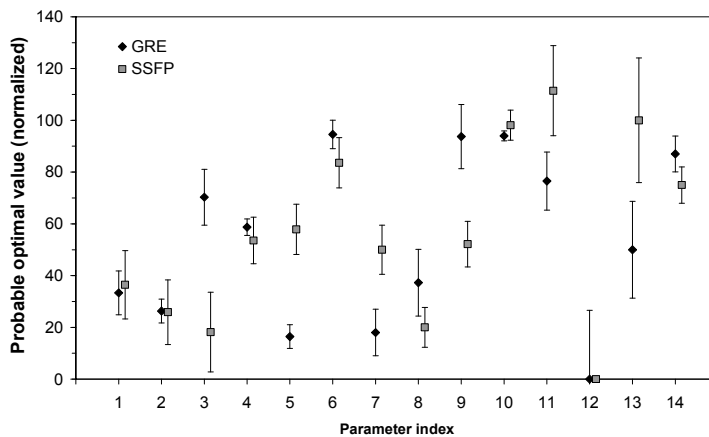
Figure 8-3. An optimization average and standard deviation of the 10 optimal values found for each parameter; these values were found after 10 optimization runs on examinations acquired with GRE and SSFP pulse sequence.

Chapter

8

Convergence speed

The most difficult part of a probabilistic search method is to predict when the process is completed. Each individual run is different because of the probabilistic nature of the algorithm. In Bevilacqua *et al.*[12] the evolution process stopped when the average of the six highest fitness values in a generation reached a plateau. In other words, the optimization process ends, when the fitness values and the standard deviation (SD) of the fitness values in a generation converge towards an asymptotic value. To compare the convergence speed of the two GAs (SGA and 2SGA), we analyzed the variation of the standard deviation between six highest fitness values per generation over the optimization processes.
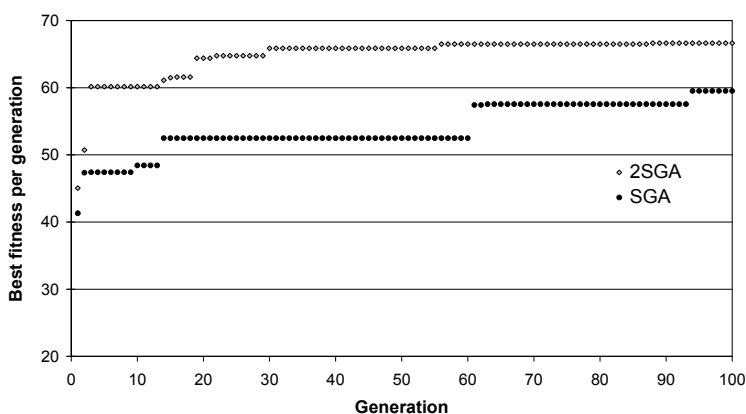
Figure 8-4. Optimization process using both 2SGA and SGA.

8.4 RESULTS

8.4.1 GA's capability to solve the MASS optimization problem

The optimization of the automatic segmentation on different pulse sequence (SSFP and GRE, respectively) resulted in different segmentation parameter sets (Figure 8-3). The average degree of similarity between automatically detected and manually drawn contours ($\bar{S}$) found with the segmentation algorithm before and after the optimization increased from $\bar{S} = 44.8\%$ in an earlier study on MASS[15] to $\bar{S} = 59.3\%$ in the set of images acquired with GRE pulse sequence and from $\bar{S} = 58.5\%$ to $\bar{S} = 66.7\%$ in the set of images acquired with SSFP pulse sequence.

8.4.2 Choice of the GA to use in MASS optimization process

Fitness study

To test the performance of the algorithm we focused first on the optimal fitness value found after 100 generations on the set of SSFP examinations. With 2SGA (p_{mut}=0.6, p_{cross}=0.05, $p_{replace}$=0.9) the optimal fitness function reached a value of $\bar{S} = 66.7\%$, whereas with the SGA (p_{mut}=0.6, p_{cross}=0.05) the optimal fitness value found was $\bar{S} = 59.5\%$ (Figure 8-3).

Test regarding the stop criteria

The performance of GAs is crucially dependent upon the loop termination criteria. We analyzed the evolution of the distribution of the six highest fitness values within a generation with the two different algorithms. Figure 8-4 clearly shows that the SD of the six highest fitness values increases when using the SGA method while no general trend of the SD is noticed when using the 2SGA.

Table 8-1. Average degree of similarity found per examination in the End-Systolic and End-diastolic phases found after the optimization of the segmentation algorithm.

Examination	Image type	Deg of similarity ED phase (%)	Deg of similarity ES phase (%)	CNR (ED phase)
1	SSFP	65.2	59.2	4.67
2	SSFP	47.6	47.4	2.86
3	SSFP	52.9	72.6	3.60
4	SSFP	64.7	85.7	5.00
5	SSFP	100.0	72.4	6.75
6	SSFP	76.3	46.3	4.64
7	SSFP	59.3	79.1	3.86
8	SSFP	92.2	92.1	5.43
9	SSFP	64.1	50.2	3.67
10	SSFP	58.6	48.8	3.00
11	GRE	78.3	54.2	3.00
12	GRE	43.9	45.9	1.40
13	GRE	54.2	42.1	1.67
14	GRE	47.9	56.9	1.61
15	GRE	59.7	61.2	3.00
16	GRE	58.6	51.2	1.75
17	GRE	53.2	67.9	2.08
18	GRE	54.4	76.6	1.92
19	GRE	47.4	68.6	2.00
20	GRE	68.2	78.6	2.80

Chapter

8

8.5 DISCUSSION

The goal of this work was to find a procedure to automatically optimize the segmentation parameters for the contour detection procedure in the MASS analytical software package.

The optimization requires a total of 14 dependent segmentation parameters to be adjusted simultaneously. The evaluation of one parameter takes approximately 36 s. With the assumption that these parameters are allowed to take only five different values, a brute-force method would require testing 5^{14} sets of segmentation parameters (or individuals). Due to time limitations, a brute-force method for tuning the segmentation algorithm used in MASS would be entirely impractical (as a matter of fact, a brute-force method would take approximately 36.5^{14} s, meaning years of calculation). On the other hand, the optimization of the segmentation algorithm needs to be done only once for a particular MR pulse sequence. Using the SGA and 2SGA approaches as optimization methods, a set of presumed optimal segmentation parameters can be found in 72 hours, with a maximum degree of similarity between the automatically detected contour and a gold standard, being manually drawn contours, of 59.3% (SGA) and 66.7% (2SGA). GAs appear to be a promising method to automatically tune the segmentation algorithm used in the MASS software package.

The average degree of similarity between automatically detected and manually drawn contours found with the segmentation algorithm increased with the optimization from 44.8% to 59.3% in the set of images acquired with a GRE pulse sequence, and from 58.5% up to 66.7% on the set of images acquired with SSFP pulse sequence. The different average degree of similarity found after the optimization in the two different set of images (GRE and SSFP, respectively) stressed the importance of optimizing the segmentation algorithm beforehand; the difference in the performance of the segmentation is directly linked to the different contrast to noise ratio (Table 8-1). This result illustrates the gain of optimizing the automatic segmentation algorithm (Figure 8-6 and Table 8-1). Moreover, at the end of the optimization process using 2SGA, the optimal set of segmentation parameters differed for different image characteristics. Hence, the increase in segmentation accuracy for images with different characteristics requires the use of automatic optimization procedures.
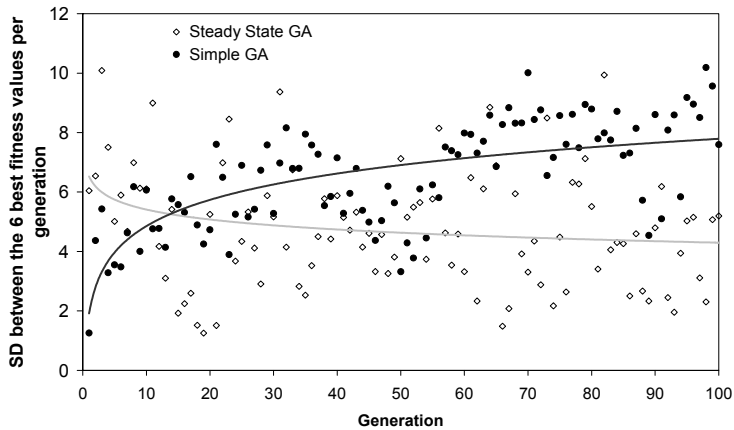
Figure 8-5. Graph displaying the variations of the standard deviation (SD) of the six highest fitness values found per generation using the SGA (simple GA) and the 2SGA (steady state GA), respectively. Each generation includes 50 individuals corresponding to 50 fitness values. The average and SD of the 6 best fitness values found per generation was calculated and displayed on the above-mentioned graph. The variation of the SD was assessed for the two GAs using two logarithm curves.

In this study, we analyzed two different GA methods presented in the literature: the SGA and 2SGA. In order to define which one was the more suitable to our optimization process, we focused on two different criteria: the segmentation accuracy reached at the end of the process (the optimal fitness value) and the convergence speed (the stop criteria). Using an *a-priori* defined stop criterion of 100 generations (G_{max}=100), we found that the optimized performance of the segmentation algorithm is higher for the 2SGA as compared to the SGA, $\bar{S} = 66.7\%$ vs. $\bar{S} = 59.5\%$ respectively. With respect to the convergence speed, the evolution of the SD of the fitness values within over generations was used as the criterion that determines which optimization-algorithm demonstrated the faster convergence. The SD of the fitness value is expected to decrease during the optimization process. Whereas no general trend in the SD of the fitness values could be detected using the 2SGA, the SD of the SGA fitness values diverges. Because convergence was defined as a decrease of the SD, none of the two algorithms was concluded to be the most suitable when using the stop criterion of 100 generations. Discrimination between the two algorithms will require some more experiments with higher generation numbers. Nevertheless, at this point of the study the 2SGA was more suitable to solve our optimization problem than the SGA that shows a SD increasing so a divergence of the algorithm.

Chapter

8

The intra-observer study is considered as a gold standard for assessment of variability according to clinical analysis. In this study, the intra-observer degree of similarity between manual endocardial contours was found to be 71% on GRE image data sets and 77% for SSFP image data sets. After application of the 2SGA-based algorithm, the degree of similarity of the automatic segmentation algorithm is comparable to the intra-observer degree of similarity. Thus, the accuracy of the optimized segmentation algorithm is now comparable to the accuracy of manual segmentation. Therefore, we conclude that the optimization method developed using 2SGA is a promising method to automate the procedure of finding the optimal parameter setting for LV endocardial segmentation of MR images acquired with SSFP and GRE pulse sequences in MASS.
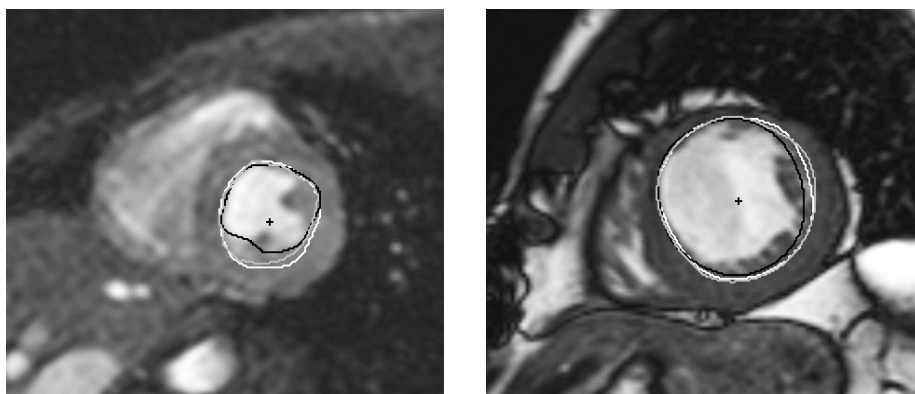
Figure 8-6. Illustration of the benefit of running the parameter optimization procedure. The manual contour (in white), the automatically detected prior to optimization (in black) and after optimization (in grey) are displayed on an MR image acquired using a GRE (Left) and SSFP (Right) acquisition sequence, respectively.

8.6 CONCLUSION

In this study, the need for automatic optimization of the segmentation algorithm used in the MASS software package has been demonstrated. The GA methods appeared to be suitable to fulfill the optimization task. This work demonstrated that the use of the 2SGA as an optimization method drastically increased the accuracy of the endocardial segmentation algorithm used in MASS. The MASS software package includes endocardial and epicardial contour detection algorithms. Since both of them need an initial set of parameters to run, the 2SGA is also an interesting tool to optimize the epicardial contour detection.

8.7 REFERENCES

1   van der Geest RJ, Buller VGM, Jansen E, Lamb HJ, Baur LHB, van der Wall EE, de Roos A, Reiber JHC. Comparison between manual and semiautomated analysis of left ventricle volume parameters from short-axis MR images. J Comput Assist Tomogr 1997; 21:756-765.
2   Cagnoni S, Dobrzeniecki AB, Poli R, Yanch JC. Genetic algorithm-based interactive segmentation of 3D medical images. Image and Vision Comput 1999; 17:881-895.
3   Holland J. Adaptation in natural and artificial systems (University of Michican Press, Ann Arbor, 1975).
4   Gavrielides MA, Lo JY, Floyd CE. Parameter optimization of a computer-aided diagnosis scheme for the segmentation of microcalcification clusters in mammograms. Med. Phys 2002; 29:475-483.
5   Fan Y, Jiang T, Evans DJ. Volumetric segmentation of brain images using parallel genetic algorithms. IEEE Trans. Med. Imag 2002; 21:904-909.
6   Liu H, Yu Y, Schell MC, O'Dell WG, Ruo R, Okunieff P. Optimal marker placement in photometry patient positioning system. Med Phys 2003; 30:103-110.
7   Capek M, Mroz L, Wegenkittl R. Robust and fast Medical Registration of 3D-multi-modality data sets. In conf. Medicom 2001, 515-518.
8   Tsutsui S. Genetic algorithms with a robust solution searching scheme. IEEE Trans Evol Comput 1997; 1:201-208.
9   Neves N, Nguyen AT, Torres EL. A study of non-linear optimization problem using a distributed genetic algorithm. In: the 25th Int. Conf. on Parallel Processing 1996.
10   Goldberg DE. Genetic algorithms in search, optimization, and machine learning, (1989).
11   Wall M. GAlib: A C++ Library of Genetic Algorithm Components. Lancet 1996, http://lancet.mit.edu/ga.
12   Bevilacqua A, Campanini R, Lanconnelli N. A distributed genetic algorithm for parameters optimization to detect microcalcifications in digital mammograms. In LNCS 2001, 278-287
13   Bosch H, van Burken G, Reiber JHC. Automated frame-to-frame contour detection in echocardiograms using motion estimation. IEEE Comput. Soc. Press 1992, 351-354.
14   Angelié E, Westenberg JJM, van der Geest RJ, Koning G, Reiber JHC. Definition of an optimal image analysis protocol for the assessment of left ventricular function from short-axis cardiac MR data sets. J Cardiovasc Magn Reson 2002; 4:125-127.
15   Angelié E, Westenberg JJM, van der Geest RJ, Danilouchkine M, Koning G, Reiber JHC. How to define the quality of a segmentation: Application for the assessment of left ventricular function from short-axis cardiac MR data sets. In: EuroCMR conference 2002, pp. 9-10.
16   Detmer PR, Bashein G, Martin RW. Matched filter identification of left-ventricular endocardial borders in transesophageal echocardiograms. IEEE Trans. Med. Imag 1990; 9:396-404.

Chapter

8

CHAPTER

9

Summary and conclusions

Over the period, in which the work described in this thesis was carried out, cardiovascular magnetic resonance (CMR) imaging has developed from an imaging modality primarily used for research into a routinely used clinical imaging modality which is applied every day in many hospitals worldwide. CMR has become the accepted gold standard for quantification of ventricular volumes. However, an MR scanner does not automatically generate quantitative results. It requires image segmentation, i.e. definition of object boundaries in the images, which is a time-consuming and tedious procedure when done manually. The availability of automated contour detection techniques that can accurately detect the myocardial boundaries in clinical CMR imaging studies would be of enormous value for routine clinical use of CMR.

The aim of this thesis was to investigate image processing techniques for automated and semi-automated assessment of quantitative parameters from cardiovascular magnetic resonance imaging studies.

Chapter 1 presents a general introduction to this thesis and defines the scope of the work.

In **Chapter 2** an overview is presented of image processing techniques which are used for quantitative analysis of various CMR acquisition protocols.

Chapter 3 describes an image segmentation method that was developed for the semi-automated detection of endocardial and epicardial contours for all slices and phases in short-axis cine MR imaging studies. Goal of this study was to evaluate the newly developed semi-automated contour detection algorithm.

The segmentation procedure presented in this chapter is based on multiple image processing steps including low-level techniques such as thresholding and edge detection using dynamic programming. Several constraints are incorporated in the various processing steps in order to increase the accuracy and robustness of the method. The segmentation algorithm is performed slice by slice, starting with the detection of the epicardial contour in the end-diastolic time-frame. A frame-by-frame detection of the epicardial contours in the remaining time-frames is performed by using the available epicardial contour of the ED frame as a model and deforming it such that the local image characteristics near the contour are similar to the corresponding location in the ED phase. Only a small deviation from the model contour is allowed, as it is known that the shape of the epicardial contour only shows little movement over the cardiac cycle.

Once the epicardial contours are available, the search for endocardial contours can be restricted to the region within the epicardial contour. The first step performed is finding an optimal threshold value separating the LV blood pool from the surrounding myocardium. The contour around the extracted blood pool serves as a first approximation of the endocardial contour. Concave sections in this contour are often caused by papillary muscles or trabecularization of the LV endocardial wall. Therefore a smooth convex hull around the extracted region is used as a better approximation of the endocardial contour. This contour is then used as input for dynamic programming, resulting in a locally more accurate contour.

A main ingredient of the developed contour detection procedure is the incorporation of available contours as *a priori* information when detecting other contours in the MR study. Since any automatically detected contour may be inaccurate, the use of such information may also lead to error propagation. Therefore, for each contour also the status was recorded and only those contours which are known to be valid are used as model information. A valid contour can either be a contour that was edited manually, or a contour that was initially detected automatically and then accepted by the operator. Using this concept, it was shown that the presented contour detection approach could be used to obtain accurate contours in all slices and phases of a study with minimal amount of contour

editing. For endocardial contours no manual editing was used at all. For epicardial contours, only in 1.4% of the images manual editing was performed. However, in this study, in the most basal slice level where no complete circumference of myocardium is present, both endo- and epicardial contours were traced manually.

Chapter 4 describes an automated contour detection method for the assessment of aortic flow from velocity-encoded cine MR imaging studies of the ascending aorta. Quantification of flow in the aorta can be used to derive the left ventricular stroke volume. In addition, by comparing aortic flow with pulmonary flow, the severity of shunts between the left and right heart chambers can be quantified.

Instantaneous aortic flow can be obtained by tracing a contour around the aortic cross-section and multiplying the cross-sectional area with the average blood flow velocity. To correct for the significant in-plane and through-plane motion as well as changes in cross-sectional shape over the cardiac cycle of the aorta, during manual image analysis the user is required to trace the vessel border in each individual image of the multi-phase MR examination, thereby carefully avoiding the inclusion of flow in adjacent regions from other vessels. Since this is a time consuming and tedious procedure which introduces observer variabilities, the automation of this process is desirable. The developed automated contour detection algorithm performs the segmentation in three separate steps. In the first step the user is required to identify an approximate center point of the aorta in one of the time frames. A contour around the aorta is detected and used as first approximation for the remaining time frames. To correct for in-plane motion of the aorta, the contour location is adjusted for each individual time frame, thereby enforcing a time-continuous motion pattern. Finally for each contour an edge based contour detection is performed to account for shape changes of the aortic cross-section.

The presented automated contour detection method fulfills the clinical requirements, as it requires minimal user interaction, it provides results which are in close agreement with results derived from manual contour tracing and has low inter- and intra-observer variability.

Chapter

9

In **Chapter 5** a new method is presented to obtain more accurate measurements of left ventricular wall thickness using a 3D extension of the Centerline method. The method takes advantage of the available 3D geometrical information of the acquired imaging planes. Conventional 2D approaches may result in overestimation of the true wall thickness in regions where the ventricular wall does not intersect at an exact 90° angle

with the imaging plane. This situation commonly occurs near the apex of the left ventricle. However, such overestimation may also be the result of inaccurate planning of the short-axis stack of images. Additionally, the extent of overestimation may vary over the cardiac cycle in case the left ventricle exhibits a significant change in orientation during contraction and relaxation.

Evaluation of the method using a data set of synthetic phantoms mimicking the geometry of the left ventricle, demonstrates the validity of the new approach. It is shown that over-estimation in wall thickness that typically occurs near the ventricular apex using the standard 2D Centerline method, is strongly reduced by applying the new 3D method. In addition, the 3D method is able to correct errors in wall thickness measurements that occur in case of inaccurate planning of the orientation of the stack of short-axis images. Using MR studies of normal volunteers, it is also shown that the 3D method results in less variability in wall thickness from base to apex and between different regions of the left ventricle. It should be noted that application of the 3D wall thickness calculation method requires multi-slice short-axis acquisitions with correct 3D alignment. In case the short-axis slices are acquired during separate breath-holds, image co-registration may be needed as a preprocessing procedure.

Chapter 6 describes a study evaluating an image processing algorithm for the automated detection of endocardial and epicardial boundaries of the left ventricle in time series of short-axis MR images based on an Active Appearance Motion Model (AAMM). In previous work the usefulness of AAM contour detection for the segmentation of the left and right ventricular boundaries in individual short-axis MR images had already been demonstrated. In this work an extension of the AAM contour detection was developed which performs modeling and contour detection for complete time-series of short-axis MR images. The rationale for this new approach is that by modeling the image information contained in a time-series of images, the automated segmentation procedure is expected to be more robust since all image data are used during the detection of a globally optimal time-continuous segmentation result. Poor image quality in particular time-frames will therefore not result in outlier contours.

In the AAMM, the appearance of the left ventricle is modeled for the systolic phase of the cardiac cycle by considering the image frames from ED to ES. For application of the AAMM contour detection method, for each study the ES time frame needs to be identified manually; the first time frame is assumed to represent ED. Using an iterative procedure the gray value difference between the synthetic AAMM image and the actual pixel

data is minimized by adjusting the pose parameters and the AAMM model parameters. This matching process results in the endocardial and epicardial contours for the complete time-series.

For the evaluation of the performance of the AAMM contour detection method a leave-one-subject-out approach is used. In three out of twenty studies the contour detection was not successful. For the remaining 17 studies a good agreement was found between manually derived and automatically derived global LV function parameters. Differences between manually and automatically derived results were 0.3±12% for the end-diastolic volume; 2±23% for the end-systolic volume; 0.1±6.7% for ejection fraction and for 0.7±15% for LV mass. These results compare favorably with the computed inter-observer variability for manual contour tracing.

Despite the good results, the study also shows a shortcoming of the AAMM contour detection method. In three studies the obtained contours do not fit to the actual endocardial and epicardial boundaries. Further inspection of these three studies reveals the presence of particular features in these studies that could explain the poor performance. Using a more extended training set of CMR exams including more pathological cases may alleviate this problem.

In **Chapter 7** an automated contour detection technique is described which is based on tracking of landmark points over the cardiac cycle. The landmarks are positioned at the myocardial boundary and are tracked over the cardiac cycle using a multi-dimensional dynamic programming (ND-DP) technique. As input, the method requires an existing contour in one of the time frames. In this study, the method is initialized using a manually traced contour in the mid-systolic time frame and 32 landmarks are defined at evenly spaced intervals along the contour. Image information around the defined landmarks is used to find likely locations for the landmark in other time frames. Within the ND-DP framework constraints are imposed on the allowed motion of a landmark, i.e. 1) the maximal excursion should be less than a certain threshold; 2) the maximal displacement from frame to frame is limited; and 3) since the image sequence describes a complete cardiac cycle, the path described by a landmark must be cyclic.

The proposed method has a number of important advantages. First, the contour detection result is relatively insensitive to individual image frames with poor image quality. Second, since an image matching strategy is used to find the likely locations of a landmark, the tracking results are also reliable in case part of the contour is defined in an area without clear edges. This advantage is especially of importance near the papillary

muscles for the endocardial boundaries and regions of poor contrast or epicardial fat during the detection of epicardial contours.

Quantitative evaluation of the method was performed on 20 CMR data sets of 18 patients with several pathologies and 2 normal volunteers. Compared to results derived by manual tracing, errors in end-diastolic volume, end-systolic volume and ejection fraction were smaller than 5%. Border position errors were in the order of one pixel.

The general applicability of the ND-DP method is further demonstrated in another segmentation problem. ND-DP is applied to a temporal series of MR phase-contrast images of the ascending aorta. A six-dimensional implementation was tested using four radii and the x,y position of the aorta center. By imposing a temporal continuity constraint on all six parameters, temporal tracking of the contour describing the aortic cross-section was performed successfully.

The motivation for the work described in **Chapter 8** is that image characteristics are highly dependent on the MRI scanner used and the applied scanning protocol. Therefore for optimal performance, the parameter settings of an automated contour detection method, such as the one described in Chapter 3, needs to be fine-tuned for a specific MR acquisition protocol. Since the optimal value of a parameter can be dependent on the values of other parameters, finding the optimal values for all parameters is a non-trivial task. Searching for the optimal settings can be seen as a high-dimensional optimization problem. In this study the value of genetic algorithm based parameter optimization is studied for this particular problem. To this end the automated endocardial contour detection algorithm as described in Chapter 3 is tested on MR image data acquired with either a gradient-echo (GRE), or a Steady State Free Procession (SSFP) protocol. Based on earlier experience, 15 parameters are selected for the optimization. It is demonstrated that compared to the default setting of the parameters a significant improvement in detection performance is obtained after parameter optimization. This study also reveals that the contour detection algorithm, although originally developed for GRE MR image data, is also applicable for images acquired using a SSFP protocol. It can be concluded that parameter optimization using genetic algorithms is a practical technique for optimization of the performance of a contour detection method for a particular type of image data.

9.1 GENERAL CONCLUSIONS

Cardiac Magnetic Resonance Imaging (CMR) has become an important clinical imaging modality for cardiac evaluation. Reliable computer

algorithms for quantitative image analysis, including automated contour detection, are therefore of enormous clinical importance. The purpose of this thesis, as described in the first chapter, was to develop and validate automated contour detection techniques for quantitative evaluation of cardiac MR examinations that can be used in a routine clinical setting.

The automated contour detection techniques described in the thesis were all applied to clinical CMR data and the results of automated contour detection were compared to manually traced contours as gold standard. A high agreement with manual image analysis was demonstrated for the presented contour detection techniques. For all algorithms developed it was attempted to make effective use of available *a priori* information. The algorithms described in chapter 2 and 7 use information from manually traced or edited contours as *a priori* information to guide the contour detection in other frames. This however implies that these algorithms are dependent on manual interaction. The AAMM contour detection technique described in Chapter 6 only requires the manual definition of the end-systolic phase, while the contour detection itself runs fully automatically. The *a priori* information used in this algorithm is derived from a training set of CMR exams with available contours.

A possible direction in realizing the ultimate goal of accurate and robust fully automated contour detection in clinically acquired CMR imaging studies is by combining several components of the algorithms described in this thesis. The large variability in image characteristics and inter-patient differences requires the use of *a priori* information. The segmentation of the apical and basal short-axis slices, which are more difficult to process automatically, can be supported by taking advantage of available images acquired in the long-axis orientation. While fully automated contour detection seems attractive, also the use of more efficient methods of user-interaction is worth investigating. The combination of advanced automated contour detection techniques, optimal visualization and advanced user interaction may result in the most viable solution.

In conclusion, in this thesis we have developed and validated various automated contour detection techniques and image analysis approaches for quantitative analysis of cardiac MR imaging studies. The developed methods have also been integrated into analytical software packages that are being used in many clinical centers worldwide. Based on the work described in the thesis and the large quantity of clinical journal papers in which the developed approaches have been applied for clinical research, we may conclude that we have realized the goals that were set at the start of the thesis.

Chapter

9

CHAPTER

10

Samenvatting en conclusies

Over de periode waarin het werk van dit proefschrift is verricht heeft cardiovasculaire Magnetische Resonantie (CMR) Imaging zich ontwikkeld van een beeldmodaliteit primair voor onderzoekstoepassing, tot een routinematig gebruikte klinische beeldmodaliteit welke wereldwijd iedere dag toegepast wordt. CMR wordt nu gezien als de geaccepteerde gouden standaard voor de kwantificatie van ventrikelvolumina. Echter, kwantitatieve meetgegevens worden niet automatisch gegenereerd door de MRI scanner. Het vereist beeldsegmentatie, i.e. de definitie van de begrenzingen van objecten in de beelden, hetgeen een tijdrovende en belastende procedure is indien uitgevoerd middels het handmatig tekenen van contouren. De beschikbaarheid van automatisch contourdetectie technieken welke nauwkeurig de contouren van de hartspier kunnen detecteren in klinische CMR onderzoeken zou van enorm klinisch belang zijn voor de routinematige toepassing van CMR.

Het doel van dit proefschrift was om beeldverwerkingstechnieken te onderzoeken voor de automatische en semi-automatische bepaling van kwantitatieve parameters voor cardiovasculaire magnetische kernspin-resonantie technieken.

Hoofdstuk 1 geeft een algemene inleiding tot dit proefschrift en definieert het kader van het werk.

In **hoofdstuk 2** wordt een overzicht gepresenteerd van de beeldverwerkingstechnieken die toegepast worden voor de kwantitatieve analyse van verschillende CMR beeldacquisitieprotocollen.

Hoofdstuk 3 beschrijft een beeldsegmentatiemethode die werd ontwikkeld voor de semi-automatische detectie van endocardiale en epicardiale contouren voor alle beeldvlakken en fasen in korte-as MR onderzoeken. Het doel van deze studie was de evaluatie van het nieuw ontwikkelde semi-automatische contourdetectie algoritme.

De in dit hoofdstuk gepresenteerde segmentatieprocedure is gebaseerd op meerdere beeldverwerkingsstappen, inclusief 'low-level' technieken zoals drempeling en rand-detectie gebruik makend van dynamisch programmeren. Om de nauwkeurigheid en de robuustheid van de methode te verbeteren zijn meerdere randvoorwaarden geïncorporeerd in de verschillende verwerkingsstappen. De beeldvlakken worden door het segmentatiealgoritme één voor één verwerkt, beginnende met de detectie van de epicardiale contour in het einddiastolische (ED) tijdsmoment. De detectie van de epicardiale contouren in de overige fasen wordt uitgevoerd middels een fase-na-fase detectie, waarbij de epicardiale contour in het ED beeld als model wordt gebruikt, welke zodanig wordt vervormd dat de lokale beeldkarakteristieken in de naburigheid van de contour overeenkomen met de corresponderende locaties in het ED beeld. Hierbij wordt slechts een kleine deviatie van de model-contour toegestaan, gegeven de kennis dat een epicardiale contour slechts een kleine beweging laat zien over een hartcyclus.

Zodra de epicardiale contouren beschikbaar zijn, kan het zoekgebied voor endocardiale contouren worden beperkt tot het gebied binnen de epicardiale contour. Als eerste stap wordt hierbij een optimale drempelwaarde bepaald welke het bloedgebied isoleert van de omliggende hartspier. De contour rondom het geïsoleerde bloedgebied dient als eerste benadering van de endocardiale contour. Concave delen in deze contouren zijn vaak het gevolg van papillairspieren of trabecularisatie van de endocardiale hartwand. Een gladde convexe omhullende rondom het gevonden gebied wordt daarom gebruik om tot een betere benadering van de endocardiale contour te komen.

Een belangrijk element van de ontwikkelde contourdetectie procedure is het gebruik maken van reeds beschikbare contouren als *a priori* informatie bij het detecteren van andere contouren binnen de MR studie. Aangezien automatisch gedetecteerde contouren onnauwkeurig kunnen zijn, kan het gebruik maken van deze informatie ook leiden tot fout propagatie. Daarom wordt van iedere contour ook de status bijgehouden en

alleen die contouren waarvan de juistheid bekend is, worden gebruikt als modelinformatie. Geldige contouren zijn, ofwel contouren die handmatig zijn aangepast, dan wel contouren die initieel automatisch werden gedetecteerd en daarna handmatig geaccepteerd door de gebruiker. Gebruik makend van dit concept kon worden aangetoond dat de gepresenteerde contourdetectie aanpak gebruikt kon worden om nauwkeurige contouren te bepalen in alle beeldvlakken en fasen van een studie met minimaal gebruik van handmatige correcties. Het was niet toegestaan om endocardiale contouren aan te passen. Handmatige aanpassing van epicardiale contouren werd in slechts 1.4% van de beelden toegepast. Echter, in deze studie werden de contouren van het meest basale beeldvlak handmatig getekend.

Hoofdstuk 4 beschrijft een automatische contourdetectiemethode voor het bepalen van de bloedstroming in de aorta op basis van snelheidsgecodeerde MRI studies van de ascenderende aorta. Kwantificatie van de bloedstroming in de aorta kan gebruikt worden om het linkerventrikel slagvolume af te leiden. Tevens kan, door de bloed stroming in de aorta met die van de pulmonaalarterie te vergelijken, de ernst van een pathologische verbinding tussen de linker en rechter harthelft worden gekwantificeerd.

De instantane aorta bloedstroming kan worden bepaald door een contour te tekenen rondom de doorsnede van de aorta en het oppervlakte van de doorsnede te vermenigvuldiging met de gemiddelde bloedstroomsnelheid. Tijdens de manuele beeldanalyse is het noodzakelijk om te corrigeren voor de aanzienlijke beweging van de aorta in het beeldvlak en door het beeldvlak heen, evenals voor de vormveranderingen van de doorsnede van de aorta in elk individueel beeld van de multi-fase MR opname. De inclusie van naburige delen in het beeld met een snelheid behorende bij een ander vat dient voorkomen te worden. Aangezien dit een tijdrovende en belastende procedure is welke gepaard gaat met gebruikers variaties, is het automatiseren van dit proces zeer gewenst. Het ontwikkelde automatische contourdetectie algoritme voert de segmentatie uit in drie afzonderlijke stappen. In de eerste stap dient de gebruiker een middelpunt aan te geven in het midden van de aorta in één van de fasen. In dit beeld wordt vervolgens een contour rondom de aorta gedetecteerd, welke gebruikt zal worden als eerste benadering voor de overige fasen. Om te corrigeren voor de verplaatsing van de aorta in het beeldvlak wordt de contourpositie aangepast voor elk individueel tijdsmoment. Hierbij wordt een tijdcontinue beweging afgedwongen. In de laatste stap wordt voor elke

contour een beeldrand gebaseerde contourdetectie uitgevoerd om te corrigeren voor vormveranderingen van de aorta doorsnede in het beeld

Het gepresenteerde automatische contourdetectie algoritme voldoet aan de klinische eisen, aangezien de benodigde gebruikers-interactie minimaal is, de resultaten goed overeen komen met die van handmatige analyse en de methode een zeer geringe inter- en intra-gebruikers variabiliteit kent.

In **Hoofdstuk 5** wordt een nieuwe methode gepresenteerd voor een nauwkeuriger bepaling van linkerventrikel wanddikte metingen, gebruik makend van een extensie van de 'Centerline' methode. De methode maakt gebruik van de 3D geometrische informatie van de opgenomen beeldvlakken. De conventionele 2D methode kan leiden tot overschatting van de werkelijke wanddikte in gebieden waar de hoek van de ventrikelwand met het beeldvlak niet exact gelijk is aan 90°. Deze situatie komt veelvuldig voor rondom de apex van het linkerventrikel. Een dergelijke overschatting kan echter ook het gevolg zijn van het onnauwkeurig plannen van de stapel van korte-as beelden. Daarnaast kan de mate van overschatting variëren over de hartcyclus in geval het linkerventrikel een significante oriëntatie verandering ondergaat gedurende contractie en relaxatie.

Evaluatie van de methode gebruik makend van een data set van synthetische fantomen met een geometrie gelijkend aan het linkerventrikel, toont de validiteit aan van de methode. Het wordt aangetoond dat wanddikte overschatting in het apicale gebied, die optreden bij het gebruik van de standaard 2D Centerline methode, met de nieuwe 3D methode sterk wordt gereduceerd. Daarnaast is de 3D methode in staat om fouten te corrigeren in de wanddikte metingen ten gevolge van onnauwkeurige planning van de oriëntatie van de korte-as beeldvlakken. Gebruik makend van MR studies van normale vrijwilligers wordt ook aangetoond dat de 3D methode leidt tot vermindering van de variabiliteit in wanddikte van basis tot apex en tussen verschillende regio's van het linkerventrikel. Het is belangrijk op te merken dat toepassing van de 3D wanddikte methode een juiste 3D uitlijning vereist van de multi-fase korte-as beeldvlakken. Indien de korte-as beelden worden opgenomen in afzonderlijke periodes van ademstilstand, kan een beeld co-registratie nodig zijn als een voorbewerkingstap.

Hoofdstuk 6 beschrijft een evaluatiestudie van een beeldverwerkingalgoritme voor de automatische detectie van endocardiale en epicardiale begrenzingen van het linkerventrikel in tijdseries van korte-

as MRI beelden gebaseerd op een 'Active Appearance Motion Model' (AAMM). In eerder werk werd het nut van AAM contourdetectie voor de segmentatie van het linker- en rechterventrikel in individuele korte-as MR beelden al aangetoond. In dit werk wordt een extensie van AAM contourdetectie geïntroduceerd, waarbij het modelleren en het detecteren in complete tijdseries van korte-as MR beelden geschiedt. De achterliggende gedachte achter deze nieuwe aanpak is dat het modelleren van beeldinformatie over een gehele tijdserie van beelden de automatische segmentatie procedure robuuster zal maken, omdat alle beelddata gebruikt wordt tijdens de detectie van een globaal optimaal tijdcontinu segmentatieresultaat. Slechte beeldkwaliteit in individuele beelden zal daarom niet leiden tot uitbijtercontouren.

In de AAMM wordt de 'appearance' van het linkerventrikel gemodelleerd voor de systolische fase van de hartcyclus gebruik makend van de fasen van ED tot en met ES. Om AAMM contourdetectie te kunnen toepassen dient de gebruiker voor elke studie de ES fase aan te duiden; de eerste fase wordt als ED moment verondersteld. Met behulp van een iteratieve procedure wordt het grijswaarde verschil geminimaliseerd tussen het synthetische AAMM beeld en de werkelijke pixel data door de pose en de AAMM model parameters aan te passen. Dit matchingsproces resulteert uiteindelijk in de endocardiale en epicardiale contouren voor de gehele tijd-serie.

Bij de evaluatie van de prestaties van de AAMM contourdetectiemethode is gebruik gemaakt van een 'leave-one-subject-out' aanpak. De contourdetectie was niet succesvol in drie van de twintig studies. In de overige 17 studies wordt een goede overeenkomst gevonden tussen manueel en automatisch afgeleide globale LV functie parameters. De verschillen tussen manueel en automatisch bepaalde resultaten waren voor het einddiastolisch volume 0.3±12%; voor het eindsystolisch volume 2±23%; voor de ejectiefractie 0.1±6.7% en voor LV massa 0.7±15%. Deze resultaten komen goed overeen met berekende inter-operator en intra-operator variabiliteit voor het manueel contouren tekenen.

Ondanks de goede resultaten laat de studie ook een tekortkoming van de AAMM contourdetectie methode zien. In drie studies passen de gedetecteerde contouren niet goed op de werkelijke endocardiale en epicardiale contouren. Verdere inspectie van deze drie studies brengt aan het licht dat, bepaalde in deze studies aanwezige features, mogelijk de oorzaak zijn van de slechte prestaties. Toepassing van een uitgebreidere trainingset van CMR studies, inclusief een groter aantal pathologische gevallen, kan mogelijk een oplossing bieden voor dit probleem.

Chapter

10

In **Hoofdstuk 7** wordt een automatische contourdetectietechniek beschreven die gebaseerd is op het vervolgen van markeringspunten over een hartcyclus. De markeringspunten worden gepositioneerd op de grens van de hartspier en vervolgd over de hartcyclus gebruik makend van een multi-dimensionale dynamisch programmeer techniek (ND-DP). De methode vereist als invoer een bestaande contour in één van de tijdsmomenten. In deze studie wordt de methode geïnitialiseerd met een manueel getekende contour in de mid-systolische fase met 32 markeringspunten verdeeld rondom de contour. Gebruik makend van de beeldinformatie rondom een markeringspunt worden aannemelijke locaties voor het markeringspunt in andere tijdmomenten gevonden. Binnen het ND-DP raamwerk worden beperkingen opgelegd ten aanzien van de toegestane verplaatsing van een markeringspunt: 1) de maximale verplaatsing dient kleiner te zijn dan een bepaalde drempelwaarde; 2) de maximale verplaatsing tussen twee opeenvolgende tijdsmomenten is beperkt; en 3) aangezien de tijdserie van beelden een complete hartcyclus beschrijft, dient het door de markeringspunten beschreven pad cyclisch te zijn.

De voorgestelde methode heeft een aantal belangrijke voordelen. Ten eerste, het resultaat van contourdetectie is relatief ongevoelig voor individuele tijdsmomenten met slechte beeldkwaliteit. Ten tweede, doordat een beeld-matchingsstrategie wordt gebruikt om de waarschijnlijke markeringspuntlocaties te vinden, is het resultaat van vervolgen ook betrouwbaar indien een deel van de contour gedefinieerd is in een gebied zonder duidelijke beeldranden. Dit voordeel is in het bijzonder van belang rondom de papillairspieren bij de detectie van de endocardiale begrenzingen en in gebieden met een slecht contrast of epicardiaal vet bij de detectie van epicardiale contouren.

Kwantitatieve evaluatie van de methode wordt uitgevoerd op 20 CMR data sets van 18 patiënten met verschillende pathologiën en 2 gezonde vrijwilligers. Vergeleken met manueel behaalde resultaten, zijn de fouten in einddiastolisch volume, eindsystolisch volume en ejectiefractie kleiner dan 5%. De contour positie fouten zijn in de orde van een pixel.

De generieke toepasbaarheid van de ND-DP methode wordt vervolgens aangetoond middels een ander segmentatieprobleem. ND-DP wordt toegepast op een temporele serie van MR fase-contrast beelden van de ascenderende aorta. Een zes-dimensionale implementatie wordt getest gebruik makend van vier stralen en de x,y positie van de aorta. Gebruik makend van een randvoorwaarde ten aanzien van de temporele continuïteit voor alle zes parameters, wordt op succesvolle wijze de contour rondom de aorta doorsnede vervolgd over de tijd.

De motivatie voor het werk beschreven in **hoofdstuk 8** is dat beeldkarakteristieken in hoge mate afhankelijk zijn van de gebruikte MRI scanner en het toegepaste scan protocol. Voor optimale prestaties van een automatisch contourdetectie methode, zoals die beschreven in Hoofdstuk 3, dienen de parameter instellingen optimaal te worden afgestemd voor een specifiek MR opname protocol. Aangezien de optimale waarde van een parameter afhankelijk kan zijn van de waarde van andere parameters, is het vinden van de optimale waarde voor alle parameters geen triviale taak. Het zoeken naar de optimale instellingen kan worden gezien als een hoogdimensionaal optimalisatie probleem. In deze studie wordt voor dit specifieke probleem de waarde onderzocht van parameter optimalisatie met behulp van genetisch algoritmen. Hiertoe wordt het in hoofdstuk 3 beschreven automatische contourdetectiealgoritme getest op MR beelden die opgenomen zijn met een *Gradient-Echo* (GRE) of *Steady State Free Precession* (SSFP) protocol. Op basis van eerdere ervaringen worden 15 parameters geselecteerd voor de optimalisatie. Aangetoond wordt dat, in vergelijking met de initiële instelling van de parameters, de prestaties van het contour detectie algoritme aanzienlijk verbeteren na toepassing van parameter optimalisatie. De studie laat ook zien dat het contourdetectiealgoritme, hoewel oorspronkelijk ontwikkeld voor GRE MR beelden, ook toegepast kan worden op beelden die opgenomen zijn met een SSFP protocol. Er kan geconcludeerd worden dat parameter optimalisatie met behulp van genetische algoritmen een praktische techniek is om de prestaties van een contourdetectie methode te optimaliseren voor beelden die opgenomen zijn met een bepaald opnameprotocol.

10.1 ALGEMENE CONCLUSIES

Cardiale Magnetische Resonantie Imaging (CMR) is een belangrijke klinische beeldmodaliteit geworden voor de evaluatie van het hart. Betrouwbare computer algoritmen voor kwantitatieve beeldanalyse, inclusief automatische contour detectie, zijn daarom van enorm klinisch belang. Het doel van dit proefschrift, zoals beschreven in het eerste hoofdstuk, was de ontwikkeling en validatie van automatische contour-detectietechnieken voor de kwantitatieve analyse van cardiale MRI onderzoeken die geschikt zijn voor routinematige klinisch gebruik.

Alle in dit proefschrift beschreven contourdetectietechnieken werden toegepast op klinische CMR data en de resultaten van automatische contourdetectie werden vergeleken met manueel getekende contouren als gouden standaard. De gepresenteerde contourdetectietechnieken lieten een

Chapter

10

goede overeenkomst zien met manueel getekende contouren. Bij alle algoritmen werd getracht om effectief gebruik te maken van beschikbare *a priori* informatie. De in Hoofdstuk 2 en 7 beschreven algoritmen gebruiken manueel getekende of aangepaste contouren als *a priori* informatie om de detectie in andere tijdsmomenten aan te sturen. Dit betekent dat deze algoritmen wel afhankelijk zijn van manuele interactie. De AAMM contour detectie techniek, beschreven in Hoofdstuk 6, is slechts afhankelijk van het manueel aangeven van de eindsystolische fase, terwijl het algoritme zelf volledig automatisch verloopt. De door dit algoritme gebruikte *a priori* informatie is afgeleid van een leerset van CMR studies met beschikbare contouren.

Een mogelijke richting om het ultieme doel te bereiken van een nauwkeurige en robuuste volledig automatische contourdetectie voor klinisch opgenomen cardiale MRI studies is door het combineren van verschillende componenten van de in het proefschrift beschreven algoritmen. De grote mate van variatie in beeld karakteristieken en inter-patiënt verschillen, maken het gebruik van *a priori* informatie noodzakelijk. De segmentatie van de apicale en basale korte-as beelden, welke moeilijker te verwerken zijn, kan worden ondersteund door gebruik te maken van beschikbare beelden die opgenomen zijn in de lange-as oriëntatie. Hoewel volledig automatische detectie aantrekkelijk lijkt, is ook het benutten van efficiëntere gebruikersinteractie de moeite waard om nader te onderzoeken. De meest praktische oplossing ligt mogelijk in de combinatie van geavanceerde contourdetectie technieken, optimale visualisatie en geavanceerde gebruikersinteractie.

Concluderend hebben we in dit proefschrift verschillende automatische contourdetectie en beeld analyse technieken ontwikkeld en gevalideerd voor de kwantitatieve analyse van cardiale MRI studies. De ontwikkelde methoden zijn ook geïntegreerd in analytische software pakketten welke wereldwijd door vele klinische centra worden toegepast. Op basis van het in dit proefschrift beschreven werk en de grote hoeveelheid artikelen in wetenschappelijke klinische tijdschriften waarin de ontwikkelde methoden zijn toegepast voor klinisch onderzoek, mogen we concluderen dat de gestelde doelen voor het proefschrift zijn gerealiseerd.

CHAPTER

11

Publications

11.1 Refereed papers in international journals

1. **van der Geest RJ**, Morris KG, Cusma JT, Reiber JHC. Postmortem validation of the automated coronary analysis (ACA) software package. Int J Cardiac Imag 1994; 10:95-102.
2. Helbing WA, Bosch JG, Maliepaard C, Rebergen SA, **van der Geest RJ**, Hansen B, Ottenkamp J, Reiber JHC, de Roos A. Comparison of echocardiographic methods with magnetic resonance imaging for assessment of right ventricular function in children. Am J Cardiol 1995; 76:589-594.
3. Hoogendoorn LI, Pattynama PMT, Buis B, **van der Geest RJ**, van der Wall EE, de Roos A. Noninvasive evaluation evaluation of aortocoronary bypass grafts with magnetic resonance flow mapping. Am J Cardiol 1995; 75:845-848.
4. Lamb HJ, Singleton RR, **van der Geest RJ**, Pohost GM, de Roos A. MR imaging of regional cardiac function: Low-pass filtering of wall thickness curves. Magnetic Resonance in Medicine 1995; 34:498-502.
5. Pattynama PMT, Lamb HJ, van der Velde EA, **van der Geest RJ**, van der Wall EE, de Roos A. Reproducibility of MRI-derived measurements of right ventricular volumes and mass. Magnetic Resonance Imaging 1995; 13:53-63.
6. Holman ER, Vliegen HW, **van der Geest RJ**, Reiber JHC, van Dijkman PRM, van der Laarse A, de Roos A, van der Wall EE. Quantitative analysis of regional left ventricular function after myocardial infarction in the pig assessed with cine magnetic resonance imaging. Magn Reson Med 1995; 34:161-169.
7. Dendale PAC, Franken PR, Waldman GJ, Baur LHB, Vandamme S, **van der Geest RJ**, de Roos A. Regional diastolic wall motion dynamics in anterior infarction: analysis and quantification with magnetic resonance imaging. Coronary Artery Disease 1995; 6:723-729.
8. Cusma JT, Spero LA, **van der Geest RJ**, Bashore TM, Morris KG. Application of quantitative coronary angiography in a cineless environment: In vivo asessment of a fully automated system for clinical use. Am Heart J 1995; 129:300-306.

9. Matheijssen NAA, Baur LHB, Reiber JHC, van der Velde EA, van Dijkman PRM, **van der Geest RJ**, de Roos A. Assessment of left ventricular volume and mass by cine-magnetic resonance imaging in patients with anterior myocardial infarction intra-observer and inter-observer variability on contour detection. Int J Cardiac Imag 1996; 12:11-19.

10. Niezen RA, Helbing WA, **van der Geest RJ**, Rebergen SA, de Roos A. Biventricular systolic function and mass studied with MR imaging in children with pulmonary regurgitation after repair for Tetralogy of Fallot. Radiology 1996; 201:135-140.

11. Helbing WA, Niezen RA, le Cessie S, **van der Geest RJ**, Ottenkamp J, de Roos A. Right ventricular diastolic function in children with pulmonary regurgitation after repair of Tetralogy of Fallot: Volumetric evaluation by magnetic resonance velocity mapping. J Am Coll Cardiol 1996; 28:1827-1835.

12. Baur LHB, Schipperheyn JJ, van der Velde EA, van der Wall EE, Reiber JHC, **van der Geest RJ**, van Dijkman PRM, Gerritsen JG, van Eck-Smit BLF, Voogd PJ, Bruschke AVG. Reproducibility of left ventricular size, shape and mass with echocardiography, magnetic resonance imaging and radionuclide angiography with anterior wall infarction. A plea for core laboratories. Int J Card Imag 1996; 12:233-240.

13. **van der Geest RJ**, Buller VGM, Jansen E, Lamb HJ, Baur LHB, van der Wall EE, de Roos A, Reiber JHC. Comparison between manual and automated analysis of left ventricular volume parameters from short axis MR images. J Comput Assist Tomogr 1997; 21:756-765.

14. **van der Geest RJ**, de Roos A, van der Wall EE, Reiber JHC. Quantitative analysis of cardiovascular MR images. Int J Card Im 1997; 13:247-258.

15. Holman ER, Buller VGM, de Roos A, **van der Geest RJ**, Baur LHB, van der Laarse A, Bruschke AVG, Reiber JHC, van der Wall EE. Detection and quantification of dysfunctional myocardium by magnetic resonance imaging: A new three-dimensional method for quantitative wall-thickening analysis. Circulation 1997; 95:924-931.

16. Johnson DB, Foster RE, Barilla F, Blackwell GG, Roney M, Stanley AWH, Kirk K, Orr RA, **van der Geest RJ**, Reiber JHC, Dell'Italia LJ. Angiotensin-converting enzyme Inhibitor therapy affects left ventricular mass in patients with ejection fraction >40% after acute myocardial infarction. J Am Coll Cardiol 1997; 29:49-54.

17. Kayser HWM, Stoel BC, van der Wall EE, **van der Geest RJ**, de Roos A. MR velocity mapping of tricuspid flow: Correction for through-plane motion. J Magn Reson Im 1997; 7:669-673.

18. Buller VGM, **van der Geest RJ**, Kool MD, van der Wall EE, de Roos A, Reiber JHC. Assessment of regional left ventricular wall parameters from short-axis MR imaging using a 3D extension to the improved centerline method. Invest Radiol 1997; 32:529-539.

19. Dendale P, Franken PR, Meusel M, **van der Geest RJ**, de Roos A. Distinction between open and occluded infarct-related arteries using contrast-enhanced magnetic resonance imaging. Am J Cardiol 1997; 80:334-335.

20. **van der Geest RJ**, Niezen RA, van der Wall EE, de Roos A, Reiber JHC. Automated measurement of volume flow in the ascending aorta using MR velocity maps: evaluation of inter- and interobserver variability in healthy volunteers. J Comp Assist Tomogr 1998; 22:904-911.

21. Westenberg JJM, Wasser MNJM, **van der Geest RJ**, Pattynama PMT, de Roos A, Vanderschoot J, Reiber JHC. Variations in blood flow waveforms in stenotic renal arteries by 2D phase-contrast Cine MRI. JMRI 1998; 8:590-597.

22. Kroft LJM, Doornbos J, **van der Geest RJ**, van der Laarse A, van der Meulen H, de Roos A. Ultrasmall superparamagnetic particles of iron oxide (USPIO) MR imaging of infarcted myocardium in pigs. MRI 1998; 16:755-763.

23. Postema S, Pattynama PMT, Broker, **van der Geest RJ**, van Rijswijk CSP, Trimbos JB. Fast dynamic contrast-enhanced colour-coded MRI in uterine cervix carcinoma: Useful for tumour staging? Clinical Radiology 1998; 53:729-734.
24. Westenberg JJM, **van der Geest RJ**, Wasser MNJM, Doornbos J, Pattynama PMT, de Roos A, Vanderschoot J, Reiber JHC. Objective stenosis quantification from post-stenotic signal loss in phase-contrast magnetic resonance angiographic datasets of flow phantoms and renal arteries. MRI 1998; 16:249-260.
25. Marcus JT, Götte MJW, de Waal LK, Stam MR, **van der Geest RJ**, Heethaar RM, van Rossum AC. The influence of through-plane motion on left ventricular volumes measured by magnetic resonance imaging: implications for image acquisition and analysis. J Cardiovasc Magnetic Resonance 1998; 1:1-6.
26. **van der Geest RJ**, Reiber JHC. Quantification in cardiac MRI. J Magn Reson Imag 1999; 10:602-608.
27. Lelieveldt BPF, **van der Geest RJ**, Ramze Rezaee M, Bosch JG, Reiber JHC. Anatomical model matching with fuzzy implicit surfaces for segmentation of thoracic volume scans. IEEE Transactions on Medical Imaging 1999; 18:218-230.
28. Kroft LJM, Doornbos J, **van der Geest RJ**. Blood pool contrast agent CMD-A2-Gd-DOTA-Enhanced MR imaging of infarcted myocardium in pigs. J Magn Reson Imaging 1999; 10:170-177.
29. Kroft LJM, Doornbos J, **van der Geest RJ**, Benderbous S, de Roos A. Infarcted myocardium in pigs: MR imaging enhanced with slow-interstitial-diffusion gadolinium compound P760. Radiology 1999; 212:467-473.
30. Marcus JT, de Waal LK, Götte MJW, **van der Geest RJ**, Heethaar RM, van Rossum AC. MRI-derived left ventricular function parameters and mass in healthy young adults: Relation with gender and age. Int J Cardiac Imag 1999; 15:411-419.
31. Westenberg JJM, Wasser MNJM, **van der Geest RJ**, Pattynama PMT, de Roos A, Vanderschoot J, Reiber JHC. Gadolinium contrast-enhanced three-dimensional MRA of peripheral arteries with multiple bolus injection: scan optimization in vitro and in vivo. Int J Cardiac Imag 1999; 15:161-173.
32. Marcus JT, Smeenk HG, Kuijer JP, **van der Geest RJ**, Heethaar RM, van Rossum AC. Flow profiles in the left anterior descending and the right coronary artery assessed by MR velocity quantification: effects of through-plane and in-plane motion of the heart. J Comput Assist Tomogr 1999; 23:567-576.
33. **van der Geest RJ**, Lelieveldt BPF, Reiber JHC Quantification of global and regional ventricular function in cardiac magnetic resonance imaging. Topics in Magn Reson Imag 2000; 11:348-358.
34. Kayser HW, **van der Geest RJ**, van der Wall EE, Duchateau C, de Roos A. Right ventricular function in patients after acute myocardial infarction assessed with phase contrast MR velocity mapping encoded in three directions. J Magn Reson Imag 2000; 11:471-475.
35. Egmont-Petersen M, Hogendoorn PCW, **van der Geest RJ**, Vrooman HA, van der Woude HJ, Janssen JP, Bloem JL, Reiber JHC. Detection of areas with viable remnant tumor in postchemotherapy patients with Ewing's sarcoma by dynamic contrast-enhanced MRI using pharmacokinetic modeling. Magn Reson Imaging 2000; 18:525-535.
36. Westenberg JJM, **van der Geest RJ**, Wasser MNJM, van der Linden EL, van Walsum T, van Assen HC, de Roos A, Vanderschoot J, Reiber JHC. Vessel diameter measurements in gadolinium contrast-enhanced three-dimensional MRA of peripheral arteries. Magn Reson Imag 2000; 18:13-22.
37. Ramze Rezaee M, van der Zwet PMJ, B.P.F.Lelieveldt, **van der Geest RJ**, Reiber JHC. A multi-resolution segmentation technique based on pyramidal segmentation and fuzzy clustering. IEEE Transactions on Image Processing 2000; 9:1238-1248.

Chapter

11

38. Mitchell SC, Lelieveldt BPF, **van der Geest RJ**, Bosch JG, Reiber JHC, Sonka M. Multistage hybrid active appearance model matching: Segmentation of left and right ventricles in cardiac MR images. IEEE Trans Med Imag 2001; 20:415-423.

39. Wagenaar HC, Trimbos JBMZ, Postema S, Anastasopoulou A, **van der Geest RJ**, Reiber JHC, Kenter GG, Peters AAW, Pattynama PMT. Tumor diameter and volume assessed by magnetic resonance imaging in the prediction of outcome for invasive cervical cancer. Gynecologic Oncology 2001; 82:474-482.

40. Lelieveldt BPF, **van der Geest RJ**, Lamb HJ, Kayser HWM, Reiber JHC. Automated observer-independent acquisition of cardiac short-axis MR images: A pilot study. Radiology 2001; 221:537-542.

41. Box FMA, Rutten, MCM, van Buchem MA, Doornbos J, van der Geest, RJ, de Koning PJH, Schaap JA, van de Vosse FN, Reiber JHC. Quantitative methods for comparisons between velocity Encoded MR-measurements and finite element modeling in phantom models. International Conference on Computational Science. Sloot PMA, Tan CJK, Dongarra JJ, and Hoekstra AG. 3:255-264, 2002.

42. Spilt A, Box FMA, **van der Geest RJ**, Reiber JHC, Kunz P, Kamper AM, Blauw GJ, van Buchem MA. Reproducibility of total cerebral blood flow measurements using phase contrast magnetic resonance imaging. J Magn Reson Imaging 2002; 16:1-5.

43. Dirksen MS, Bax JJ, de Roos A, Jukema JW, **van der Geest RJ**, Geleijns K, Boersma E, van der Wall EE, Lamb HJ. Usefulness of dynamic Multislice Computed Tomography of left ventricular function in unstable angina pectoris and comparison with Echocardiography. Am J Cardiol 2002; 90:1157-1160.

44. Janssen JP, Egmont-Petersen M, Hendriks EA, Reinders MJT, **van der Geest RJ**, Hogendoorn PCW, Reiber JHC. Scale-invariant segmentation of dynamic contrast-enhanced perfusion MR images with inherent scale selection. J Visualization and Computer Animation; 2002; 13:1-19.

45. Mitchell SC, Bosch JG, Lelieveldt BPF, **van der Geest RJ**, Reiber JHC, Sonka M. 3-D Active appearance models: Segmentation of cardiac MR and ultrasound images. IEEE Med Imag 2002; 21:1167-1178.

46. Dirksen MS, Lamb HJ, **van der Geest RJ**, de Roos A. Toward comparability of coronary magnetic resonance angiography: proposal for a standardized quantitative assessment. Eur Radiology 2003; 13:2353-2357.

47. Box FMA, Spilt A, Van Buchem MA, **van der Geest RJ**, Reiber JHC. Automatic model-based contour detection and blood flow quantification in small vessels with velocity encoded magnetic resonance imaging Invest Radiol. 2003; 38:567-577.

48. de Koning PJH, Schaap JA, Janssen JP, Westenberg JJM, **van der Geest RJ**, Reiber JHC. Automated segmentation and analysis of vascular structures in magnetic resonance angiographic images. Magn Reson Med 2003; 50:1189-1198.

49. **van der Geest RJ**, Lelieveldt BPF, Angelié E, Danilouchkine M, Swingen C, Sonka M, Reiber JHC. Evaluation of a new method for automated detection of left ventricular boundaries in time series of magnetic resonance images using an Active Appearance Motion Model. J Cardiovasc Magn Reson 2004; 6:609-617.

50. Adame, IM, **van der Geest RJ**, Mohamed M, Wasserman BA, Reiber JHC, Lelieveldt BPF. Automatic Plaque Characterization and Vessel Wall Segmentation in Magnetic Resonance Images of Atherosclerotic Carotid Arteries, SPIE. Medical Imaging 2004; 5370:265-273.

51. Adame IM, **van der Geest RJ**, Wasserman BA, Mohamed M, Reiber JHC, Lelieveldt BPF. Automatic segmentation and plaque characterization in atherosclerotic carotid artery MR images. MAGMA (Magnetic Resonance Materials in Physics, Biology and Medicine) 2004; 16:227-234.

52. Schuijf JD, Kaandorp TA, Lamb HJ, **van der Geest RJ**, Viergever EP, van der Wall EE, de Roos A, Bax JJ. Quantification of myocardial infarct size and transmurality by contrast-enhanced magnetic resonance imaging in men. Am J Cardiol. 2004; 94:284-288.

53. Westenberg JJM, Danilouchkine MG, Doornbos J, Bax JJ, **van der Geest RJ**, Labadie G, Lamb HJ, Versteegh MIM, de Roos A, Reiber JHC. Accurate and reproducible mitral valvular blood flow measurement with three-directional velocity-encoded magnetic resonance imaging. J Cardiovasc Magn Reson 2004; 6 :767-776.

54. Dirksen MS, Bax JJ, de Roos A, Jukema JW, **van der Geest RJ**, Geleijns J, van der Wall EE, Lamb HJ . Dynamic multislice computed tomography of left ventricular function. Circulation 2004; 109:E25-E26.

55. Angelié E, De Koning PJH, Danilouchkine MG, Van Assen HA, Koning G, **van der Geest RJ**, Reiber JHC. Optimizing the automatic segmentation of the left ventricle in magnetic resonance images. Med Physics 2005; 32:369-375

56. Westenberg JJM, Doornbos J, Versteegh MIM, Bax JJ, **van der Geest RJ**, de Roos A, Dion RAE, Reiber JHC. Accurate quantitation of regurgitant volume with MRI in patients selected for mitral valve repair European Journal of Cardio-thoracic Surgery 2005; 27:462–467.

57. Üzümcü, M, **van der Geest RJ**, Sonka M, Lamb HJ, Reiber JHC, Lelieveldt BPF. Multiview active appearance models for simultaneous segmentation of cardiac 2- and 4-chamber long-Axis magnetic resonance images. Invest Radiol 2005; 40:195-203

58. van Wijk JPH, Castro Cabezas M, de Koning EJP, Rabelink TJ, **van der Geest RJ**, Hoepelman IM. In vivo evidence of impaired peripheral fatty acid trapping in patients with human immunodeficiency virus-associated lipodystrophy J of Clin Endocrinology Metab. 2005; 90:3575-3582.

59. Paelinck BP, de Roos A, Bax JJ, Bosmans JM, **van der Geest RJ**, Dhondt D, Parizel PM, Vrints CJ, Lamb HJ. Feasibility of tissue magnetic resonance imaging: a pilot study in comparison with tissue Doppler imaging and invasive measurement. J Am Coll Cardiol. 2005; 45:1109-1116

60. Box FM, **van der Geest RJ**, Rutten MC, Reiber JHC. The Influence of flow, vessel diameter, and non-Newtonian blood viscosity on the wall shear stress in a carotid bifurcation model for unsteady flow. Invest Radiol. 2005; 40:277-294.

61. de Vries M, de Koning PJ, de Haan MW, Kessels AG, Nelemans PJ, Nijenhuis RJ, Planken RN, Vasbinder GBC, van Engelshoven JMA, **van der Geest RJ**, Leiner T. Accuracy of Semiautomated Analysis of 3D Contrast-Enhanced Magnetic Resonance Angiography for detection and quantification of aortoiliac stenoses. Invest Radiol 2005; 40:495-503.

62. van den Dool SW, Wasser MN, de Fijter JW, Hoekstra J, **van der Geest RJ**. Functional renal volume: Quantitative analysis at gadolinium-enhanced MR angiography – Feasibility study in healthy potential kidney donors. Radiology 2005; 236:189-195.

63. Westenberg JJM, **van der Geest RJ**, Lamb HJ, Versteegh MIM, Braun J, Doornbos J, de Roos A, van der Wall EE, Dion RAE, Reiber JHC, Bax JJ. MRI to evaluate left atrial and ventricular reverse remodeling after restrictive mitral annuloplasty in dilated cardiomyopathy. Circulation 2005; 112 [suppl I]:437-442.

64. Danilouchkine MG, **van der Geest RJ**, Westenberg JJ, Lelieveldt BPF, Reiber JHC. Influence of positional and angular variation of automatically planned short-axis stacks on quantification of left ventricular dimensions and function with cardiovascular magnetic resonance. J Magn Reson Imaging 2005; 22:754-764.

Chapter

11

65. Sonka M, Thedens DR, Lelieveldt BPF, Mitchell SC, **van der Geest RJ**, Reiber JHC, Cardiovascular MR image analysis. In: Computer vision beyond the visible spectrum. Bir B, Pavlidis I (Eds), pp 193-240, Springer Verlag, Berlin, ISBN: 1-85233-604-8, 2005.
66. Üzümcü M, **van der Geest RJ**, Swingen C, Reiber JH, Lelieveldt BP. Time continuous tracking and segmentation of cardiovascular magnetic resonance images using multidimensional dynamic programming. Invest Radiol. 2006; 41:52-62.
67. Westenberg JJ, Lamb HJ, **van der Geest RJ**, Bleeker GB, Holman ER, Schalij MJ, de Roos A, van der Wall EE, Reiber JH, Bax JJ. Assessment of left ventricular dyssynchrony in patients with conduction delay and idiopathic dilated cardiomyopathy: head-to-head comparison between tissue doppler imaging and velocity-encoded magnetic resonance imaging. J Am Coll Cardiol. 2006; 47:2042-2048.
68. Doğan H, Kroft LJ, Bax JJ, Schuijf JD, **van der Geest RJ**, Doornbos J, de Roos A. MDCT assessment of right ventricular systolic function. Am J Roentgenol. 2006; 186:S366-S370.
69. Adame IM, de Koning PJH, Lelieveldt BPF, Wasserman BA, Reiber JHC, **van der Geest RJ**. An integrated automated analysis method for quantifying vessel stenosis and plaque burden from carotid MRI images: Combined postprocessing of MRA and vessel wall MR. Stroke 2006; 37:2162-2164.
70. Adame IM, **van der Geest RJ**, Bluemke DA, Lima JA, Reiber JHC, Lelieveldt RBF. Automatic vessel wall contour detection and quantification of wall thickness in in-vivo MR images of the human aorta. J Magn Reson Imaging. 2006; 24:595-602
71. Schoonman GG, Bakker D, Schmitz N, **van der Geest RJ**, van der Grond J, Ferrari MD, van Buchem MA. Magnetic resonance angiography of the human middle meningeal artery: implications for migraine. J Magn Reson Imaging. 2006; 24:918-921.
72. Doğan H, MD, Kroft LJM, Huisman MV, **van der Geest RJ**, de Roos A. Right Ventricular Function in Patients with Acute Pulmonary Embolism: Analysis with Electrocardiography-synchronized Multi–Detector Row CT. Radiology 2007; 242:78-84.
73. Box FMA, van der Grond J, de Craen AJ, Palm-Meinders IH, **van der Geest RJ**, Reiber JHC, van Buchem MA, Blauw GJ. Pravastatin decreases wall shear stress and blood velocity in the internal carotid artery without affecting flow volume: results from the PROSPER MRI Study. Stroke 2007; 38:1374-3376.
74. Dehnavi RA, Doornbos J, Tamsma JT, Stuber M, Putter H, **van der Geest RJ**, Lamb HJ, de Roos A. Assessment of the carotid artery by MRI at 3T: A study on reproducibility. J. Magn. Reson. Imaging 2007; 25:1035-1043
75. Milles J, **van der Geest RJ**, Jerosch-Herold M, Reiber JHC, Lelieveldt BPF. Fully automated registration of first-pass myocardial perfusion MRI using independent component analysis. Inf Process Med Imaging 2007; 20:544-555.
76. Box FM, **van der Geest RJ**, van der Grond J, van Osch MJ, Zwinderman AH, Palm-Meinders IH, Doornbos J, Blauw GJ, van Buchem MA, Reiber JHC. Reproducibility of wall shear stress assessment with the paraboloid method in the internal carotid artery with velocity encoded MRI in healthy young individuals. J Magn Reson Imaging. 2007; 26:598-605.
77. Winter EM, Grauss RW, Hogers B, van Tuyn J, **van der Geest RJ**, Lie-Venema H, Vicente Steijn R, Maas S, de Ruiter MC, de Vries AAF, Steendijk P, Doevendans PA, van der Laarse A, Poelmann RE, Schalij MJ, Atsma DE, Gittenberger-de Groot AC. Preservation of left ventricular function and attenuation of remodeling after transplantation of human epicardium-derived cells into the Infarcted mouse heart. Circulation 2007; 116:917-927.

78. Grauss RW, Winter EM, van Tuyn J, Pijnappels DA, Steijn RV, Hogers B, **van der Geest RJ**, de Vries AA, Steendijk P, van der Laarse A, Gittenberger-de Groot AC, Schalij MJ, Atsma DE. Mesenchymal stem cells from ischemic heart disease patients improve left ventricular function after acute myocardial infarction. Am J Physiol Heart Circ Physiol 2007; 293:H2438-H2447.

79. Angelié E, Oost ER, Hendriksen D, Lelieveldt BP, **Van der Geest RJ**, Reiber JH. Automated contour detection in cardiac MRI using active appearance models: the effect of the composition of the training set. Invest Radiol. 2007; 42:697-703.

80. Henneman MM, Schuijf JD, Dibbets-Schneider P, Stokkel MP, **van der Geest RJ**, van der Wall EE, Bax JJ. Comparison of multislice computed tomography to gated single-photon emission computed tomography for imaging of healed myocardial infarcts. Am J Cardiol. 2008; 101:144-148.

81. Winter EM, Grauss RW, Atsma DE, Hogers B, Poelmann RE, **van der Geest RJ**, Tschöpe C, Schalij MJ, Gittenberger-de Groot AC, Steendijk P. Left ventricular function in the post-infarct failing mouse heart by magnetic resonance imaging and conductance catheter: a comparative analysis. Acta Physiol (Oxf). 2008; 194:111-122.

82. Grauss RW, van Tuyn J, Steendijk P, Winter EM, Pijnappels DA, Hogers B, Gittenberger-De Groot AC, **van der Geest RJ**, van der Laarse A, de Vries AA, Schalij MJ, Atsma DE. Forced myocardin expression enhances the therapeutic effect of human mesenchymal stem cells after transplantation in ischemic mouse hearts. Stem Cells. 2008; 26:1083-1093.

83. Schoonman GG, van der Grond J, Kortmann C, **van der Geest RJ**, Terwindt GM, Ferrari MD. Migraine headache is not associated with cerebral or meningeal vasodilatation-a 3T magnetic resonance angiography study. Brain. 2008; 131:2192-2200.

84. Westenberg JJ, Braun J, Van de Veire NR, Klautz RJ, Versteegh MI, Roes SD, **van der Geest RJ**, de Roos A, van der Wall EE, Reiber JH, Bax JJ, Dion RA. Magnetic resonance imaging assessment of reverse left ventricular remodeling late after restrictive mitral annuloplasty in early stages of dilated cardiomyopathy. J Thorac Cardiovasc Surg. 2008; 135:1247-1252.

85. Westenberg JJ, Roes SD, Ajmone Marsan N, Binnendijk NM, Doornbos J, Bax JJ, Reiber JH, de Roos A, **van der Geest RJ**. Mitral Valve and Tricuspid Valve Blood Flow: Accurate Quantification with 3D Velocity-encoded MR Imaging with Retrospective Valve Tracking. Radiology. 2008; 249:792-800.

86. Milles J, **van der Geest RJ**, Jerosch-Herold M, Reiber JH, Lelieveldt BPF. Fully automated motion correction in first-pass myocardial perfusion MR image sequences. IEEE Trans Med Imaging. 2008; 27:1611-1621.

87. Roes SD, Westenberg JJ, Doornbos J, **van der Geest RJ**, Angelié E, de Roos A, Stuber M. Aortic vessel wall magnetic resonance imaging at 3.0 tesla: A reproducibility study of respiratory navigator gated free-breathing 3D black blood magnetic resonance imaging. Magn Reson Med 2009; 61:35-44.

88. Roes SD, Borleffs CJW, **van der Geest RJ**, Westenberg JJM, Ajmone Marsan N,. Kaandorp TAM, Reiber JHC, Zeppenfeld K, Lamb HJ, de Roos A, Schalij MJ, Bax JJ. Infarct Tissue Heterogeneity Assessed with Contrast-Enhanced Magnetic Resonance Imaging Predicts Spontaneous Ventricular Arrhythmia in Patients with Ischemic Cardiomyopathy and Implantable Cardioverter-Defibrillator. Circ Cardiovasc Imaging 2009;2(3):183-190.

89. El Aidi H, Mani V, Weinshelbaum KB, Aguiar SH, Taniguchi H, Postley JE, Samber DD, Cohen EI, Stern J, **van der Geest RJ**, Reiber JH, Woodward M, Fuster V, Gidding SS, Fayad ZA. Cross-sectional, prospective study of MRI reproducibility in the assessment of plaque burden of the carotid arteries and aorta. Nat Clin Pract Cardiovasc Med 2009;6(3)219-228.

Chapter

11

90. Mani V, Muntner P, Gidding SS, Aguiar SH, El Aidi H, Weinshelbaum KB, Taniguchi H, **van der Geest RJ**, Reiber JH, Bansilal S, Farkouh M, Fuster V, Postley JE, Woodward M, Fayad ZA. Cardiovascular magnetic resonance parameters of atherosclerotic plaque burden improve discrimination of prior major adverse cardiovascular events. J Cardiovasc Magn Reson. 2009;11(1):10.

91. Kornaat PR, Sharma R, **van der Geest RJ**, Lamb HJ, Kloppenburg M, Hellio le Graverand MP, Bloem JL, Watt I. Positive association between increased popliteal artery vessel wall thickness and generalized osteoarthritis: is OA also part of the metabolic syndrome? Skeletal Radiol. 2009.

92. Marsan NA, Westenberg JJ, Ypenburg C, van Bommel RJ, Roes S, Delgado V, Tops LF, **van der Geest RJ**, Boersma E, de Roos A, Schalij MJ, Bax JJ. Magnetic resonance imaging and response to cardiac resynchronization therapy: relative merits of left ventricular dyssynchrony and scar tissue. Eur Heart J 2009.

93. Duivenvoorden R, de Groot E, Elsen BM, Lameris JS, **van der Geest RJ**, Stroes ES, Kastelein JJP, Nederveen AJ. In Vivo Quantification of Carotid Artery Wall Dimensions 3.0-Tesla MRI Versus B-Mode Ultrasound Imaging. Circ Cardiovasc Imaging 2009;2(3):235-242.

94. Grotenhuis HB, Westenberg JJ, Steendijk P, **van der Geest RJ**, Ottenkamp J, Bax JJ, Jukema JW, de Roos A. Validation and reproducibility of aortic pulse wave velocity as assessed with velocity-encoded MRI. J Magn Reson Imaging 2009;30(3):521-526.

95. Roes SD, Hammer S, **van der Geest RJ**, Ajmone Marsan N, Bax JJ, Lamb HJ, Reiber JHC, de Roos A, Westenberg JJM. Flow Assessment Through Four Heart Valves Simultaneously Using 3-Dimensional 3-Directional Velocity-Encoded Magnetic Resonance Imaging With Retrospective Valve Tracking in Healthy Volunteers and Patients With Valvular Regurgitation. Invest Radiol 2009;44:669-675.

96. Zudilova-Seinstra EV, de Koning PJH, Suinesiaputra A, van Schooten BW, **van der Geest RJ**, Reiber JHC, Sloot PMA. Evaluation of 2D and 3D glove input applied to medical image analysis. International Journal of Human Computer Studies 2009,doi:10.1016/j.ijhcs.2009.08.001.

97. Zudilova-Seinstra E, van Schooten B, Suinesiaputra A, **van der Geest RJ**, van Dijk B, Reiber JHC, Sloot PMA. Exploring individual user differences in the 2D/3D interaction with medical image data. Virtual Reality 2009, DOI 10.1007/s10055-009-0131-4.

98. Kwee RM, Teule GJJ, van Oostenbrugge RJ, Mess WH, Prins MH, **van der Geest RJ**, ter Berg JWM, Franke CL, Korten AGGC, Meems BJ, Hofman PAM, van Engelshoven JMA, Wildberger JE, Kooi EM. Multimodality Imaging of Carotid Artery Plaques 18F-Fluoro-2-Deoxyglucose Positron Emission Tomography, Computed Tomography, and Magnetic Resonance Imaging. Stroke. 2009;40(12):3718-3724.

99. Marsan NA, Westenberg JJ, Ypenburg C, Delgado V, van Bommel RJ, Roes SD, Nucifora G, **van der Geest RJ**, de Roos A, Reiber JC, Schalij MJ, Bax JJ. Quantification of functional mitral regurgitation by real-time 3D echocardiography: comparison with 3D velocity-encoded cardiac magnetic resonance. JACC Cardiovasc Imaging. 2009;2(11):1245-52.

100. Attili AK, Schuster A, Nagel E, Reiber JHC, **van der Geest RJ**. Quantification in cardiac MRI: advances in image acquisition and processing. Int J Cardiovasc Imaging 2010;26 Suppl 1:27-40.

101. Germans T, Russel IK, Gotte MJW, Spreeuwenberg MD, Doevendans PA, Pinto YM, **van der Geest RJ**, van der Velden J, de Wilde AAM, van Rossum AC. How do hypertrophic cardiomyopathy mutations affect myocardial function in carriers with normal wall thickness? Assessment with cardiovascular magnetic resonance. J Cardiovasc Magn Reson 2010;12:13, doi:10.1186/1532-429X-12-13.

102. Lobbes MB, Heeneman S, Passos VL, Welten R, Kwee RM, **van der Geest RJ**, Wiethoff AJ, Caravan P, Misselwitz B, Daemen MJ, van Engelshoven JM, Leiner T, Kooi ME. Gadofosveset-enhanced magnetic resonance imaging of human carotid atherosclerotic plaques: A proof-of-concept study. Invest Radiol. 2010;45(5):275-281.

103. Zudilova-Seinstra EV, de Koning PJH, Suinesiaputra A, van Schooten BW, **van der Geest RJ**, Reiber JHC, Sloot PMA. Evaluation of 2D and 3D glove input applied to medical image analysis. International Journal of Human Computer Studies 2010;68 (6) 355-369.

104. Tao Q, Milles J, Zeppenfeld K, Lamb HJ, Bax JJ, Reiber JH, **van der Geest RJ**. Automated segmentation of myocardial scar in late enhancement MRI using combined intensity and spatial information. Magn Reson Med. 2010; 64(2):586-594.

105. Gupta V, Hendriks EA, Milles J, **van der Geest RJ**, Jerosch-Herold M, Reiber JH, Lelieveldt BPF. Fully Automatic Registration and Segmentation of First-Pass Myocardial Perfusion MR Image Sequences. Acad Radiol. 2010;17(11):1375-1385.

106. Kwee RM, van Oostenbrugge RJ, Mess WH, Prins MH, **van der Geest RJ**, Ter Berg JW, Franke CL, Korten AG, Meems BJ, van Engelshoven JM, Wildberger JE, Kooi ME. Carotid plaques in transient ischemic attack and stroke patients: One-year follow-up study by magnetic resonance imaging. Invest Radiol. 2010 Sep 8. [Epub ahead of print].

107. Wijnmalen AP, **van der Geest RJ**, van Huls van Taxis CF, Siebelink HM, Kroft LJ, Bax JJ, Reiber JHC, Schalij MJ, Zeppenfeld K. Head-to-head comparison of contrast-enhanced magnetic resonance imaging and electroanatomical voltage mapping to assess post-infarct scar characteristics in patients with ventricular tachycardias: Real-time image integration and reversed registration. Eur Heart J. 2010;32(1):104-114.

108. Gerretsen SC, Kooi ME, Kessels AG, Schalla S, Katoh M, **van der Geest RJ**, Manning WJ, Waltenberger J, van Engelshoven JMA, Botnar RM, Leiner T. Visualization of Coronary Wall Atherosclerosis in Asymptomatic Subjects and Patients with Coronary Artery Disease Using Magnetic Resonance Imaging. PloS One 2010;5(9):e12998.

109. M.S. Asghar MS, Hansen AE, Kapijimpanga T, **van der Geest RJ**, van der Koning P, Larsson HBW, Olesen J, Ashina M. Dilation by CGRP of middle meningeal artery and reversal by sumatriptan in normal volunteers. Neurology 2010;75:1520-1526.

110. Westenberg JJ, de Roos A, Grotenhuis HB, Steendijk P, Hendriksen D, van den Boogaard PJ, **van der Geest RJ**, Bax JJ, Jukema JW, Reiber JH. Improved aortic pulse wave velocity assessment from multislice two-directional in-plane velocity-encoded magnetic resonance imaging. J Magn Reson Imaging 2010;32(5):1086-1094.

111. Gai N, Turkbey EB, Nazarian S, **van der Geest RJ**, Liu CY, Lima JA, Bluemke DA. T(1) mapping of the gadolinium-enhanced myocardium: Adjustment for factors affecting interpatient comparison. Magn Reson Med. 2010 Dec 16. [Epub ahead of print]

112. Marsan NA, Westenberg JJ, Roes SD, van Bommel RJ, Delgado V, **van der Geest RJ**, de Roos A, Klautz RJ, Reiber JC, Bax JJ. Three-dimensional echocardiography for the preoperative assessment of patients with left ventricular aneurysm. Ann Thorac Surg. 2011;91(1):113-121.

Chapter

11

11.2 PAPERS IN CONFERENCE PROCEEDINGS

1.   Dumay ACM, Gerbrands JJ, **van der Geest RJ**, Verbruggen PE, Reiber JHC. Automated labeling of coronary tree segments in angiographic projection data. SPIE Medical Imaging V: Image Processing. SPIE, 1991; 1445:38-46:439-442.
2.   Dumay ACM, **van der Geest RJ**, Gerbrands JJ, Jansen E, Reiber JHC. Consistent inexact graph matching applied to labelling coronary segments in arteriograms. Proc 11th International Conference on Pattern Recognition 1992 (The Hague Aug 30 - Sept 3 1992):439-442.
3.   **van der Geest RJ**, Jansen E, Buller VGM, Reiber JHC. Automated detection of left ventricular epi- and endocardial contours in short-axis MR images. IEEE Comput Comput 1994:33-36
4.   **van der Geest RJ**, Buller VGM, Reiber JHC. Automated quantification of flow velocity and volume in the ascending and descending aorta using MR flow velocity mapping. IEEE, Comput Cardiol 1995:29-32.
5.   Buller VGM, **van der Geest RJ**, Kool MD, Reiber JHC. Accurate three-dimensional wall thickness measurement from multi-slice short-axis MR imaging. IEEE Comput Cardiol 1995:245-248.
6.   Lelieveldt BPF, **van der Geest RJ**, Reiber JHC. Automated model driven localization of the heart and lung surfaces in thoracic MR images. IEEE, Comput Cardiol 1998; 25:9-12.
7.   Lelieveldt BPF, Rijsdam JT, **van der Geest RJ**, Huijsmans DP, Reiber JHC. Model driven interpretation of velocity encoded aortic flow images by means of Voronoi arrangement matrices. IEEE, Comput Cardiol 1998; 25:753-756.
8.   Lelieveldt BPF, Sonka M, Bolinger L, Scholtz TD, Kayser HWM, **van der Geest RJ**, Reiber JHC. Anatomical modeling with fuzzy implicit surfaces: application to automated localization of the heart and lung surfaces in thoracic MR Images. In: Samal AKaM, ed. Proc. Information Processing in Medical Imaging, Lecture Notes in Computer Science. Berlin: Springer Verlag, 1999: 400-405.
9.   Mitchell SC, Lelieveldt BPF, **van der Geest RJ**, Bosch JG, Reiber JHC, Sonka M. Segmentation of cardiac MR images: An active appearance model approach. proc. SPIE Medical Imaging 2000 Image Processing 2000; 3979:224-234.
10.   Egmont-Petersen M, Hogendoorn PCW, **van der Geest RJ**, Bloem JL, and Reiber JHC. Assessment of the influence of preoperative chemotherapy in patients with osteosarcoma by dynamic contrast-enhanced MRI using pharmocokinetic modeling. Bildverarbeitung für der medizin. Handels H, Horst A, Lehmann T, and Meinzer HP. Springer Verslag, Berlin. 399-403, 2001.
11.   Schaap JA, de Koning PJH, Janssen JP, Westenberg JJM, **van der Geest RJ**, Reiber JHC. 3D quantification visualization of vascular structures in magnetic resonance angiographic images. International Conference on Computational Science. Sloot PMA, Tan CJK, Dongarra JJ, and Hoekstra AG. 3:242-254, 2002.
12.   Guzman R, Remonda L, de Koning PJH, **van der Geest RJ**, Oswald O, Schroth G. Correlation of quantitative MR angiography of the carotid artery with in-vivo measurement during carotid endarterectemy. In: Computer Assisted Radiology and Surgery - CARS 2002. HU Lemke, MW Vannier, K Inamura, AG Farman, K Doi, JHC Reiber (Eds.). Elsevier Science BV 2002: 917-922.
13.   Lelieveldt BPF, Uzümcü M, **van der Geest RJ**, Reiber JHC, Sonka M. Multi-view active appearance models for consistent segmentation of multiple standard views: application to long- and short-axis cardiac MR images. In: Computer Assisted Radiology and Surgery - CARS 2003. HU Lemke, MW Vannier, K Inamura, AG Farman, K Doi, JHC Reiber (Eds.). Elsevier Science BV 2003:1141-1146.

14. Angelié E, de Koning PJH, van Assen HC, Danilouchkine M, Koning G, **van der Geest RJ**, Reiber JHC. Automatic tuning of left ventricular segmentation of MR images using genetic algorithms. In: Computer Assisted Radiology and Surgery - CARS 2003. HU Lemke, MW Vannier, K Inamura, AG Farman, K Doi, JHC Reiber (Eds.). Elsevier Science BV 2003:1102-1107.

15. van Assen HC, **van der Geest RJ**, Danilouchkine MG, Lamb HJ, Reiber JHC, Lelieveldt BPF. 3D Active Shape Model matching for left ventricle segmentation in cardiac CT. In: Medical Imaging 2003: Image Processing. M. Sonka, JM Fitzpatrick, Eds. SPIE, Vol. 5032; 2003: 384-93. SPIE, Vol. 5032; 2003:949-957.

16. Van Assen HC, Danilouchkine MG, Behloul F, Lamb HJ, **van der Geest RJ**, Reiber JHC, Lelieveldt BPF. Cardiac LV segmentation using a 3D active shape model driven by fuzzy inference. Proc MICCAI 2003, Lecture Notes in Computer Sceince 2003; 2878:533-540.

17. Abrahamyan L, Schaap JA, Hoekstra AG, Shamonin D, Box FMA, **van der Geest RJ**, Reiber JHC, Sloot PMA. A problem solving environment for image-based computational hemodynamics. VS Sunderam, GD van Albada, PMA Sloot, JJ Dongarra (Eds.). Computational Science - ICCS 2005: 5th International Conference, Atlanta, GA, USA. Lecture Notes in Computer Science, 3514:287-294. Springer-Verslag Berlin Heidelberg.

18. Milles J, **van der Geest RJ**, Jerosch-Herold M, Reiber JHC, Lelieveldt BPF. Analysis of first-pass myocardial perfusion MRI using independent component analysis. In: SPIE Medical Imaging 2006: Image Processing, JM Reinardt , JPW Pluim Eds. SPIE 2006;Vol 6144:pp-pp 596-604

19. Makowski P, de Koning PJH, Angelié E., Westenberg JJM, **van der Geest RJ**, Reiber JHC. 3D Cylindrical B-Spline Segmentation of Carotid Arteries from MRI Images. In: Lecture Notes in Computer Science, Biomedical Simulation. Springer Berlin/Heidelberg 2006;188-196.

11.3 BOOK CHAPTERS AND OTHER PUBLICATIONS

1. Reiber JHC, van der Zwet PMJ, Koning G, von Land CD, Bosch JG, Maurincomme E, **van der Geest RJ**, Gerbrands JJ. Perspectieven in beeldvorming en beeldverwerking. In: Verheugt F (Ed). 'De toekomst van de cardiologie'. Nederlands Hartstichting. 1994: 63-91.

2. Reiber JHC, Goedhart B, Bosch JG, **van der Geest RJ**, Dijkstra J, Koning G, Rezaee MR, Lelieveldt BPF, de Roos A, van der Wall EE, Bruschke AVG. Quantitative cardiovascular image analysis: Current status and what are realistic expectations for the future? In: E.E. van der Wall, V. Manger Cats, J. Baan (Eds) 'Vascular Medicine'. Kluwer Academic Publishers, Dordrecht, 1997:103-131.

3. **van der Geest RJ**, Reiber JHC. Quantification in Cardiac MRI. In: CB Higgins, A de Roos (Eds). 'Cardiovascular MRI and MRA'. Lippincott Williams & Wilkins, Philadelphia, 2003: 70-81.

4. Schaap JA, de Koning PJ, Janssen JP, **van der Geest RJ**, Reiber JH. Quantitative analysis of vascular images, in particular of abdominal aorta aneurysms from 3D CTA data sets. Stud Health Technol Inform. 2004; 103:252-258

5. Lelieveldt BPF, **van der Geest RJ**, Reiber JHC. Towards 'One-Stop' cardiac MR image analysis. Imaging Decision MRI 2004;8:2-12.

6. **van der Geest RJ**, Lelieveldt BPF, Reiber JHC. Quantification in cardiac magnetic resonance imaging and computed tomography. In: C.B. Higgins, A. de Roos (Eds) 'MRI and CT of the cardiovascular system' (second edition). Philadelphia, PN, 2006:91-106.

Chapter

11

7. **van der Geest RJ**, Kitslaar PH, de Koning PJH, van 't Klooster R, Jukema WJ, Koning G, Marquering HA, Reiber JHC. Advanced three-dimensional postprocessing in computed tomographic and magnetic resonance angiography. In: Ho VB and Reddy GP (Eds) 'Cardiovascular imaging.' St Louis, MO, 2011:1128-1143.

Acknowledgments

Curriculum vitae

Rob van der Geest was born in Leiderdorp, the Netherlands on March 9, 1966. In 1984 he received his VWO diploma from the Bonaventura Scholengemeenschap, Leiden, and in 1992 his Master of Science degree (ir.) in Electrical Engineering at the Delft University of Technology, Delft, The Netherlands. The topic of his graduation work was the development of a system for automated labeling of branches of the coronary arterial tree in X-ray angiograms. He spent three months at Duke University Medical Center, Durham, USA to carry out validation experiments for an automated system for assessment of coronary artery dimensions from X-ray angiograms. In 1992 he joined the Laboratory for Clinical and Experimental Image Processing (LKEB) of the Leiden University Medical Center. At this position he started new developments into cardiovascular Magnetic Resonance Imaging. The main topic of research was the development of automated contour detection methods needed for assessment of quantitative functional parameters from cine MR acquisitions and MR velocity-encoded imaging. The results of this work have been described in this thesis. Currently, he is heading the Section Cardiovascular Magnetic Resonance Imaging at LKEB. Under his supervision, image processing research is carried out for cardiac and vascular applications of Magnetic Resonance Imaging.